

Assen Zlatarov University
Burgas, Bulgaria



ANNUAL

VOLUME XLVIII, BOOK 1, 2019

TECHNICAL AND NATURAL SCIENCES



ASSEN ZLATAROV UNIVERSITY
BURGAS, BULGARIA

ANNUAL

Vol. XLVIII, BOOK 1, 2019

TECHNICAL AND NATURAL SCIENCES



Assen Zlatarov University

Assen Zlatarov University
Annual, Vol. XLVIII, Book 1, 2019
Burgas 8010, Bulgaria
ISSN 2603-3968

**ASSEN ZLATAROV UNIVERSITY
BURGAS, BULGARIA**

ANNUAL

Vol. XLVIII, BOOK 1, 2019

TECHNICAL AND NATURAL SCIENCES



BURGAS • 2019

Editor-in-Chief

Prof. Margarita Terzieva, DSc

Co-editors

Assoc. Prof. Penka Peeva, PhD
Assoc. Prof. Liliya Staneva, PhD
Asst. Prof. Ivan Sokolov

Editorial Boards

Section I: Technical Sciences

Assoc. Prof. Magdalena Mitkova, PhD
Prof. Valentin Nenov, PhD
Prof. Sotir Sotirov, PhD
Prof. Irena Markovska, PhD
Assoc. Prof. Yovka Nikolova, PhD
Assoc. Prof. Dimitrina Kiryakova, PhD
Assoc. Prof. Husein Yemendzhiev, PhD
Prof. A. Baran Dural (Turkey)
Prof. Yordan Nikov (France)

Section II: Natural Sciences

Assoc. Prof. Svetlana Zheleva, PhD
Prof. Nina Sultanova, PhD
Assoc. Prof. Zhechka Mihailova, PhD

Technical Assistant: Iliana Ishmerieva

Reviewers

Prof. Ts. Godzhevargova, DSc
Prof. G. Panayotova, PhD
Prof. E. Sotirova, PhD
Prof. An. Aleksandrov, PhD
Assoc. Prof. K. Gabrovska, PhD
Assoc. Prof. M. Dyulgerova, PhD
Assoc. Prof. I. Vardeva, PhD
Assoc. Prof. S. Koruderlieva, PhD
Assoc. Prof. Y. Tasheva, PhD
Assoc. Prof. L. Staneva, PhD
Assoc. Prof. Al. Dimitrov, PhD
Assoc. Prof. Ts. Dimitrov, PhD
Assoc. Prof. M. Stancheva, PhD
Assoc. Prof. Y. Koleva, PhD
Assoc. Prof. D. Dobrudzhaliev, PhD
Assoc. Prof. M. Lyubcheva, PhD
Assoc. Prof. Sv. Zheleva, PhD
Chief asst. Prof. G. Peeva, PhD
Chief Asst. Prof. R. Kasarov, PhD
Chief Asst. Prof. V. Ivanov, PhD

Section III: Social Sciences and Humanities

Prof. Bratoy Koprinarov, PhD
Assoc. Prof. Todor Palichev, PhD
Prof. Valentina Terentieva (Russia)
Prof. Kiril Chekalov (Russia)
Prof. Marina Yanich (Serbia)
Prof. Zaur Zavrumov (Russia)
Assoc. Prof. Galina Petrova, PhD

Section IV: Public Health and Health Care

Prof. Hristo Bozov, PhD
Assoc. Prof. Antoaneta Grozeva, PhD

VOLUME XLVIII (1). CONTENTS

<i>Nina Sultanova, Stefka Kasarova, Ivan Nikolov, Radostin Kasarov</i>	Application of polymers in the design of imaging systems	7
<i>Ivan Georgiev, Dimitar Yanakiev</i>	Numerical study of a subrecursive sequence converging to the Euler-Mascheroni constant	12
<i>Nikola Todorov, Veselina Yordanova, Vesela Manolova, Emine Ahmed, Mirela Toneva, Stanislav Evtimov, Aneliya Stoyanova, Vladilena Deyanova</i>	Monitoring of the noise pollution in ecology laboratory 327 in the Inorganic Chemistry Building of Prof. Dr Assen Zlatarov University, Burgas	16
<i>Irena Markovska, Fila Yovkova, Dimitar Georgiev, Magdalena Mitkova</i>	Synthesis and characterization of graphene	22
<i>Fila Yovkova, Irena Markovska, Dimitar Georgiev, Dimitar Rusev, Magdalena Mitkova</i>	Synthesis of highly porous dielectric ceramic materials with rice husk as pore-former	27
<i>Tsvetalina Ibrevva, Tsvetan Dimitrov, Aleksander Karamanov, Georgi Avdeev</i>	Synthesis and study of Co-doped willemite ceramic pigments	32
<i>Maya Stancheva, Hiusein Yemendzhiev, Valentin Nenov</i>	Monitoring the dynamics of soluble phosphates during anaerobic digestion of buffalo manure	36
<i>Yana Koleva</i>	Investigation of the bioactivity score of third generation retinoids	40
<i>Yana Koleva, Asen Kolev</i>	Molecular properties and bioactivity score of cyclododec-2-en-1-yl ethers	45
<i>Blagovesta Midyurova</i>	Design of air cathodes for application in microbial fuel cell	49
<i>Yordanka Tasheva</i>	Some features of gasoil extraction	53

<i>Galina Grigorova</i>	Testing raw cow milk used for dairy products	58
<i>Galina Yordanova, Milka Atanasova, Ruska Nenkova</i>	Bread yeast - vitality and viability, endurance and storage stability	61
<i>Desislava Nikolova</i>	An optimal oriented approach to the sustainable supply chain design for biorefinery	65
<i>Milena Miteva, Dimitrina Kiryakova, Stoyko Petrov</i>	Preparation and structure of PAN/clay nanocomposite membranes	69
<i>Plamena Atanasova, Sabina Nedkova</i>	Application of a model for assessment and analysis of radioactive activity	73
<i>Sabina Nedkova, Plamena Atanasova</i>	Crisis management and its relation with the anxiety state of people working in the chemical industry	77
<i>Veselina Bureva, Krassimir Atanassov, Nikolay Andreev</i>	Intercriteria analysis applied to healthcare rankings	81
<i>Stanislav Popov</i>	Generalized net model of stochastic expectation-maximization algorithm	86
<i>Ivaylo Belovski</i>	Thermoelectric energy convertors: features and operating modes	90
<i>Vasil Ivanov, Ivailo Belovski</i>	Survey of the impact of seasons over the effectiveness of solar panels	96
<i>Mladen Proykov</i>	Modernization of the street lighting system of a residential district	99
<i>Mladen Proykov</i>	Laboratory model for compensation of reactive power	104
<i>Vasil Bobev</i>	Combined road and railway transport in present-day Bulgaria	110
<i>Yuliyana Petrov</i>	Modeling of transient processes in a linear electric circuit of the second order with a generalized net	113
<i>Lachezar Radev</i>	Novel Mg-containing glass-ceramics in the SiO ₂ -CaO system and their in vitro bioactivity: XRD, FTIR, SEM and ICP-AES analysis	117

APPLICATION OF POLYMERS IN THE DESIGN OF IMAGING SYSTEMS

Nina Sultanova, Stefka Kasarova, Ivan Nikolov, Radostin Kasarov
E-mail: sultanova@btu.bg

ABSTRACT

Optical characteristics of different polymers have been studied to facilitate designers in material selection. Transmittance and refraction have been measured in the visible and near infrared spectra. Essential dispersive parameters in lens design as Abbe numbers, relative partial and first order dispersions have been estimated in both spectral areas. Thermal sensitivity of polymers is evaluated by their thermo-optic and expansion coefficients, thermal “glass” and thermo-optical constants. Design examples of a hybrid glass-plastic and an all-plastic triplet are presented and aberrations are compared. A remote imaging Maksutov type mirror-lens teleobjective is synthesized and computed geometrical and wavefront aberrations illustrate the good image quality of polymer optics.

Key words: optical polymers, lens design, design parameters

INTRODUCTION

Selection of optical polymers (OPs) in lens design is based on knowledge of their optical and material properties. They have already successfully replaced glass not only in consumer but in high quality optics [1, 2]. Injection moulding technologies offer a low-cost alternative to glass with some additional advantages such as reduced weight, high impact resistance, greater range of configuration possibilities and ability to integrate proper optical and mechanical features. However, some limitations in usage of OPs in lens design should be considered, such as restricted refractive index range, low scratch resistance, high hygroscopicity, ultraviolet degradation, etc. The weakest area of OPs is their much higher temperature sensitivity in comparison with glass. Thermal instability of polymer components is a result from the change of the refractive index value and the consequent alteration of optical power, as well as from the material thermal expansion. Reduction of thermal effects is possible in hybrid glass-plastic optical systems and proper choice of housing materials. Polymer films are used for reproducing unique geometric surfaces over glass components in high-performance imaging optics or in production of optical sensors, fibers and waveguides.

We have investigated the optical and some material properties of principal polymers such as polymethyl methacrylate (PMMA), polystyrene transmission decrease occurs beyond 2200 nm due to the absorption of the material functional groups.

(PS) and polycarbonate (PC), copolymers styrene acrylonitrile (SAN) and methyl methacrylate styrene (NAS), many trademarks, such as CTE-Richardson, Zeonex, Optorez, NAS 21 Novacor, Bayer, and some development materials produced by the USA Eastman Chemical Company (ECC). Different measuring techniques were used to obtain precise refractometric data of bulk polymers and thin films in the visible (VIS) and near-infrared (NIR) regions. Dispersive characteristics used in lens design have been estimated. Thermal sensitivity of OPs is analysed on the basis of their thermo-optic and expansion coefficients, thermal “glass” and thermo-optical constants.

The selection of appropriate OPs in lens design is illustrated on the basis of examples of all-plastic and hybrid glass-plastic objectives. Computing of geometrical and wave aberrations is accomplished to ensure image quality of the designed optical systems.

OPTICAL MATERIAL CHARACTERISTICS OF POLYMERS

The most important optical material characteristics in lens design are spectral transmission, refractive index (RI) and dispersion. Measured spectra of ECC thin polymer films show about 85 % transmittance in the range of 400 – 2000 nm [3]. There are some weak absorption bands between 1660 and 1700 nm and a considerable

We have measured RIs of polymer bulk samples and thin films at 22 wavelengths in the interval 406÷1320 nm. Pulfrich refractometer with an instrumental error of 2×10^{-5} at spectral lines in VIS light and a goniometric set-up with interference filters up to 1052 nm and uncertainty of 3.6×10^{-4} have been used to obtain precise RI data [4]. Three- and four-wavelength laser microrefractometers have been applied to measure RIs of thin ECC films with accuracy of 2×10^3 . The results show some differences in refraction of bulk samples and polymer layers for the same material. RIs of bulk samples at six measuring wavelengths are included in Table 1. Designers select OPs on the basis of RI values and Abbe numbers in the desired spectral range. In VIS area refraction at Fraunhofer's F-, d-, C-lines and v_d are presented and in NIR region RIs at measuring wavelengths are considered with an Abbe number defined as: $v_{879} = (n_{879} - 1) / (n_{703} - n_{1052})$. Relative partial dispersions $P_{d,C}$ and $P_{s,t}$ are calculated to combine OPs in achromatic pairs. Absolute values of first order dispersions $dn/d\lambda$ at d-line and 879 nm are computed for comparative analysis of dispersive properties in VIS and NIR wavelengths λ .

by the relation $R = (n-1)^2 / (n+1)^2$. In the VIS area values are slightly higher in the decimal part of R .

Thermo-optic coefficients (TOCs) dn/dT of studied OPs are estimated on the basis of our RI measurements in the range 10÷50°C at increasing temperature T by 5 °C. The results are of two orders of magnitude higher than those of glasses (see SCHOTT glass N-BK10 in the table), but they are always negative. A variation of TOCs with λ is noticed and a slight change of dispersion is established. Linear α and volume β thermal expansion coefficients of OPs are evaluated on the basis of Lorentz-Lorenz equation since for polymers $\beta \approx 3\alpha$ is always one or two orders of magnitude larger than the temperature coefficient of polarizability [4]. Thermal "glass" constant γ represents the normalized optical power ϕ change of a thin lens to unit ϕ and unit change of T : $\gamma = d\phi/\phi dT = (dn/dT)/(n-1) - \alpha$. The thermo-optical constant $G = \alpha(n-1) + dn/dT$ is an approximate measure of the sensitivity of the material to radial gradients and quantifies the optical path difference with T [5]. The results at d-line are included in the table. Reduction of the thermal effects is possible in hybrid glass-plastic systems

Table 1. Refractive indices, dispersive and additional optical parameters of optical polymers

Optical parameters	PMMA	Optorez 1330	Zeonex E48R	SAN	PC	Bayer	PS	N-BK10
n_F	1.4973	1.5163	1.5376	1.5783	1.5994	1.5998	1.6056	1.50296
n_d	1.4914	1.5094	1.5309	1.5667	1.5849	1.5857	1.5917	1.49782
n_C	1.4890	1.5065	1.5282	1.5623	1.5793	1.5803	1.5862	1.49552
n_{804}	1.4843	1.5031	1.5234	1.5543	1.5703	1.5718	1.5775	1.49212
n_{879}	1.4835	1.5017	1.5224	1.5526	1.5683	1.5698	1.5756	1.49083
n_{1052}	1.4813	1.4984	1.5204	1.5496	1.5645	1.5660	1.5718	1.48837
v_d	59.2	52.0	56.5	35.4	29.1	30.0	30.5	66.95
v_{879}	96.7	71.7	100.5	66.6	54.6	54.8	55.9	83.2
$P_{d,C}$	0.289	0.296	0.287	0.275	0.279	0.277	0.284	0.3093
$P_{s,t}$	0.217	0.306	0.202	0.175	0.179	0.185	0.186	0.3224
$ dn_d/d\lambda , \times 10^{-5} \text{ nm}^{-1}$	5.75	4.74	6.06	10.13	11.59	10.64	11.04	3.87
$ dn_{879}/d\lambda , \times 10^{-5} \text{ nm}^{-1}$	0.97	1.87	1.07	1.70	2.37	2.53	2.42	1.60
$R(879)\%$	3.8	4.0	4.3	4.7	4.9	4.9	5.0	3.9
$dn_d/dT, \times 10^{-4} \text{ K}^{-1}$	-1.30	-1.20	-1.26	-1.10	-1.00	-1.20	-1.31	0.034
$\alpha, \times 10^{-4} \text{ K}^{-1}$	0.75	0.66	0.66	0.53	0.47	0.56	0.60	0.058
$\gamma, \times 10^{-4} \text{ K}^{-1}$	-3.39	-3.02	-3.03	-2.47	-2.17	-2.61	-2.81	0.010
$G, \times 10^{-4} \text{ K}^{-1}$	-0.93	-0.86	-0.91	-0.80	-0.73	-0.87	-0.95	0.063

For a higher power efficiency of polymer components reflectance is calculated at 879 nm

and with a proper choice of housing materials.

OPTICAL DESIGN

The aim of optical design is to ensure object imaging with the highest possible contrast and negligible distortion. In Fig. 1a the layout and geometrical aberrations of a hybrid 3x magnifier for night-vision goggles with a back focal length $f' = 104$ mm and numerical aperture $NA = 0.24$ are presented. It consists of a polymer doublet built by PMMA and PS, and a convex-plane N-BK10 glass lens. The selection of OPs in the achromatic polymer pair is accomplished on the basis of v_d and $P_{d,c}$ values (Table 1). For the synthesis of a triplet, after calculation of the achromatic doublet, the scheme is determined by the

triplet's achromatization condition. The PMMA polymer and N-BK10 glass have similar dispersive characteristics and the obtained spherochromatic correction is rather good but there is some energy scatter for the out of axis views because of the arising coma. The spot diagram analysis and radial energy distribution are illustrated in Fig. 1b. The blur spot size is about 0.006 mm on the axis view. For a comparative analysis, an all-plastic optimized triplet built by PMMA-Bayer-PMMA has been calculated with similar parameters $f' = 100.2$ mm and $NA = 0.24$. In VIS area the system has a blur spot of 0.019 mm on the axis and the maximal geometrical spot size is 0.136 mm over the image field

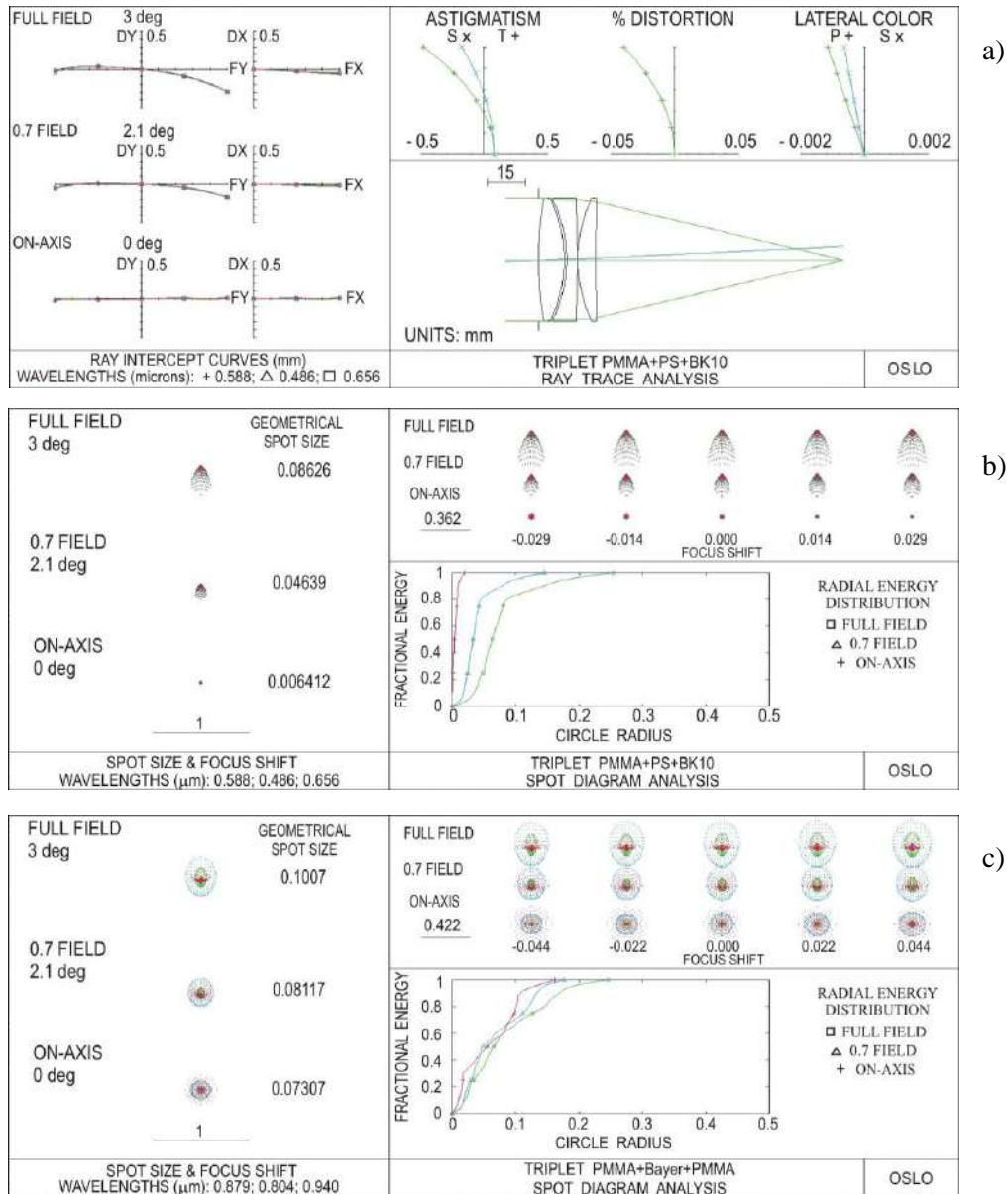


Fig. 1 Triplet design: a) VIS hybrid triplet layout and residual geometrical aberrations; b) spot diagram analysis of PMMA-PS-BK10 triplet; c) geometrical spots under 0.1 mm of the all-plastic NIR triplet PMMA-Bayer-PMMA, used for comparison

but its coma correction is poorer. Spot diagrams in NIR are presented in Fig. 1c. The dispersion characteristics of OPs are different in this part of the spectrum and it is difficult to minimize the triplet's sphero-chromatic aberrations.

The all-plastic 110 mm Maksutov type objective (Fig. 2), operating at a focal length of 300 mm and relative aperture 1:3, is intended for remote sensing of ground areas contaminated with biological agents. The optical system is focused at a distance of 5 m and object height is up to 5 mm. It consists of a PC primary mirror sputtered with aluminum reflective layer and silicon oxide anti-abrasive film and a PMMA double-lens aberration and achromatic compen-

sator. The telescope may be used in a large spectral area which is limited only by the PMMA transmission. Objectives with excellent optical characteristics and aberration correction in the full field of view are required for remote sensing devices. The Maksutov imaging objective gives nearly diffraction-limited performance for all wavelengths and fields as shown in Fig. 2b, c.

SUMMARY AND CONCLUSIONS

The selection of OPs in lens design is considered on the basis of their refractive, dispersive and thermo-optical characteristics in VIS and NIR region (Table 1). Presented Abbe numbers,

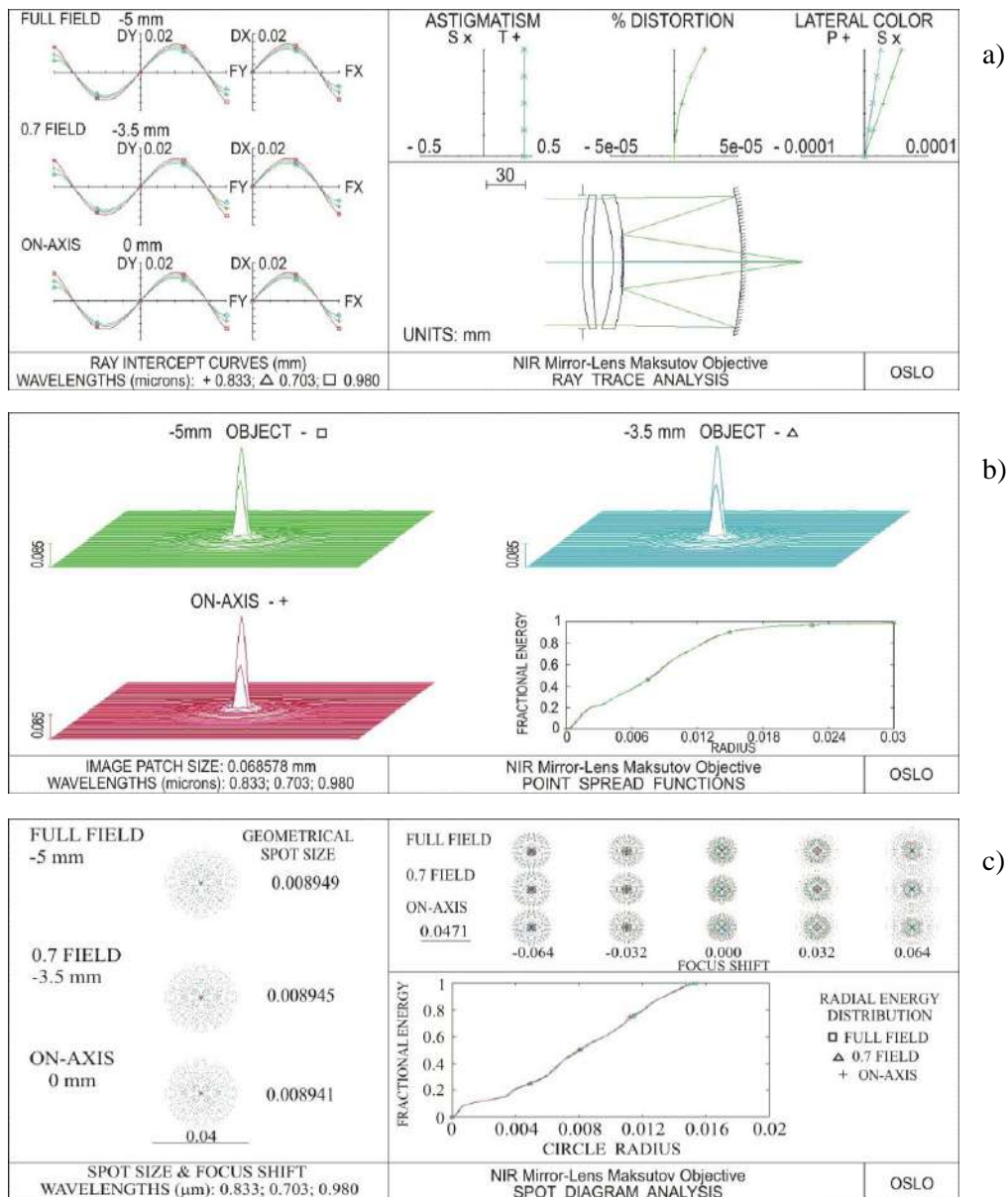


Fig. 2 NIR mirror-lens remote imaging objective with a PC mirror and a PMMA double lens aberration and achromatic compensator: a) optical layout with aberration corrections; b) point spread functions; c) spot diagram analysis

relative partial and first order dispersions are used in the design of plastic and hybrid glass-plastic objectives. TOCs, thermal expansion coefficients, thermal “glass” and thermo-optical constants, reflectance are determined on the basis of refractometric measurements. A comparison with the properties of a crown type glass is presented. In VIS area OPs show greater dispersion than glasses but in NIR region some polymers such as PMMA, acrylic and polyacrylate of ECC, as well as Zeonex E48R reveal lower dispersion according to their Abbe numbers and first order dispersions at 879 nm. Therefore, OPs are suitable materials for high-performance imaging optics in the NIR spectrum.

Incorporation of OPs and glasses in hybrid systems integrates lower weight and manufacturing cost, a broader service temperature range and a better correction of aberrations (Fig. 1). The proper selection of optical materials allows for minimization of sphero-chromatism and residual monochromatic aberrations in the developing system. The obtained sphero-chromatic charts and lateral colour corrections are rather good. A comparison with an all-plastic PMMA-Bayer-PMMA triplet is accomplished. The obtained correction of aberrations is satisfactory. In Fig. 2a a Maksutov type mirror-lens all-plastic teleobjective is presented. Limited geometrical and

wave aberrations are obtained. The presented examples of optical design confirm that the application of OPs does not pose a restriction on image quality of polymer optics and the arising aberrations could be minimized.

REFERENCES

1. Kuna, L., C. Leiner, S. Ruttloff, W. Nemitz, F. Reil, P. Hartmann, F. Wenzl and C. Sommer. *Polymer Optics and Molded Glass Optics: Design, Fabrication, and Materials 2016*, International Society for Optics and Photonics, 2016. p. 99490C.
2. Minami, K. *Optical plastics*, in Handbook of Plastic Optics, S. Bäumer (Ed.), Wiley-VCH, Frankfurt, 2005, pp. 109-147
3. Nikolov, I., N. Sultanova and S. Kasarova. *SES 2011*, Proceedings of the Tenth Scientific Conference with International Participation “Space, Ecology, Safety”, 2014, pp. 473-478.
4. Sultanova, N., S. Kasarova and I. Nikolov. *Refractive Index Metrology of Optical Polymers*, Lap Lambert Academic Publishing, Saarbrücken, 2014.
5. Rogers, P. and M. Roberts. *Thermal compensation techniques*, in Handbook of Optics, M. Bass (Ed. in chief), vol. I, McGraw-Hill Inc., New York, 1995, pp. 39.1-39.17.

NUMERICAL STUDY OF A SUBRECURSIVE SEQUENCE CONVERGING TO THE
EULER-MASCHERONI CONSTANT

Ivan Georgiev, Dimitar Yanakiev
E-mail: ivandg@yahoo.com

ABSTRACT

In this paper we study the practical applications of a sequence converging to the Euler-Mascheroni constant with subexponential convergence rate. Our main objective is to compute as many decimal digits of the constant as we can by using this sequence with a careful selection of the parameter values. Using software with arbitrary precision arithmetic we have obtained up to 118 correct decimal digits for relatively small values of these parameters.

Key words: Euler-Mascheroni constant, subrecursive class M^2 , computing decimal digits

INTRODUCTION

The subject of this paper is the estimation of the complexity of real numbers and real functions with respect to the narrow subrecursive class M^2 . The tools for this purpose are built in [7], where many significant real numbers are shown to be M^2 -computable and also the complexity of real functions is analysed by means of the class of the M^2 -substitutional operators. The first author has extended these tools to the class of rudimentary operators in [1] and has also studied the uniform M^2 -complexity of the generalised mean in [4]. In this paper we are interested in the complexity of the Euler-Mascheroni constant γ , which is defined by the equality

$$\gamma = \lim_{n \rightarrow \infty} \left(1 + \frac{1}{2} + \dots + \frac{1}{n} - \ln n \right),$$

and its value is approximately 0.57721566...

It is well-known that the above representation is not suitable for computing γ , since it has very slow convergence rate. The method of Vacca from [9] has M^2 -computable general term, but the convergence rate is not fast enough. The method of Karatsuba in [5] has a proper convergence rate, but its general term is not M^2 -computable. To overcome these difficulties, the first author has defined in [2] another fast converging sequence, which is suitable to prove M^2 -computability of γ . He builds this sequence by using results from [7] on the M^2 -computability of the elementary functions of calculus, together with the M^2 -analysis of integration in [3]. Our current aim is to check how many decimal digits of γ can be computed using this last M^2 -method.

For this purpose, we have used the Simulink package of Matlab with arbitrary precision arithmetic. The approximation process depends on the values of three parameters, which must be balanced appropriately to obtain the needed sufficiently small error.

M^2 -METHOD FOR γ

The M^2 -method from [2] begins with the integral representation

$$\gamma = -\int_0^{\infty} e^{-x} \ln x dx,$$

which is converted to the sum of two improper integrals of the form

$$\int_1^{\infty} f(x) dx,$$

where $f(x)$ is an analytic real function. For the two integrals we apply the same steps of approximation:

1. We replace the infinite bound by a finite real number, which we denote as $\xi + 1$.

2. We make a linear change of variables to obtain an integral of the form

$$\int_{-1}^1 \theta(x, \xi) dx.$$

3. By the *tanh-rule* from [8, Section 14] (another change of the variables), we produce

$$\int_{-\infty}^{\infty} \theta(\tanh t, \xi) \frac{1}{\cosh^2 t} dt.$$

4. We discretise the last integral by the trapezoidal quadrature rule with step h and we reach the following two-way infinite series

$$h \sum_{k=-\infty}^{+\infty} \theta(\tanh(kh), \xi) \frac{1}{\cosh^2(kh)}.$$

5. Finally we truncate this infinite series to its n -th (two-way) partial sum

$$h \sum_{k=-n}^n \theta(\tanh(kh), \xi) \frac{1}{\cosh^2(kh)}.$$

ESTIMATION OF THE ERROR

The error of the above method for computing the constant γ depends on the value of the three parameters ξ , h and n . It consists of three parts: the *chopping-off error* after step 1, the *discretisation error* from step 2 and the *truncation error* from step 3. Following [2, 3], the total chopping-off error for both integrals is at most

$$\frac{2\ln(\xi+1)+2}{\xi+1}.$$

The total discretisation error is at most

$$\xi \frac{2M\pi}{e^{\frac{2\pi a}{h}} - 1},$$

where $M = \ln(\xi+1) + 3.5$, $a = 0.25\pi$ and we have factored out ξ after the linear change in step 2 from the previous section. The total truncation error is at most

$$\xi \frac{4M}{e^{2nh} - 1},$$

where M is as above.

It is clear that to minimise the sum of the three errors, the three parameters must be chosen in non-trivial dependence on one another. For example, when h decreases, the discretisation error also decreases, but the truncation error increases (when n is fixed). This is why we will choose h to depend on n in such a way so that the two exponents in the denominator of the discretisation and the truncation error are the same. Solving for h we obtain

$$\frac{2\pi a}{h} = 2nh \Rightarrow h = \frac{\pi}{2\sqrt{n}}. \quad (1)$$

By summing the three terms above, we calculate the total error to be at most

$$\frac{2\ln(\xi+1)+2}{\xi+1} + \frac{\xi(\ln(\xi+1)+3.5)(2\pi+4)}{e^{\pi\sqrt{n}} - 1} \quad (2)$$

as a function of ξ and n .

Let us note that the value of h in (1) gives a better approximation than the value used in [2, 3], which is the reciprocal of the square root of n

(sufficient to prove M^2 -computability).

Now we want to balance the two summands of the last expression for the error by choosing a value for ξ as a function of n . We take

$$\xi = e^{\frac{\pi}{2}\sqrt{n}} - 1,$$

which is roughly the square root of the second denominator. Since

$$\frac{\xi}{e^{\pi\sqrt{n}} - 1} = \frac{1}{e^{\frac{\pi}{2}\sqrt{n}} + 1},$$

both denominators differ only by 1, which is negligible for values of $n \geq 10000$. The value

$\xi = e^{\pi\sqrt{n}} - 1$ gives practically no result, since after cancellation the second summand of the error is too big even for small values of n .

MAIN RESULTS

Based on the above observations we conducted our numerical experiment for calculating the decimal digits of γ by the M^2 -method for values of ξ of the form

$$\xi = e^{\alpha\sqrt{n}} - 1,$$

where α takes non-uniformly distributed values in the interval $(0, \pi]$. The values of n are 10000, 20000 and 30000, presented in three separate tables for each of these values. The value of h is fixed in (1) as a function of n .

Next to each value of ξ we give the number of correctly calculated digits of γ and also the error (2) from the last section, rounded to the nearest negative integer power of 10.

Table 1. Results for $n = 10000$

Value of α	Correct digits	Rounded error
$\pi/10$	11	10^{-11}
$\pi/8$	15	10^{-15}
$\pi/6$	20	10^{-20}
$\pi/4$	30	10^{-31}
$2\pi/5$	52	10^{-52}
$\pi/2$	65	10^{-64}
$3\pi/5$	78	10^{-51}
$3\pi/4$	99	10^{-30}
$5\pi/6$	111	10^{-19}
$7\pi/8$	86	10^{-13}
$9\pi/10$	69	10^{-10}
π	2	1

satisfactory for α in $(\pi/2, \pi]$. Another approach would be to optimize the values of the parameters in some other order. For example, we could optimize the value of h for each value of n separately and not use the fixed dependence (1) of h as a function of n .

ACKNOWLEDGEMENTS

This paper was supported by the Bulgarian Ministry of Education and Science under the National Research Programme "Young scientists and postdoctoral students", approved by DCM \# 577 / 17.08.2018.

REFERENCES

1. Georgiev, I., Computing real functions with rudimentary operators. *Annual of Assen Zlatarov University*, **44** (1), (2015), pp. 9-14.
2. Georgiev, I., Fast Converging Sequence to Euler-Mascheroni Constant. *Annuaire de l'Universite de Sofia "St. Kliment Ohridski" Faculte de Mathematiques et Informatique*, **104**, (2017), pp. 185-191.
3. Georgiev, I., On subrecursive complexity of integration. (submitted for publication in *Annals of Pure and Applied Logic*, 2019).
4. Georgiev, I., Uniform M^2 -computability of the generalised mean. *Annual of Assen Zlatarov University*, **47** (1), (2018), pp. 7-10.
5. Karatsuba, E., On the computation of the Euler constant. *Numer. Alg.*, **24**, (2000), pp. 83-97.
6. Knuth, D., Euler's constant to 1271 places. *Math, of Comp.*, **16**, (1962), pp. 275-281.
7. Skordev, D., Weiermann, A., Georgiev, I., M^2 -computable real numbers. *J. Logic and Computation*, **22** (4), (2012), pp. 899-925.
8. Trefethen, L., Weideman, J. A. C., The exponentially convergent trapezoidal rule. *Society for Industrial and Applied Mathematics*, **56** (3), (2014), pp. 385-458.
9. Vacca, G., A New Series for the Eulerian Constant. *Quart. J. Pure Appl. Math.*, **41**, (1910), pp. 363-368.

MONITORING OF THE NOISE POLLUTION IN ECOLOGY LABORATORY 327 IN THE INORGANIC CHEMISTRY BUILDING OF PROF. DR ASSEN ZLATAROV UNIVERSITY, BURGAS

Nikola Todorov, Veselina Yordanova, Vesela Manolova, Emine Ahmed, Mirela Toneva,
Stanislav Evtimov, Aneliya Stoyanova, Vladilena Deyanova
E-mail: steel_nick@yahoo.com

ABSTRACT

Noise is one of the main pollutants of the environment. It has a substantial effect on the quality of execution of highly intellectual tasks carried out in universities, as well as on the health of students and lecturers. In the present work, noise monitoring was performed in Ecology Laboratory 327 in the Inorganic Chemistry Building of Prof. Dr Assen Zlatarov University, Burgas. Internal and external noise sources were identified. Noise pollution from road traffic and the corridor was determined. A noise level was detected during teaching a different number of students. It was established that students and lecturers in Ecology Laboratory 327 were exposed to noise of 63-66 dB(A), which is 23-26 dB(A) higher than the limit value defined in the regulations of the Republic of Bulgaria. Measures for decreasing the noise pollution in the Inorganic Chemistry Building are suggested.

Key words: noise effect, intellectual labour, students and lecturers, annoyance

INTRODUCTION

The work of students and lecturers in higher education is highly intellectual, sensory and with a high emotional load. It requires focus, attention, high mental concentration and logical thinking [1-3]. The human mind processes every sound coming from the surroundings. unwanted sounds are considered as noise. When people are exposed to noise they are distracted, and long exposures to noise cause loss of concentration. This is a normal human physiological response, especially during intellectual activities. It is harder for the inattentive students to understand the matter taught or the assigned task, their cognitive abilities are also reduced. Frequent lack of concentration has a negative effect on students' psyche – it causes annoyance and anxiety about coping with the matter and demotivates them to achieve better results [4 - 7].

Noise also has a negative effect on the lecturers' health: it obstructs their mental activity, which results in a rapidly occurring fatigue and headache. Furthermore, raising the voice to overcome the noise causes extreme vocal exhaustion while teaching, which can be potentially harmful for the voice and throat. Noise can arouse a complex of symptoms called "noise sickness". In the initial period of this sickness, a partial loss of hearing occurs as well as a functional disorder in the nervous and cardio-vascular systems, to result later in a complete loss of hearing and dys-

function of the nervous system and other systems and organs [8-10].

According to research of the World Health Organization, noise is the second most hazardous pollutant in the environment (after particulate matter) causing health problems of the population [11]. To reduce the unfavourable effects of noise pollution, a number of regulatory documents have been adopted [12-14]. Order No 6 from 26.06.2006 [15] states that the highest permissible noise level in an auditorium in educational and scientific organizations is 40 dB(A).

Back in 1968 when the Inorganic Chemistry Building was constructed in the outskirts of the city, this permissible value could have been met. In later decades, however, a number of changes took place, e.g. increase of transport traffic, increase of the number of students and technical appliances and equipment used in education. At present, the noise levels in many auditoria, laboratories and studies in the Inorganic Chemistry Building of Prof. Dr Assen Zlatarov University, Burgas is substantially higher than the allowable limit. One of these rooms is 327, known among students and lecturers as Ecology Laboratory 327 (EL 327). A major part of the lectures and laboratory practice of the students doing "Ecology and preservation of the environment" and "Ecology and ecological management" take part in it. Lecturers and students have a good reason to ask: are the educational conditions in EL 327 ecological enough?

On this basis, the following main aims of the present work were formulated:

- ◆ to identify the main sources of noise in EL 327 in the Inorganic Chemistry Building;
- ◆ to estimate the noise pollution caused by these sources;
- ◆ to suggest measures for the reduction of noise pollution.

MATERIALS AND METHODS

Materials

◆ EL 327 is a room 5.75x6.20 m, located on the third floor of the Inorganic Chemistry Building of Prof. Dr Assen Zlatarov University, Burgas. Its window panes are made of 4-chamber PVC joinery with a double glass pack. There are 16 desks in it: 2 for the lecturers and 4 for the students. The laboratory is equipped with a laptop and a projector to be used during the lectures.

◆ A sound level meter – two pieces of model GM 1356 were simultaneously used. They have been manufactured according to standards IEC PUB651 TYPE2 & ANSI S1.4 TYPE2. Measuring range: 30-130 dB A; precision +/-1.5dB A; length of records: 1-250 seconds; memory: 4500 items. Connectivity: AC, PWM, USB. The USB port allows to save both recorded and real time measurement data for further processing and analysis.

◆ Software: noise level meter GM 1356 comes with installation disk of “Sound Lab” software. Using it, one can monitor the data collection in real time and download the data saved on the device, which can be further transformed in tables for processing. The data taken by the device are: number of the measurement, value measured, time and date of the measurement.

◆ Tripod on which the sound level meter is fixed.

Measurements

The sound level meter is fixed on the tripod and positioned at a height of 120 cm corresponding to the height of students’ ears. The measurement parameters are set:

- sampling rate – 1 per second
- total duration – 59 min (3540 samples). The experiment can be interrupted earlier than the deadline set.

The sampling starts at the beginning of every hour from 9:00 to 15:00 and lasts 59 min. The sound level is recorded as L, dB(A). The data are downloaded during the 1 min interval and this usually takes less than a minute. After that, the

memory of the device is erased and ready for the next sampling. The file names are formed as follows: date, number, start hour, number of students. Besides, the date, hour, minute and seconds are recorded for each sample.

All measurements were taken in May 2019. Measurements without students were carried out on two consecutive days (Monday and Tuesday) without interruption. The sound level measurements in the presence of students were taken with interruptions according to the following schedule: on Monday (from 9:00 to 12:00) and Tuesday (13:00 to 16:00) with the same group of students (7 3rd-year and 14 4th-year students).

Computer processing of the results

Using the USB port of the device and the software that comes with the sound meter, the raw data were downloaded to a computer. The software allows exporting the data in tabular form which can be further processed using spreadsheet programs such as MS Excel. The obtained values were transformed in dimension Leq, dB(A). It is possible to analyse different time intervals, e.g. 45 min (duration of an academic hour) or 15 min (duration of the break between the lectures).

RESULTS AND DISCUSSION

Determination of the monitoring points (MP)

To determine the monitoring points, it is necessary to find the noise sources. For EL 327 they were:

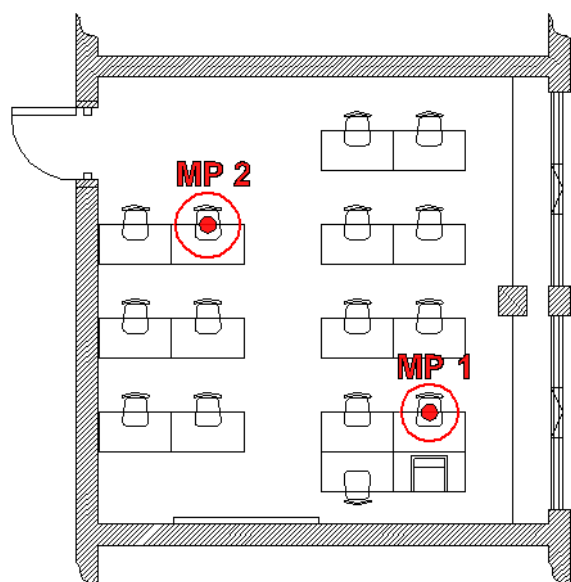
◆ external sources: road traffic noise, air traffic noise, noise from repair works outside the building, noise from the corridor and adjacent rooms resulting from talking and movement of students and lecturers, technical equipment, etc;

◆ internal sources: intercourse between students and lecturer, noise from notebooks and other aids, movement of chairs and tables, lecturer’s voice, noise from the computer and projector, noise from luminaire.

Monitoring points were determined to ensure the highest possible levels of noise pollution and the highest risk for the health of students and lecturers. Two measuring points were chosen, MP 1 was placed at the first desk by the window and MP 2 was placed at the third desk, nearest to the door (Scheme 1).

Both MPs were outside the direct sound field of the lecturer and located more than 1 m from the nearest reflecting surface in the room. Be-

sides, MP 1 received the highest impact from the noise coming from the computer and projector (smaller distance), from the road and air traffic and the repair works outside the building, because a window was often left open to air the room. MP 2 received the highest impact from the noise coming from the corridor (resulting from speaking and movement of students and lecturers) and repair works in the building.



Scheme 1. Monitoring points in EL 327

Evaluation of traffic noise

The main source of traffic noise was the road transport on international road E871, whose section behind the Inorganic Chemistry Building is also part of European road E773. To determine the exposition to traffic noise, the measurements were taken in days without any repair works. The time interval between 9:00 and 16:00 was selected because the largest number of students and lecturers are in the building and exposed to the noise during this period.

To find the effect of the traffic noise, measurements of sound levels L , dB(A) were taken under the following conditions:

a) background noise with windows closed (other conditions: door closed, no students or lecturers and no working technical devices);

b) background noise with one open window near MP 1 (other conditions: door closed, no students or lecturers and no working technical devices);

c) noise during a lecture with one window open near MP 1 (other conditions: door closed, one computer and one projector working).

From the results obtained, Leq , dB(A) was calculated. The results were compared (Fig.1).

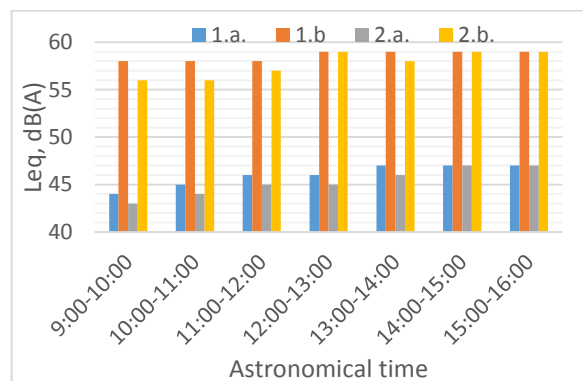


Fig.1. Equivalent sound level at the monitoring points 1 and 2 with closed windows (a) and one open window (b).

It can be seen from Fig.1 that Leq (closed windows and door) was between 44 and 47 dB(A) for MP 1 and between 43 and 47 for MP 2. These values are higher than the permissible limit of 40 dB(A) for the noise level in auditoria in educational organizations and scientific research organizations. (Order No 6/6.06.2006).

After opening one window, the Leq in the room increased to 56-59 dB(A). In both cases, a slight tendency of increase was observed until 14:00 and a little lower noise level measured by MP 2 which can be explained with its location away from the window.

Hence, at lectures with closed windows Leq was 57-60 dB(A), while with an open window, despite that only 7 students were present, the equivalent sound level reached 63-66 dB(A) (Fig. 2).

Under these conditions, the students made an effort to hear the lecturer and the lecturer tried to overcome the noise and, at some moments, the sound level L reached peak values of 85 dB(A).

For the purpose of the present work, sound measurements were also taken with two open windows and 14 students. The experiment was discontinued after 15 min due to the abnormal communication between the lecturer and the students. The equivalent sound level measured was 72 dB(A).

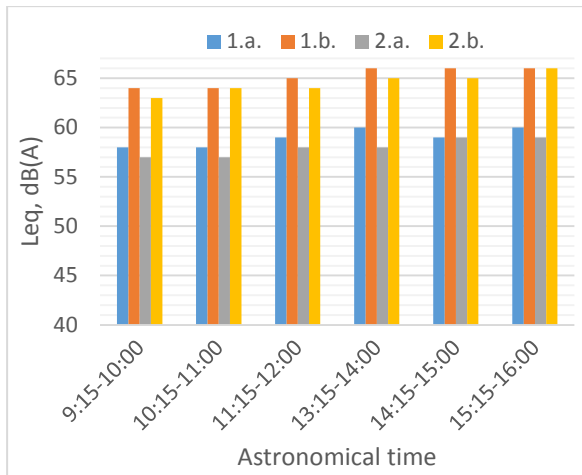


Fig.2. Equivalent sound level at monitoring points 1 and 2 during lectures with closed windows (a) and with one open window (b).

It can be concluded from the studies carried out that the traffic on the international road E871, which increases every year, is the main source of noise pollution in EL 327. The values measured were significantly higher than those required by the regulatory documents of the Republic of Bulgaria.

Evaluation of noise from the corridors

For the present study, measurements of noise levels were taken during the 15 min long breaks under the following conditions:

- door open, absence of students;
- door closed, presence of 7 students;
- door open, presence of 7 students.

The equivalent noise levels were compared (Fig. 3). Because of the small difference between values registered by MP 1 and MP 2, the figure shows only the results obtained at MP 2.

The rise of noise levels during a break can be seen in Fig. 3. There was a small margin between values registered by MP 1 and MP2, and for convenience only results from MP 2 are showed. It is easy to detect the difference between the three studied cases:

- Open door and absence of students – 54-57 dB(A);
- Closed door and 7 students – 60-62 dB(A);
- Open door and 7 students – 64-65dB(A).

The highest increase was in the intervals 12:00-12:15 and 13:00-13:15, which can be explained by the more active movement related to the lunch break. It can be seen that the students were noisiest during the third and fourth breaks. The conclusion drawn from these data was that the noise from the corridors during the break

increases the noise pollution by 3-6 dB (A) on average.

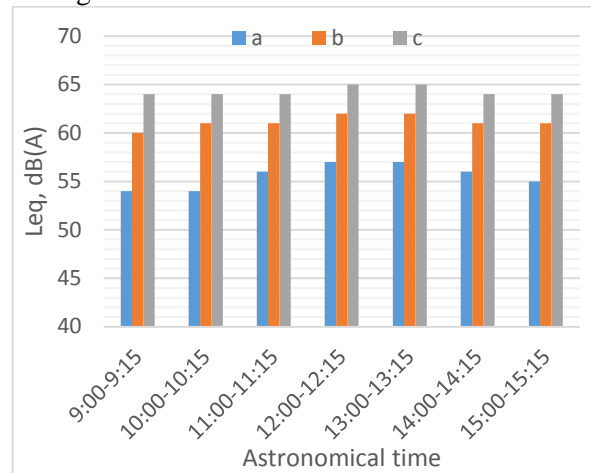


Fig.3. Equivalent noise levels at monitoring point

- 2 with open door and absence of students (a), closed door and 7 students (b) and open door and 7 students (c).

Evaluation of internal noise

To estimate the internal noise, sound level measurements were taken during lectures and during examinations, with 7 or 14 students and closed door and windows. Examinations usually continue for 3 hours and, in our case, they were of 3rd year students from 9:00-12:00 and 4th year students from 13:15 to 16:00 (Fig. 4). Both MPs measured the same noise level.

As can be seen from Fig. 4, Leq was in the range 48-50 dB(A) during an examination. The quietest period was the second hour and the highest sound levels were measured during the third hour. During the whole period, the requirements of Order No 6 and the Directives of the World Health Organization on Noise in the European Union were not met.

Sound levels were significantly higher during lectures. The noise from the computer and projector, the noise from students (intercourse, noise from rustling notebooks and other aids, movement of chairs and tables) and lecturer's speech increased the noise level to 56-58 dB(A) in the group of 7 students and to 59-62 dB(A) in the group of 14 students (Fig. 4c). The higher number of students was, the sound levels was higher and the lecturer had to raise his/her voice to overcome the noise in the room.

The results obtained from the study showed that the noise pollution generated by the technical devices, students and lecturer was about 10-12 dB(A). For the purposes of the present study, measurements were also taken with three open

windows in the presence of 14 students. The experiment continued for 15 min only due to the abnormal communication between the lecturer and the students. The average noise pollution measured was 74 dB(A).

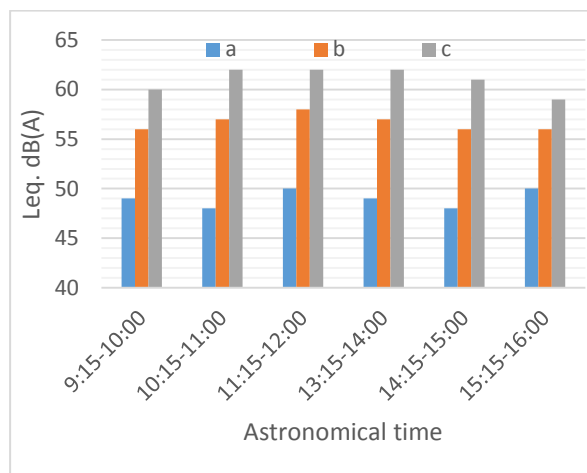


Fig. 4. Equivalent sound level during examination (a), lecture with 7 students (b) and lecture with 14 students (c).

Possible measures to decrease noise pollution in EL 327

Taking into account the adverse effect of noise on the physical and psychic state of the students and lectures, it is necessary to take urgent measures to limit the unfavourable effect of noise sources.

To minimize the exposure to traffic noise, it is necessary to create a green barrier between International road E871 and the Inorganic Chemistry Building. For this purpose, sound blocking plants (shrubs and trees) should be planted. To lower the internal sound levels, students must be aware of the effects of the noise pollution on the human ability to perform intellectual work, results, examination marks, working capacity and health. The installation of sound sensors to indicate noise levels exceeding 55 dB(A) is also necessary.

CONCLUSION

Students and lecturers of “Ecology and ecological management” who use EL 327 are exposed to noise levels of 63-66 dB(A). The highest noise pollution is generated by the traffic on international road E871 (14-15 dB(A)). The noise from the corridors during breaks increases the noise pollution by 4-6 dB (A) on average. The sound level during lectures depends on the number of students and Leq was measured to be in

the range of 62-64 dB(a) with 14 students and closed windows. All measured values were higher than the permissible limits stated in both Order No 6 for noise limits and the requirements of the World Health Organization.

To minimize the unfavourable effects of noise on the physical and psychic state of students and lecturers, it is necessary to create a green barrier of shrubs and trees between international road E871 and the Inorganic Chemistry Building, make students aware of the hazards and mount sound sensors with indication for noise levels exceeding the allowable values.

REFERENCES

- Hernandez E., I. Garcia, J. Navarro and E. Kolosovas-Machuca, Evaluation of noise environments during daily activities of university students, *International Journal of Occupational Safety and Ergonomics*, 2016, p.1
- Hodgson, M., R. Rempel and S. Kennedy, “Measurement and prediction of typical speech and background noise levels in university classrooms during lectures,” *Journal of Acoustical Society of America*, 1999, p. 226
- Juan, M., N. Lopez, L. Pavon, E. Tristan – Hernandez, Evaluation of acoustic quality in university facilities, *International Journal of Acoustics and Vibration*, 2018, p. 3
- Ozyonar, F., O. Gokkus, H. Muratcobanoglu, O. Gursoy, Assessment of On-Campus Noise Levels At Cumhuriyet University, *Fresenius Environmental Bulletin*, 2018, p. 3476
- Juan, M., N. Lopez, L. Pavon, E. Tristan – Hernandez, Evaluation of acoustic quality in university facilities, *International Journal of Acoustics and Vibration*, 2018, p. 3
- Hernandez, E., I. Garcia, J. Navarro, and E. Kolosovas-Machuca, Evaluation of noise environments during daily activities of university students, *International Journal of Occupational Safety and Ergonomics*, 2016, p.1
- Nuryadin, S., Effects of Classroom Noise on Teaching and Learning of High School Students in Jakarta, *International Journal of Science and Research*, 2016
- Xie, H., J. Kang, R. Tompsett, The impacts of environmental noise on the academic achievements of secondary school students in Greater London, *Applied Acoustics*, 2011, p.551
- Aparecida, E., M. Servilh, M. Delatti, College students' perception of classroom noise and its consequences on learning quality, *Audiol., Commun. Res.* 2014

10. Seetha, P., K. Karmegam, M. Ismail, S. Sapuan, N. Ismail and L. Tamil Moli, Effects to teaching environment of noise level in school classrooms, *Journal of Scientific & Industrial Research*, 2008, p. 659
11. https://ec.europa.eu/environment/noise/health_effects_en.htm
12. Directive 2002/49/EC of the European Parliament and of the Council of 25 June 2002 relating to the assessment and management of environmental noise
13. Law on Protection from Noise Pollution in the Environment.
14. Order No 54 / 13.12.2010 On National System for monitoring of environmental noise pollution, on requirements for conducting independent monitoring and providing information from industrial sources of noise in the environment.
15. Order No 6/26.06.2006 on environmental noise indicators taking into account the degree of discomfort during different parts of the day, limit values for environmental noise indicators, methods for assessing the values of noise indicators and the harmful effects of noise on public health (58/18/2006)

SYNTHESIS AND CHARACTERIZATION OF GRAPHENE

Irena Markovska, Fila Yovkova, Dimitar Georgiev, Magdalena Mitkova
E-mail: imarkovska@abv.bg

ABSTRACT

This paper proposes a technology for the production of monolayer graphene (from 1 to 5 layers) by an easy, accessible and non-toxic method. For the preparation of graphene, a combination of chemical and physical (ultrasonic) treatment of the original graphite precursor (>99%) was applied. During the treatment with dilute sulfuric acid, the Vandervaals bonds that bind graphene layers in graphite were loosened due to the introduction of molecules and ions from the acid between them. After the application of ultrasound, the Vandervaals bonds broke and the graphene monolayers became separated. Our research is focused mainly in the field of nanotechnology in connection with energy storage technologies, aiming to improve the electrical and capacitive characteristics of electrodes used in electric batteries, capacitors and supercapacitors.

Key words: graphene, ultrasound, acoustic cavitation, electrical resistivity

INTRODUCTION

Graphene is a single layer (monolayer) of carbon atoms, tightly bound in a hexagonal honeycomb lattice. Graphene is a new material for the synthesis of which the Nobel Prize in physics was granted to the Russian scientists Novoselov K.S. and Geim A.K. in 2010 after their publication in *Science* in 2004 [1].

Graphene belongs to the group of many topical present-day nanomaterials. Nanomaterials and nanotechnology have been identified as key enabling technologies in many technical applications, and are forecast to grow from a global volume of € 200 billion in 2009 to more than € 2 trillion nowadays [2, 3].

The first review of earlier literature relevant specifically to graphene was provided again by Novoselov K.S. and Geim A.K. in their articles [1, 4-5]. Graphene is an incredible material with many potential applications that continues to impress scientists around the world with its structure and composition. Graphene, a two-dimensional building carbon allotrope, shows potential applications in a wide range, including: touch panels, ultra-fast lasers, semiconductor devices and energy storage. This is due to its excellent physical and electrical properties, such as high thermal conductivity and high electron mobility [6, 7]. Some of the potential uses of graphene are described in Fig. 1 [8, 9].

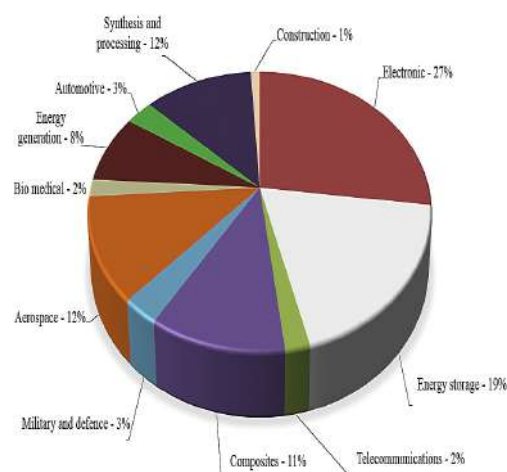


Fig. 1. Industrial applications of graphene-based materials [8, 9].

Graphene is an allotrope of carbon in the form of a plane of sp^2 -bonded atoms. In graphite (Fig. 2), the carbon atoms are in sp^2 hybrid state, which means that three of the four atom orbitals have interacted between themselves to form three new non-identical hybrid orbitals and one single p orbital remained unchanged. Graphite has a layered planar structure. It consists of stack planes arranged one above the other, called graphene planes, the carbon atoms of which are arranged in a densely packed two-dimensional hexagonal structure. The distance between the atoms in the lattice is about 1.42 Å and the distance between the planes is 3.35 Å [10].

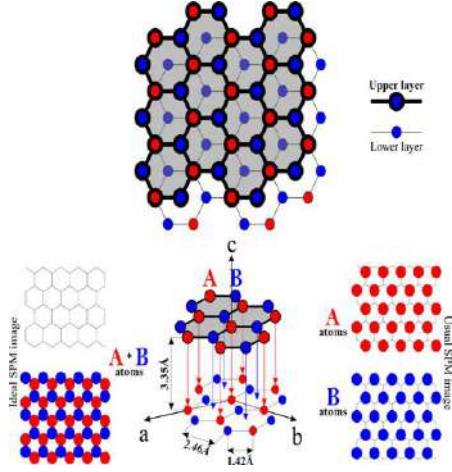


Fig. 2. Structure of graphite [10].

The carbon layers are held together in the direction of the main crystallographic axis “c” by weak Van der Waals forces, so they can easily be detached one from another under mechanical exfoliation.

EXPERIMENTAL

In the present work, a combination of chemical (using KOH or H₂SO₄) and physical impact on the precursor of the original graphite was applied to obtain graphene. Graphene production studies have been performed eliminating one of these stages, but the results are worse.

Theoretical background

An important role is played by the physical impact with ultrasound. Sonochemistry uses ultrasound to accelerate chemical reactions and initiate new reaction channels to increase the yield from chemical reactions and obtain new products with totally new properties, such as graphene. The main effect of the sonochemical reaction is caused by the acoustic cavitation which generates extreme physical conditions such as high temperature, high pressure, and shock waves accompanying the implosion of a cavitation bubble. A special physicochemical medium is created for the chemical reactions which cannot occur under normal conditions [11, 12].

Due to the effects of ultrasound, complex processes take place in the solutions, which leads to the formation of superfine graphene. The phenomena observed can be described as follows:

By application of ultrasound, a sound wave of high enough intensity propagates through the solution. A great number of cavitation bubbles is

generated in low pressure zones. These zones have variable geometry and complex dynamics due to the complex nature of the movements of the bubbles in the non-uniform pressure field.

Considering a single bubble which pulses driven by the variable acoustic pressure $p_a = p_0 \cos \omega t$, the change of bubble radius ξ is determined by the equation:

$$m \frac{\partial^2 \xi}{\partial t^2} + b \frac{\partial \xi}{\partial t} + k \xi = F(t) \quad (1)$$

For a bubble with average radius R_0 in liquid with density ρ , the effective mass is: $m = 4\pi R_0^3 \rho$, the modulus of elasticity is $\kappa = 12\pi\gamma R_0 P_h$, and the driving force is:

$$F(t) = -4\pi R_0^2 p_0 \cos \omega t \quad (2)$$

The resonance frequency is inversely proportional to the average radius of the bubble:

$$\omega_0 = \sqrt{\frac{k}{m}} = \frac{1}{R_0} \sqrt{\frac{3\gamma P_h}{\rho}} \quad (3)$$

Important parameters of the medium are the hydrostatic pressure P_h and the coefficient of non-linearity γ of the gas within the bubble.

The larger bubbles go up to the surface at a speed determined after the equalization of the lift and the Stokes force of friction for sphere:

$$v = \frac{2\rho_0 g R^2}{9\eta} \quad (4)$$

Smaller bubbles, in turn, can dissolve in the liquid and disappear. The behaviour of a bubble with radius R is stipulated by the pressures of the gases and vapours p_b in the bubble, by the hydrostatic pressure p_h in the liquid and by the surface tension σ . The difference between the internal and external pressures on the surface of the bubble is given by the equation:

$$p_b - p_h = \frac{2\sigma}{R} \quad (5)$$

For unsaturated liquids, the pressure of the dissolved gases is smaller than the hydrostatic pressure ($p_g < p_h$). It can be seen from eq. (5) that $p_h < p_b$. Therefore, the pressure of the gas in the liquid is smaller than the gas pressure in the bubble ($p_g < p_h < p_b$), so a diffusion of gas from the bubble to the liquid will be initiated, which will cause the bubble to dissolve and disappear.

To start the cavitation process, the pressure of gases and vapours in the bubble must be greater than the local hydrostatic pressure plus the surface tension forces, i.e.:

$$p_b \geq p_h + \frac{2\sigma}{R} \quad (6)$$

When the radius of the growing bubble reaches the resonance value of R_0 , the energy of the acoustic wave is absorbed very effectively due to the coincidence of the frequencies of the acoustic field and the bubble pulse. This results in a new abrupt increase of bubble size which disturbs the resonance and the energy influx becomes weaker. Without energy influx, the bubble becomes unstable and spontaneously collapses. The walls are torn, the liquid flows in and an implosion occurs together with the characteristic high temperature and pressure. The maximal local temperature and pressure can be assessed by the following formula:

$$T_{\max} = \frac{T_0 P(\gamma - 1)}{p_b} \quad (7)$$

$$P_{\max} = p_b \left[\frac{P(\gamma - 1)}{p_b} \right]^{\frac{\gamma}{\gamma - 1}}$$

Here, p_b is the pressure within the bubble before the implosion, $P = p_h + p_a$ is the pressure in the liquid and $\gamma = C_p/C_v$ is the coefficient of non-linearity of the gas in the bubble.

Sample preparation

Chemical treatment. As a chemical solution in ultrasound bath, KOH and H_2SO_4 were used. The precursor of graphite at samples G2 and G4 was put in KOH. In the second occasion, H_2SO_4 was used as a solution (samples G1 and G3).

The synthesized graphene samples were labelled G0, G1, G2, G3 and G4, respectively.

G0 – pure graphite (precursor);

G1 - graphene flakes from cup surface (treated with 2n H_2SO_4);

G2 - graphene flakes from the cup surface (treated with KOH);

G3 - graphene from the cup bottom (treated with 2n H_2SO_4);

G4 - graphene from the cup bottom (treated with KOH).

Fig. 3 shows a photograph of graphene on the bottom (G3) and on the surface of the cup (G1).



Fig. 3. Pictures of graphene on the bottom (G3) and on the surface of the cup (G1)

Physical treatment. Physical treatment was performed using ultrasound with a process duration of 1 to 8 hours.

RESULTS AND DISCUSSION

Sieve analysis of precursor of graphite

As a precursor we have investigated two types of graphite: commercial powder with a purity below 99% (No 1) and graphite (No 2), with a purity above 99%.

Using a sieving machine, 50.00g of each raw material were sieved for 15 min until completely passing through the sieves, and then the fractions from the individual sieves were weighed and their portion in the initial quantity was determined. The sizes of the openings of the sieves selected are shown in Table 1 together with the results obtained from the analysis.

Table 1. Sieve analysis of precursor of graphite, mass %

pre-cursor	Sieve with size of light opening, mm				
	>0,40	0,40	0,20	0,09 - 0,063	<0,063
graphite 1	0	4,35	67,9	15,05	12,7
graphite 2	0	11,5	80,4	1,85	6,2

It is well known that the smaller the particle size of the raw materials, the higher the graphene yield. It can be seen from the data in Table 1 that the fine fractions are predominant in the main raw materials – sizes from 90 to 200 μm for the present experiments, graphite 2 was selected.

Study of synthesized graphene X-ray analyses

The X-ray analyses were carried out by the method of powder diffraction using X-ray apparatus equipped D2 PHASER AXS- Bruker, with Cu anode and K_{α} emission, ($CuK\alpha$, $\lambda=1.5406\text{\AA}$). The following operating regime was used during the experiments: current 10 mA and voltage 30 kV.

Measurements of interplanar distances and diffraction peak intensities were made with the software package PowderCell v. 2.4. Phase analysis was performed using the PDF Powder Diffraction File (ICDD) to uniquely identify the present phases.

Table 2. X-ray analysis of samples G0, G1, G2, G3, G4

$d_{\text{teor.}}$ Å	G0	G1	G2	G3	G4
graphite	Int. exp.				
3.38	5250	2500	2900	3400	4250
2.12	250	125	125	125	200
2.02	200	100	100	100	180
1.69	125	70	70	50	70
1.227	50	20	20	20	30

The results of X-ray analyses are presented in Table 2. When graphene is a monolayer, it cannot be determined using X-ray structural analysis because there is no crystal lattice. This is also the case in our experiment - only residual graphite peaks are observed on the diffraction patterns of the samples tested. There are no peaks of graphene oxide, nor reduced graphene oxide. The reference value of the most intense peak for 100% intensity appeared at $d_{\text{teor}}=3.37\text{\AA}$. In our diffractograms, the peak at $d=3,378\text{\AA}$ belongs to graphite – pure graphite (G0). For composition G1, d appeared at 3.38\AA , for composition G2 $d=3.41\text{\AA}$, for composition G3 $d=3.41\text{\AA}$ and for composition G4 $d=3.399\text{\AA}$. The intensity of the characteristic peak of graphite is highest for pure graphite -0 ($I=5250$). The peak of G1 has the lowest intensities. The sequence is as follows: G1 ($I=2500$) <G2 ($I=3000$) <G3 ($I=3750$) <G4 ($I=4250$).

Optical Microscopy

Using an optical Celestron 5 MP LCD Deluxe Digital Microscope two samples with composi-

tion G2 and G4 were examined in order to evaluate the differences in the morphological characteristics.

The microscopic analyses of graphene with compositions G2 and G4 are presented in Fig. 4. The graphene sample with composition G2 and G4 was placed on a glass slide and examined with light microscope.

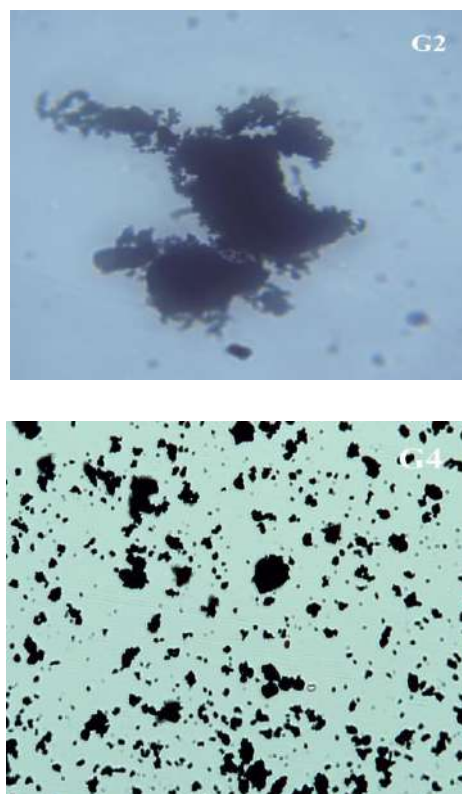


Fig. 4. Optical image of graphene samples with compositions G2 and G4

The sample with composition G2 is a cluster of graphene layers scattered on the glass plate, while the sample with composition G4 is a multitude of smaller clusters scattered on a glass slide.

Determination of electrical resistivity

In order to use the synthesized graphene for the purposes of energy storage, its electrical characteristics (electrical resistance, in particular) were examined. A series of graphene samples were prepared by the above described technology (S2, S4 and S6) as well as pure graphite samples. The electrical resistance of graphene samples was found to be several times lower than that of pure graphite (precursor).

The results in Fig. 5 give reason to believe that the graphene obtained according to the described technology can find application for various purposes, such as: electrodes for supercapac-

itors; integrated circuit component; graphene sensors (gas, bio and light); an anode for lithium-ion batteries, etc.

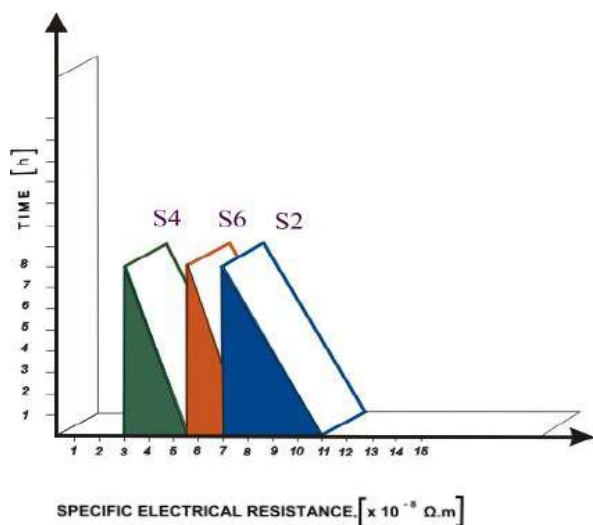


Fig. 5. Determination of the electrical resistance of graphene

CONCLUSIONS

Graphene was synthesized using pure graphite as precursor (with purity >99%).

The combination of chemical and physical (ultrasound) impacts on the precursor of the initial graphite was applied for the preparation of graphene.

By the treatment with diluted sulfuric acid, the van der Waals bonds which hold the graphene layers in graphite are weakened due to the introduction of molecules and ions from the acid between them, and by application of ultrasound, individual layers of graphene are separated, thus avoiding its oxidation to graphene oxide which worsens the electric conductivity of graphene.

Raman spectra proved the graphene synthesized.

Profound studies were carried out on the possibility to improve the capacitive characteristics of supercapacitors using graphene covering.

ACKNOWLEDGEMENTS

This work was supported by the Bulgarian Ministry of Education and Science under the

National Research Programme "E+: Low Carbon Energy for the Transport and Households, and by National Research Programme "Young scientists and postdoctoral students", both approved by DCM # 577 / 17.08.2018"

REFERENCES

1. Novoselov K.S., A.K. Geim, S.V. Morozov, et al., *Science*, **306** (2004), pp. 666-669.
2. Falkner R., N. Jaspers, *Regulating Nanotechnologies: Risk, Uncertainty and the Global Governance Gap*, *Global Environmental Politics*, **12** (1), (2012), pp. 30-55;
3. Petkova, St., Bl. Ramon, *Nanotoxicology and regulatory issues of emerging technologies*, *Annual of The Organization for Prohibition of Chemical Weapons*, Hague, Holland, (2013) pp.1-43.
4. Geim A. K., *Graphene prehistory*, *Phys. Scr.* **146**, (2012), pp.1-3.
5. Geim A.K., K. S. Novoselov, *Nature Mater.* **6**, (2007), pp.183-191.
6. Zhan H., F. Ding, H. Li, F. Qu, H. Meng, H. Gu, *Controlled synthesis of monolayer graphene with a high quality by pyrolysis of silicon carbide*, *Materials Letters*, 1 June 2019, volume 244, pp. 171-174.
7. Özkaya S., E. Blaisten-Baroja, *Polypyrrole on graphene: A density functional theory study*, *Surface Science*, **674** (2018) pp. 1–5.
8. Xiang Z., S.R. Bhavatharini, H. Liu, S. Ramakrishna, *Graphene's potential in materials science and engineering*, *RSC Adv.*, **55**, (2014), pp. 28987-9011.
9. Dasari B. L., J. M. Nouri, D. Brabazon, S. Naher, *Graphene and derivatives - Synthesis techniques, properties and their energy applications*, *Energy*, **140**, (2017), pp. 766- 778.
10. <http://pysicsopenlab.org/2018/01/31/graphite-structure/>
11. Saalbach K. A., J. Twiefel, J. Wallaschek, *Self-sensing cavitation detection in ultrasound-induced acoustic cavitation*, *Ultrasonics*, **94** (2019), pp. 401–410.
12. Saalbach K.A., P. Freytag, K. Kerber, J. Twiefel, *Ultrasonic assisted simultaneous composite casting-A feasibility study*, *Ultrasonics Symposium (IUS), 2012 IEEE International, IEEE*, (2012), pp. 775–777.

SYNTHESIS OF HIGHLY POROUS DIELECTRIC CERAMIC MATERIALS WITH RICE HUSK AS PORE-FORMER

Fila Yovkova, Irena Markovska, Dimitar Georgiev, Dimitar Rusev, Magdalena Mitkova

E-mail: fila_03@abv.bg

ABSTRACT

Dielectric material is an important part of condenser components. The present work reports the synthesis of high porosity dielectric ceramics with a main phase of mullite. Burned rice husk ash was used as a pore-forming agent. γ -Al₂O₃, technological waste from the petrochemical industry, was used as the basic material. Additive of 3% TiO₂ was added to corundum powder in order to obtain a solid solution and to reduce the synthesis temperature of the ceramics. The samples were studied mainly by X-ray analysis, SEM, DTA, FT-IR, etc.

Key words: dielectric ceramics, alumina, pore-former, rice husk

INTRODUCTION

Porous ceramic materials are important for a variety of applications, such as thermal insulation [1, 2], filtration [3], biomedical, catalyst substrates [4] and dielectric materials in capacitor elements. Capacitors are passive electronic components that can store electrical charge. The capacitor consists of two conductors, between which a different type of dielectric, including ceramic, is placed. The application of these ceramics is obviously determined by their unique structure [5].

The required porosity in ceramics can be obtained by the additives burning method. Organic materials such as rice husk, which are a by-product of the processing of rice, straw, sawdust, etc., are used as burners. Annually, about 500 million tonnes of rice are processed to obtain 100 million tonnes of rice husk [6].

The aim of the present work is to develop porous dielectric materials based on mullite ceramics.

MATERIALS AND METHODS

Materials

The initial materials used for the synthesis of porous ceramic materials were granules of pure and waste γ -Al₂O₃ (technological waste from the oil refining industry), SiO₂·nH₂O, TiO₂, and the pore-former was ash from rice husk burnt in air.

Methods

The initial γ -alumina and synthesized samples were studied mainly by X-ray analysis, SEM, infrared spectroscopy (FT-IR), differential thermal analysis (DTA) and optical microscopy.

The X-ray analyses were carried out by the method of powder diffraction using X-ray apparatus equipped D2 PHASER AXS- Bruker, with Cu anode and K α emission, (CuK α , $\lambda=1.5406\text{\AA}$). The following operating regime was used during the experiments: current 10 mA and voltage 30 kV.

Measurements of interplanar distances and diffraction peak intensities were made with the software package PowderCell v. 2.4. Phase analysis was performed using the PDF Powder Diffraction File (ICDD) to uniquely identify the present phases.

SEM - The morphology and microstructure of the rice husk were examined by scanning electron microscopy (SEM). The electron microscope photographs were taken using a Philips SEM525M/EDAX9900 scanning electron microscope with attached X-ray microanalyst. The microphotographs were taken in a regime of secondary electrons at acceleration of 20 kV.

FT-IR studies were performed on a Tensor 27 Fourier infrared spectrophotometer FTIR (Bruker, Germany) in the interval 400 – 4000 cm⁻¹ at resolution of 1 cm⁻¹. Measurements were carried out at room temperature. The sample (0.3 mg) was tableted with KBr (100 mg) at a pressure of 2-4 atm.

DTA experiments were performed on an apparatus for complex thermal analysis (STA 449 F3 Jupiter), NETZSCH, Germany by heating to 1100°C at a rate of 10°C min⁻¹.

EXPERIMENT

The two Al₂O₃ powder materials were prepared as follows: the pure and waste granules were washed with running water on a metal sieve to remove contamination and crude mechanical particles. Then the granules were dried at 120°C for 3 hours. The materials were ground by wet grinding in a Retsch planetary mill with corundum balls for 5 hours at a ratio of material : water : milling balls = 1:1:2. The ground aluminium oxide was dried at 120°C for 5 h.

As SiO₂ source, ash from oxidized rice husk was used. The rice husks studied are technological waste from the processing of Krasnodarsky 424 rice variety grown in Bulgaria [7]. The rice husks separated during the processing are ark shaped with the following approximate size: length about 8 mm, width about 2-3 mm and thickness about 0,10 – 0,15 mm. The husks studied contain mainly organic substances (cellulose, hemicellulose and lignin) and an inorganic part consisting of mostly SiO₂ (~20%) and 5.5% mixture of the following oxides: CaO, Fe₂O₃, MgO, Al₂O₃, Na₂O, K₂O, MnO₂, as well as traces of Cu and Pb.

Fig. 1 (A, B) shows photographs of rice husk burnt in air, at bigger (Fig. 1A) and smaller magnification (Fig. 1B). It can be seen from the two photographs that, after the separation of the organics, only the inorganic substances remain in

the husk which forms the silicon-oxygen carcass. The silicon-oxygen carcass (Si-O-Si) which builds the burnt husk can be quite clearly seen in Fig. 1B.

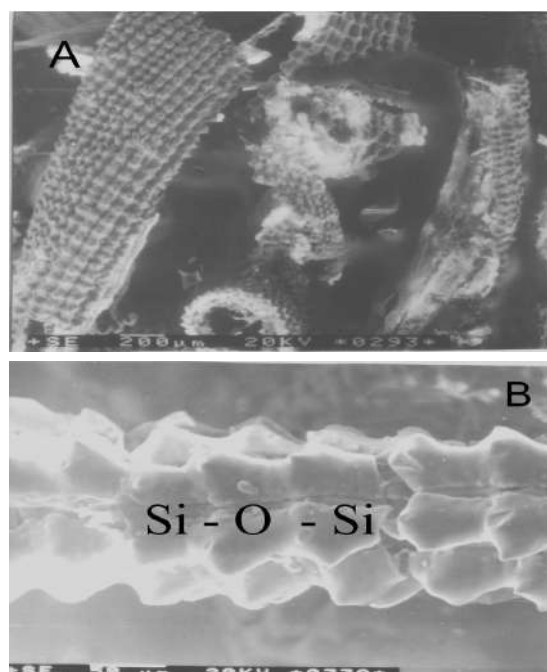


Fig. 1. CEM of oxidized rice husk

Composition of the blends

A number of blends were prepared for the study and a series of samples were synthesized under different conditions and combinations of the initial components, including different content of the pore-forming agent. Some of the blends are shown in Table 1.

Table 1. Composition of the synthesized samples

No of the sample	composition, mass. %				
	Al ₂ O ₃ -pure	Al ₂ O ₃ waste	- SiO ₂	TiO ₂	RHA
MC 5	70	-	30	3	10
MC 6	70	-	30	3	20
MC 7	-	70	30	3	10
MC 8	-	70	30	3	20

Formation and sintering of the samples

The initial materials (described in Table 1) were weighed, mixed and homogenized. Then, 4% aqueous solution of PVA was added as plasticizer and the mixture was semi-dry formed on a manually operated hydraulic press. The samples

obtained were dried in a desiccator under the following conditions: 80°C – 1h, 120°C – 1h, 180°C – 1h, followed by high temperature sintering at 1350°C. The aim was to obtain porous material with good mechanical characteristics at comparatively low synthesis temperature. The

sintering itself was carried out with several isothermal periods to prevent cracking of the sample by the burning of PVA and the pore-forming additives: isothermal periods of 30 min at 200°C, 30 min at 300°C, 30 min at 400°C, 30 min at 500°C, 30 min at 700°C, 30 min at 900°C and 60 min at 1350°C.

RESULTS AND DISCUSSION

Study of the initial materials

Using a sieving device, 100.00 g of each ingredient were sieved for 15 min, then the fractions on the individual sieves were weighed and determined as % of the initial amount. The results obtained from the analysis are presented in Table 2.

It can be seen from the data shown in Table 2 that the fractions with size between 125 and 315 μm were predominant in the basic materials.

As a pore-former, ash from rice husks was added, fraction 0.08 – 0.125 μm . White ash from rice husks obtained by burning raw husks in air at 500°C was used. Burning was carried out in a silit furnace at a heating rate of $-3^{\circ}\text{C}/\text{min}$. The aim was that burning was as complete as possible to obtain material of the highest quality. At this temperature, SiO_2 is in amorphous form which was proved by additional XRD analyses.

The experiments showed that the smaller the raw material particles size, the finer and more uniformly distributed porosity was produced in the sintered ceramics.

Blends compositions and sintering of the samples

A number of blends obtained from pure and waste oxide were prepared for the experiments and 4 series of samples were formed under different conditions and different combinations of the initial components, including content of pore-forming agent of 10% and 20%. Some of the blends are shown in Table 2, as selected according to the suitability of the sintered samples for the main goal of the study.

Table 2. Fractional analysis of initial materials, mass%

type	Sieve with the size of the light bore, mm					
	>	0,315-	0,2	0,125 -	0,08	<0,063
Raw material	>	0,315-	0,2	0,125 -	0,08	<0,063
ma-	0.3	0,20	0-	0,08	—	
terial	15		0,1		0,063	
			25			
Al_2O_3	26,	28,70	39,	5,73	0	0
3-	48		09			
pure						
Al_2O_3	49,	25,55	23,	1,88	0	0
3-	12		45			
waste						
SiO_2	22,	26,45	27,	23,89	0	0
	34		32			
TiO_2	0	0	16,	10.18	0	3.54
			28			

DTA of initial $\gamma\text{-Al}_2\text{O}_3$

Differential thermal analysis of the initial Al_2O_3 , pure and waste, was carried out to find out the processes taking place in them under heating. The results obtained from the thermal analysis are illustrated in Fig. 2.

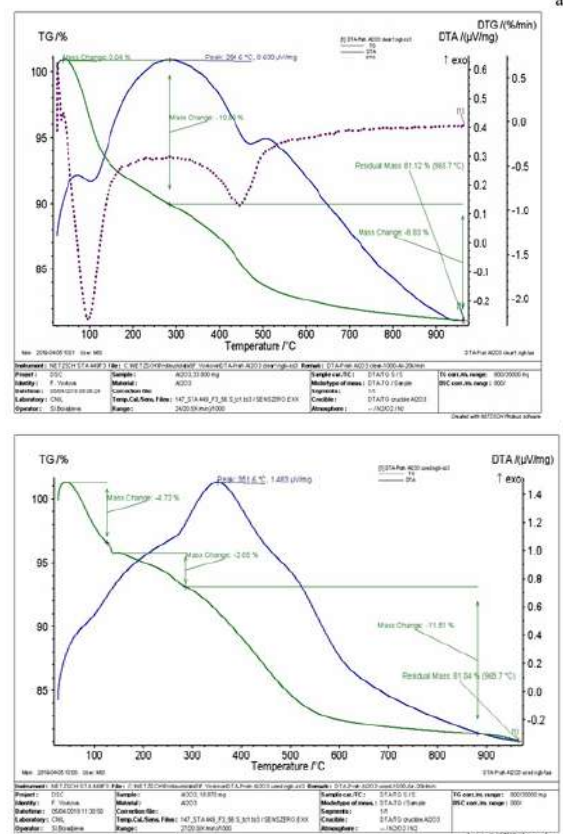


Fig. 2. DTA of initial $\gamma\text{-Al}_2\text{O}_3$: a) pure $\gamma\text{-Al}_2\text{O}_3$, b) waste $\gamma\text{-Al}_2\text{O}_3$

The thermal method shows the individual stages of weight loss occurring due to reactions of dehydration (separation of the adsorbed water) and the burning of the organics present in the initial powder. It can be seen from the DTA analysis of pure Al_2O_3 (Fig. 2a) that a wide endothermal effect was registered at about 110°C due to the release of the physically bonded water, which was accompanied by about 0.04% weight loss. The crystallization water evaporated at about 450°C , which was also indicated by an endothermal effect.

The curve obtained from the analysis of waste Al_2O_3 (Fig. 2b) has a wide endothermal effect at about 120°C , which indicates the release of the physically bonded water and the weight loss here was about 4.72%.

During the heating of the two kinds of aluminium oxide, exothermal effects were registered at 284.6°C (Fig. 2a) for the pure Al_2O_3 and at 351.6° for the waste Al_2O_3 (Fig. 2b). Both exoeffects were accompanied by about 11 % weight loss.

Study of the properties of the ceramics obtained X-Ray analyses

The data are shown in Fig. 3. All four samples showed diffraction maxima for three phases present at different contents: mullite ($\text{Al}_{4+2x}\text{Si}_{2-2x}\text{O}_{10-x}$, $x \approx 0.4$), cristobalite (SiO_2) and corundum (Al_2O_3). The references used were taken from the PDF ICDD library, as follows: mullite – Powder Diffraction File #15-1776; cristobalite – Powder Diffraction File #39-1425; corundum – Powder Diffraction File #46-1212.

The predominant phase in the ceramics was mullite accompanied by corundum and cristobalite phases, which are due to non-reacted Al_2O_3 and SiO_2 .

The lower sintering temperature of the ceramics was achieved by adding 3 mass% of TiO_2 in the initial blend. It forms a solid solution with corundum, thus facilitating the formation of defects in its lattice and, respectively, ease ceramics sintering at lower temperature. A higher content of this additive would cause deterioration of ceramics properties, namely poorer physico-mechanical properties due to the processes of recrystallization.

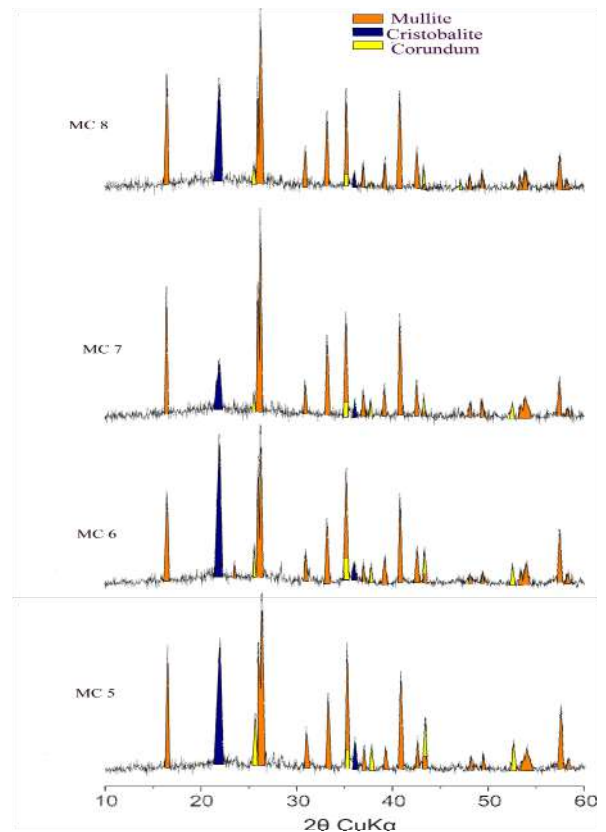


Fig. 3. Powder diffractograms of samples MC 5 ÷ MC8

Study of the ceramics surface

Fig. 4 shows photographs of surfaces of the samples synthesized with addition of 20% pore former (rice husks ash) to the initial pure or waste corundum powder. The microscopic studies of the ceramic samples surface shown in Fig. 4 were carried out with light microscope.

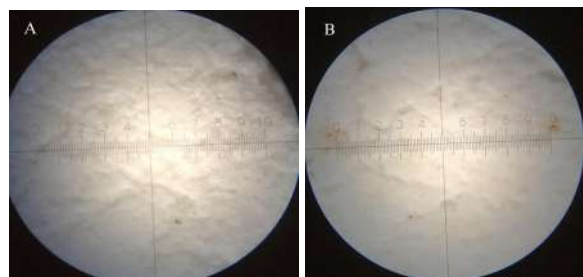


Fig. 4 Surface image of ceramic samples with 20% rice husk: a) MC 6 and b) MC 8

The photographs show that the surface of the samples made from pure oxide (MC6) was rougher and more inhomogeneous.

Determination of basic physicochemical properties

Some of the important physicochemical properties of the samples were determined, namely: water uptake (WU), apparent density (ρ_{app}) and apparent (open) porosity (P_{app}). The results obtained are presented in Table 3.

Table 3. Basic physicochemical properties of the samples

No of the sample	Water uptake, %	ρ_{app} , g/cm ³	porosity $_{app}$, %
MC 5	41.20	1.28	52.85
MC 6	45.92	1.24	56.97
MC 7	36.52	1.37	50.10
MC 8	39.73	1.34	53.32

As can be seen from Table 3, blends MC6 had the highest open porosity – 56.97%. In our study, a comparatively high open porosity and very good physicochemical properties were achieved due to the burning component added. By burning the rice husks, the residual non-burnt carbon in them burned down and releases carbon oxides, which gave the necessary porosity.

CONCLUSIONS

Based on the results from the experiments, the following conclusions were made: Porous mullite ceramics were synthesized using the burning additive method;

- The phase compositions of the synthesized porous materials were investigated by X-ray analysis;
- Besides mullite, synthesized ceramics contain corundum and α -cristobalite;
- It was found out that the composition based on pure aluminum oxide containing 20% ash of rice husk has the highest porosity;
- These materials are dielectrics and could be used as part of capacitor elements.

ACKNOWLEDGEMENTS

This work was supported by the Bulgarian Ministry of Education and Science under the National Research Programme “E+: Low Carbon

Energy for the Transport and Households”, and by the National Research Programme “Young scientists and postdoctoral students”, both approved by DCM # 577 / 17.08.2018”

REFERENCES

1. Ni, X., J.Wang, G. Liu, Z. Zhang, J. Shen, B. Zhou, G. Wu, Preparation and properties of super insulation material SiO₂ aerogel, *Advanced Materials Research*, **516-517**, (2012), p.1531-1535.
2. Tseng C. C., R.L. Sikorski, R. Viskanta, M.Y. Chen, Effect of foam properties on heat transfer in high temperature open – cell foam inserts, *J. Am. Ceram Soc.*, **95**, (6), (2012), p. 2015-2021.
3. Suzuki T., A dense cell culture system for microorganisms using a stirred ceramic membrane reactor incorporating asymmetric porous ceramic filters, *J. Ferment. and Bioeng.*, **82**, (3), (1996), p. 264-271.
4. Zhang L., Z. Mao, J.D. Thomason, S. Wang, K. Huang, Synthesis of a homogeneously porous solid oxide matrix with tunable porosity and pore size, *J. Am. Ceram Soc.*, **95**, (6), (2012), p. 1832-1837.
5. Roy Rice W., The Porosity Dependence of Physical Properties of Materials: A Summary Review, *Key Eng. Materials*, **115**, (1996),p.1-20.
6. Markovska I., F. Yovkova, G. Minov, D. Ru-sev, L. Lyubchev, Investigation of Silane Modified Ceramic Surface of Porous Mullite Ceramics, *World Academy of Science, Engineering and Technology (International Journal of Science, Engineering and Technology)*, **73**, (2013), p. 273 - 278. (SJR- 0.132).
7. Tsvetalina I., I. Markovska, Ts. Dimitrov, Synthesis and characterization of willemite ceramic pigments obtained by utilisation of bio-waste, *Annual of Assen Zlatarov University*, 2018, volume XLVII, book 1, p. 44- 49.

SYNTHESIS AND STUDY OF Co-DOPED WILLEMITE CERAMIC PIGMENTS

Tsvetalina Ibrevva, Tsvetan Dimitrov, Aleksander Karamanov, Georgi Avdeev
E-mail: cvetila@abv.bg

ABSTRACT

This study shows the possibility to synthesize Co-doped willemite ceramic pigments via solid-state high temperature sintering. The starting materials used for the synthesis of pigments were CoO, ZnO, Fe₂O₃, NiO, P₂O₅ and amorphous Si₂O.H₂O. In the synthesized pigments ZnO was substituted partially by CoO. The optimal parameters of the synthesis process were determined. The willemite ceramic pigments were studied mainly by X-ray analysis, scanning electron microscopy (SEM) as well as by the CIELab system of color measurement. It was found out that the synthesized pigments are suitable and can be successfully applied in glaze tiles and sanitary ceramics.

Key words: willemite pigments, CIELab color measurement, oxide additives, solid-state sintering

INTRODUCTION

Ceramic pigments are inorganic colored finely dispersed powders which, when added to some medium, impart certain color and change some of its properties. Beside their coloring ability, ceramic pigments are resistant to atmospheric and chemical influences, high temperatures, the decomposing activity of silicate melts and the effects of light [1 - 5]. These colored inorganic substances have a high coefficient of light refraction, they are insoluble in water, organic solvents and binding materials, but possess the ability to disperse in them and impart specific color.

In recent years, researchers from many countries work on the synthesis, characterization and properties of various kinds of willemite ceramic pigments prepared from both natural and waste materials [6, 7]. Willemite is a mineral, zinc silicate (2ZnO.SiO₂). It was discovered in the form of small brown crystals and named after the King of Holland Willem I (Willem Frederik) in 1830. Willemite can be green, yellow, brown, red-brown, orange, and blue. It can be found in nature as prismatic translucent and small needle crystals. It is one of the few silicates with orthogonal syngony, which is more characteristic of carbonates.

The ceramic pigments with structures of willemite 2ZnO.SiO₂ which crystalize in the trigonal syngony have been known for some time. Such is the widely used cobalt silicate 2CoO.SiO₂ with fine blue color. The color palette of willemite pigments today is quite large [8]. If zinc oxide is substituted with nickel oxide,

blue pigments which successfully compete with the more expensive cobalt pigments can be obtained. The introduction of FeO results in yellow and brown pigments and MnO in pink, purple and grey [8]. Attempts have been made to substitute not only ZnO but also SiO₂ with other acidic oxides such as SnO₂, TiO₂, ZrO₂ [9].

The aim of the present paper is to study the possibilities to synthesize blue willemite ceramic pigments from pure materials with respect to their possible use as pigments in the silicate industry.

MATERIALS AND METHODS

1. Materials

The synthesis of pigments is carried out by a solid state reaction using the following chemically pure initial materials: CoO, ZnO, SiO₂.2H₂O, Fe₂O₃, NiO, P₂O₅ и NaF. Amorphous Si₂O.H₂O was used as a source of SiO₂. In these synthesized pigments ZnO could be partially substituted by CoO.

The SiO₂ feedstock used in the system SiO₂.nH₂O is considerably more reactive than conventional quartz sand and has a particle size in the range of 2-7 μm. The mineralizer of NaF is used to reduce the temperature of the synthesis and accelerate the processes of formation of the new phase.

2. Methods

The willemite ceramic pigments were studied mainly by X-ray analysis, scanning electron microscopy (SEM) as well as by the CIELab system of color measurement.

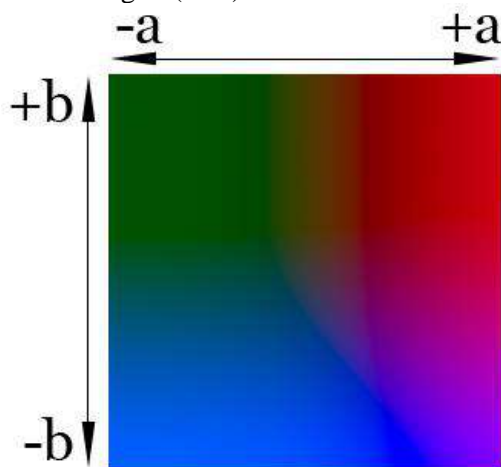
The X-ray analyses were carried out by the method of powder diffraction using X-ray apparatus equipped D2 PHASER AXS – Bruker, with Cu anode and K_{α} emission, (CuK_{α} , $\lambda=1.5406\text{\AA}$). The following operating regime was used during the experiments: current 10 mA and voltage 30 kV.

The morphology and microstructure of the pigments were investigated by scanning electron microscopy (SEM). The electron microscope photographs were taken using a Philips SEM525M/EDAX9900 scanning electron microscope with attached X-ray microanalyst. The microphotographs were taken in a regime of secondary electrons at acceleration of 20 kV.

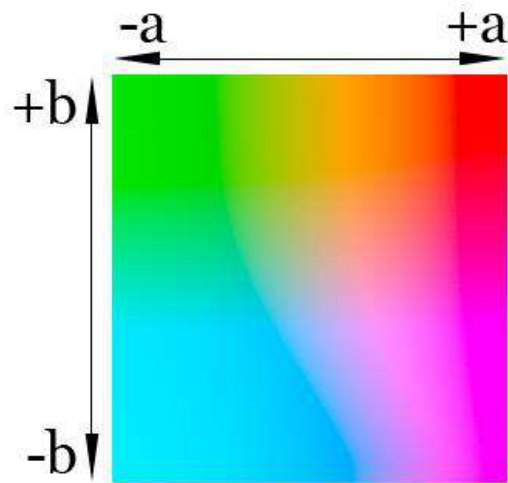
Color measurement. Color is one of the most important indicators of pigment quality. Colored substances absorb and convert light rays of a certain wavelength into the visible portion of the spectrum, due to their atomic structure. The CIELab system defines colors not only of ceramic pigments but also of other materials, which indicates that this system is universal and widely used. In the present paper the pigments color is determined spectrally with a Lovibond Tintometer RT 100 Color. The colour measurements were performed using the CIELab method. This method, which is the standard method in the ceramic industry, especially for ceramic pigments, allows to determine the whiteness and color degree of tiles by measuring the three parameters: L^* , a^* and b^* , where:

- L^* (brightness), from absolute white $L^* = 100$ to absolute black $L^* = 0$
- a^* - green color (-) / red color (+)
- b^* - blue color (-) / yellow color (+)

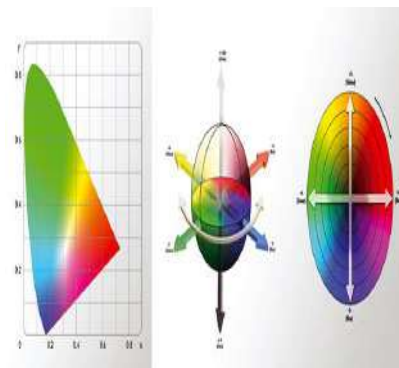
The color space of the CIELab system is shown in Fig. 1 (A-C).



A) brightness 25 %



B) brightness 75 %



C)

Fig. 1 (A, B, C) The colour space of CIELab system

EXPERIMENT

In order to obtain willemit ceramic pigments in the system $Co_0.Zn_0.SiO_2$ the composition of the blends was calculated. The following pigment compositions were prepared: $Co_0.Zn_0.SiO_2$, $Co_0.Zn_0.SiO_2.0.1Fe_2O_3$, $Co_0.Zn_0.SiO_2.0.1NiO$ and $Co_0.Zn_0.0.5SiO_2.0.5P_2O_5$. First, after calcination in a platinum crucible, the SiO_2 and H_2O content in $SiO_2.nH_2O$ was determined, as follows: $SiO_2 - 76.3\%$ and $H_2O - 23.7\%$. Quantities of the starting oxides, such as ZnO , CoO , Fe_2O_3 , NiO , P_2O_5 and $Si_2O.H_2O$ in the 100 g batch recipe were weighed to the nearest 0.1 g, then mixed and homogenized in a FRITCH PULVERIZETE6 planetary mill.

The composition of the samples is shown in Table 1.

Table 1. Composition of the samples

No of sample	Composition
1	CoO.ZnO.SiO ₂
2	CoO.ZnO.SiO ₂ .0.1Fe ₂ O ₃
3	CoO.ZnO.SiO ₂ .0.1NiO
4	CoO.ZnO.0.5SiO ₂ .0.5 P ₂ O ₅

The synthesis of pigments was carried out by the method of solid state sintering. The sintering of the initial blends was performed in a laboratory muffle furnace at heating rate 6°C/min and 1 h isothermal period at the final temperature. The pigments were sintered at 900°C and 1000°C. After sintering, additional homogenization was carried out in a planetary mill PULVERIZETE6, a product of FRITCH Co.

RESULTS AND DISCUSSION

X – ray analysis of the pigments

Fig. 2 shows the results obtained from X-ray phase analyses of the pigments. The X-ray analyses carried out showed that cobalt – willemite ceramic pigments were synthesized in the system $x\text{CoO} \cdot (2-x)\text{ZnO} \cdot \text{SiO}_2$, where $x = 1,00$.

It can be seen from the X-rays analyses that the main phase was a willemite and reflexes of the zinc silicate were also observed.

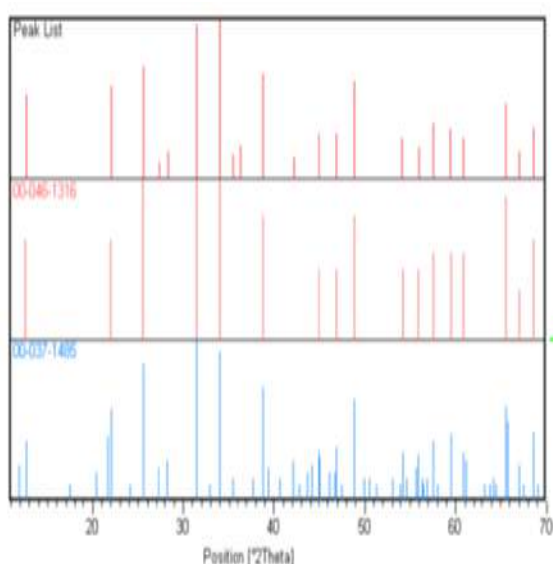


Fig. 2. XRD parents of Co – doped zinc silicate synthesized at 1000°C in the system CoO.ZnO.SiO₂: 00-046-1316 - willemite – (Zn, Co)₂SiO₄: 00-037-1485 zinc silicate Zn₂SiO₄

Color Measurement

One of the most characteristic properties of pigments is their color. In this respect, one of the most important studies of pigments is connected with the determination of their color coordinates. The coloring of pigment occurs due to the selective absorption of certain wavelengths of light by its crystal lattice. As a result, the pigments are colored in a color complementary to the absorbed one. Most often, the color carriers in the pigments are the chromophores. These are atoms and atomic agglomerates which have the ability to impart one or another color to the substances in which they are present.

Table 2 shows the results obtained for color coordinates of the pigments synthesized, using the CIELab colour system. All pigments are blue, due to the cobalt ion. It can be seen from the data presented that the best results were obtained for Co-willemite pigment – k CoO.ZnO.SiO₂ synthesized at 1000°C- $b^* = -47.2$. Good results are also obtained for the same composition synthesized at 900°C, $b^* = -31.4$. After the introduction of additives such as FeO, NiO, P₂O₅ the blue color decreases, resp. parameter - b^* decreases, too. As the temperature of the synthesis increases, the amount of blue color increases (Table 2).

Table 2. Color measurement of pigments synthesized at 900°C and 1000°C

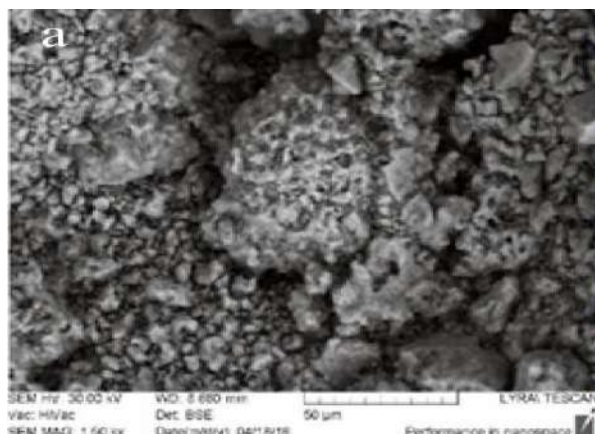
Pigment	Colour	L*	a*	b*
CoO.ZnO.SiO ₂ 1 - 900°C		28,7	2,1	-31,4
CoO.ZnO.SiO ₂ 1 - 1000°C		38,5	8,4	-47,2
CoO.ZnO.SiO ₂ .0,1FeO 2 - 900°C		23,5	-3,2	-7,2
CoO.ZnO.SiO ₂ .0,1FeO 2 - 1000°C		29,6	-0,1	-24,4
CoO.ZnO.SiO ₂ .0,1NiO 3 - 900°C		29,3	1,3	-22,6
CoO.ZnO.SiO ₂ .0,1NiO 3 - 1000°C		41,6	3,9	-37,5
CoO.ZnO.0,5SiO ₂ .0,5P ₂ O ₅ 4 - 900°C		53,8	12,6	-24,3
CoO.ZnO.0,5SiO ₂ .0,5P ₂ O ₅ 4 - 1000°C		62,3	10,5	-26,8

SEM analysis

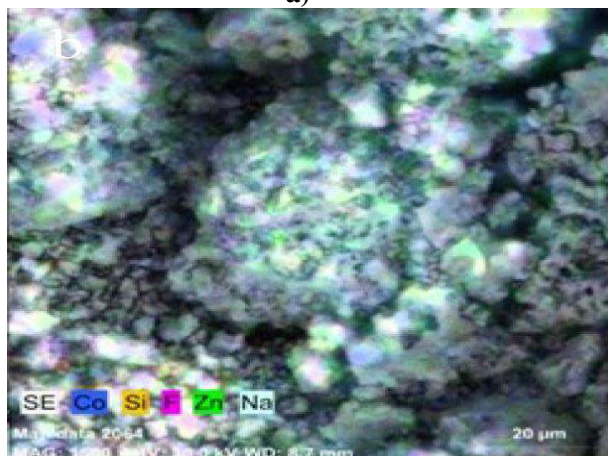
To determine the topography of the samples, scanning electron spectroscopy was applied. Scanning electron microscopy (SEM) is a method for direct study of the structure of the samples. Observations were combined with Energy

Distributed X-ray Spectroscopy conducted with a Bruker detector. Fig. 3 (a, b) show micrographs of willemite pigments.

The synthesized pigments were observed in reflected electron mode at low (1500 times) and high (3000 times) increases. SEM observations at low magnifications were combined with a mapping EPCP to monitor the distribution of the elements in crystalline phase (Fig. 3b)



a)



b)

Fig.3 (a, b) Micrographs of Co – willemite pigment synthesized at 1000°C

The figure shows that the particles are opaque to the electron beam. In this aspect from the pictures taken, conclusions can only be drawn about the shape and size of the crystals as well as their tendency to aggregation. The crystal sizes were from 3 to 5 µm. In most cases, however, the tendency for aggregation was quite strong and the material began melting under the electron beam.

CONCLUSIONS

Willemite ceramic pigments were synthesized via solid-state high temperature sintering.

The optimal parameters for the process of synthesis of all initial mixtures were established.

The starting materials used for the synthesis were CoO, ZnO, CoO, Fe₂O₃, NiO and SiO₂.H₂O.

In the synthesized pigments ZnO was substituted partially by CoO.

It was found out that the pigment with composition CoO.ZnO.SiO₂ synthesized at 1000°C had the most saturated color. At this composition the amount of blue color measured by the system CIELab was b* = -41.24.

The introduction of oxide additives, such as FeO, NiO, P₂O₅, led to decrease of the intensity of blue color: the parameter (-b *) had lower values.

It was established that the synthesized pigments could successfully be used in glazes for wall tiles.

ACKNOWLEDGEMENT

This work was supported by the Bulgarian Ministry of Education and Science under the National Research Fund, grant agreement KP-06-H27/14 – 2018.

REFERENCES

- Ozel, E. and H. Yurdakul, S. Turan, M. Ardit, G. Cruciani and M. Dondi. *J. Eur. Cer. Soc.*, 30, (2010), p. 3319-3329.
- Galindo, R., M. Llusar, A. Tena, G. Monros and J. Badenes. *J. Eur. Cer. Soc.*, 1, (2007), p. 199-205.
- Alarcon, J., P. Escribano and J. Gargallo. *Br. Ceram. Trans. J.*, 3, (1984), p. 81-83.
- Carda, J., G. Monros, P. Escribano and J. Alarcon. *J. Am. Cer. Soc.*, 1, (1989) p.160-162.
- Klemme, S., J. Miltenburg, P. Javorsky and F. Wastin. *Am. Miner.*, 90, (2005), p. 663-666.
- Dimtrov, Ts., I. Markovska and Ts. Ibrev. *Eur. Un. Sci. (EUS)*, 50, (2018) p. 55-58.
- Ibrev, Ts., I. Markovska and Ts. Dimitrov, *Annual of Assen Zlatarov University*, 2018, volume XLVII, book 1, p. 44- 49.
- Masslennikova., G., A. Glebicheva and N. Fomina. *Glass and Ceram.*, 8, (1974), p. 23-25.
- K. Kvjatkovskaj and A. Zazigin. *Glass and Ceram.*, 2 (1986) 14-18.

MONITORING THE DYNAMICS OF SOLUBLE PHOSPHATES DURING ANAEROBIC DIGESTION OF BUFFALO MANURE

Maya Stancheva, Hiusein Yemendzhiev, Valentin Nenov

E-mail: maya.stan4eva@gmail.com

ABSTRACT

The application of anaerobic digestion of livestock manure is a useful technology for reducing organic waste matter and simultaneously gaining energy in the form of biogas. Consumer economy encourages the consumption of a large amount of dairy and meat products and, as a result, livestock farms increase their capacities and their waste. On the other hand, this kind of waste incorporates a considerable amount of phosphorus. Phosphorus is a biogenic element needed by all living organisms and it is a non-renewable resource mined from phosphate rocks. Our experimental work comprised a process of anaerobic digestion batch of buffalo manure for 42 days in which the quantity of phosphates in soluble form as well as other required parameters were monitored.

Key words: *phosphorus, soluble phosphates, anaerobic digestion, buffalo manure*

INTRODUCTION

Anaerobic digestion (AD) is a commonly used technology that generates biogas and breaks down organic materials by anaerobic microbes. The processes of AD are used in the treatment of organic wastes, such as livestock manure, municipal waste, food and fruit/vegetable processing waste, etc.

The advantages of AD technologies are: substantial odour reduction; reduction of greenhouse gas (GHG) emissions; potential pathogen reduction; minimization of solid waste for disposal; production of a renewable energy source (biogas) and enhanced nutrient management [1].

Since the animal industry is growing to meet the increasing consumption of more livestock products as a result of the population growth, changes in life habits and higher living standards [2], animal wastes need more appropriate treatment because of the quantity and quality of their resources.

AD effluent contains a high level of phosphorus (P) that, when directly discharged, has a potential to cause various environmental issues, for instance eutrophication, which affects aquatic biological systems. On the contrary, phosphorus is a principal nutrient of concern to all living organisms, it plays a vital role in plant and animal physiology and growth. It takes part in plant photosynthesis. It is incorporated in the Adenosine Tri-Phosphate (ATP) molecule that acts as an energy carrier for cells. In natural ecosystems, phosphorus is present in low concentrations in

soils and, for the most part, found in the form of compounds that are not available for plant uptake. Due to its scarcity, ecosystems have evolved to be very effective in the use of phosphorus. Also, phosphorus is applied in many industries. In 2005, total external inputs to EU cropland and livestock amounted to 1.8 Mt P, comprising 1.4 Mt of mineral fertiliser P and 0.4 Mt P in feed imports [4]. The reason why special attention is paid to this element is that phosphorus is considered a non-renewable resource on the human time scale because the rock takes about 10 to 15 million years to form. Having in mind the demand for phosphorus, it is expected that there will be a phosphorus deficiency [3]. In the last decade, phosphorus recovery has been the subject of intense research. With current technology and incentives for implementing the circular economy, the most promising three categories of substrate to work on are: sewage waste and food chain waste especially slaughterhouse waste. The potential volume of recovery of these substrates are estimated to be ca. 2.5 Mt P annually [5].

P recovery from AD residues in the form of struvite ($MgNH_4PO_4 \cdot 6H_2O$), a high-quality fertilizer, has been numerously proved as an applicable technique in the literature [6-12]. Most of the studies in the literature support the removal/recovery of the readily available nutrients in the digestion [13-15]. However, the dissolution of phosphorus from the solid phase is critical for the recovery of phosphorus.

There is no doubt that pH is one of the most important factors affecting P release [16], because sorption–adsorption, precipitation–solubilisation and other chemical reactions related to P speciation transformation are greatly pH dependent.

One way to extract phosphorus from organic matter is by acidification of the effluent and separation of the fluid from solid phase [17].

Also, sludge fermentation, during which P release is observed resulting from the degradation of intracellular polyphosphate from polyphosphate-accumulating organisms (PAOs), is greatly affected by pH [18]. In order to recycle P resources as much as possible, it becomes very important to release P from manure.

To optimise the crystallization of struvite conditions such as high pH of the fluid (up to pH 9), an environment relatively clean from organic matter, addition of seed material, etc are needed.

The aim of this study is the monitoring of the concentration of soluble form of phosphates during an AD of buffalo manure and assessment of the potential of digested effluent for crystallization of struvite.

EXPERIMENT

The experiment was performed in a lab-scale glass anaerobic reactor with working volume of 1200 ml (Fig. 1). The reactor was joined to a hot plate and a thermal probe to maintenance temperature of 35°C (mesophilic condition), and a propeller agitator. The biogas produced ran through an outlet pipe into a measuring cylinder, where it was quantified.

One batch with substrate provided by the Murra - 2002 OOD buffalo farm in Straldzha was used. Manure samples were collected by floor scrapings of the buffalo stables. The inoculum volume was 10%. It came from the storage tank in the farm and it was free from rough livestock waste such as straw and had a total solid content of 4.4%. The substrate consisted of fresh buffalo manure, blended in a mixer and diluted with tap water to 4.4% total solids.

Sampling was done every two days and the samples were tested in replicate for:

- 1) *pH*: potentiometric measurement
- 2) *Dissolved phosphates (PO₄)*: according to ISO 6878:2004
- 3) *Dissolved ammonium ions (NH₄)*: spectrophotometric determination by Nessler.

The samples were centrifuged at 3000 rpm for 5 min to separate the solids, and the supernatant was used for chemical analysis.

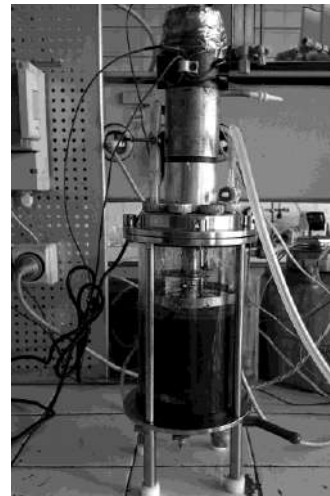


Fig. 1. Lab-scale anaerobic digestion reactor

For the purposes of the experiment the values of the following parameters were analysed at the beginning and the end of the process:

- 4) *Total solids (TS)*: oven drying at 105°C until constant weight.
- 5) *Volatile solids (VS)*: drying in laboratory muffle furnace at 600°C until constant weight. VS represent the difference between TS and fixed solids (FS).
- 6) *Inorganic solids (IOS)*: they are equal to FS after drying at 600°C.
- 7) *Chemical oxygen demand (COD)*: centrifugation and analysis of the supernatant according to cuvette test (Hach) – LCK 514
- 8) *Total nitrogen (TN)*: N-reduction and Kjeldahl analysis. The N-content is quantified titrimetrically.
- 9) *Total phosphorus (TP)*: acid digestion with concentrated sulphur acid and successive analysis of phosphates according to ISO 6878:2004.
- 10) *Coliforms: Most probable number (MPN)* according to EPA Method 1681: Faecal Coliforms in Sewage Sludge (Biosolids) by Multiple-Tube Fermentation using A-1 medium (2006).

RESULTS AND DISCUSSION

Table 1 shows the characteristics of the substrate before and after anaerobic digestion. With the AD process the amounts of *TS*, *VS* and *COD* were decreased by 29%, 27% and 37%, respectively.

Table 1. Substrate characteristics before and after anaerobic digestion

Parameter	Before AD	After AD
<i>TS</i> , %	4.40±0.05	3.11±0.02
<i>VS</i> , %	3.34±0.01	2.43±0.06
<i>IOS</i> , %	1.05±0.04	0.69±0.04
<i>pH</i>	7.70±0.32	7.54±0
<i>COD</i> , mgO ₂ l ⁻¹	14,150±70.71	8,975±106.07
<i>TN</i> , %	0.12±0.002	0.07±0.01
<i>TP</i> , %	0.036±0.002	0.038±0.001
<i>C : N : P</i>	51.67 : 3.39 : 1	35.98 : 1.75 : 1

Coliform bacteria, indicator organisms of microbiological contamination, were reduced to 5.22 MPNg⁻¹ in log with a 95% confidence interval [4.22, 5.65], as the initial value was 7.32 MPNg⁻¹ in log with a 95% confidence interval [6.78, 7.70].

The monitoring of soluble phosphates during the AD process showed an initial rise of the PO₄ until the sixth day of the experiment (Fig. 2) and a subsequent decrease to values close to the original ones. A study about the effect of AD on manure characteristics for phosphorus precipitation from swine waste resulted in 26% available reactive phosphorus increase [17].

Also, it is noticeable that the pH value at the beginning of the process varied between 6.7 and 6.9 (Fig. 3), and on the eleventh day of the experiment the pH value had a stable position between 7.40 and 7.54. This could be explained by the high development rate of volatile fatty acids due to the degradation of organic matter. The higher pH shows that the volatile fatty acids were utilized due the methanization process and caused the increase of alkalinity.

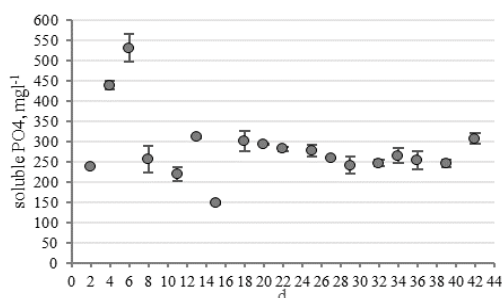


Fig. 2. Monitoring of soluble phosphate

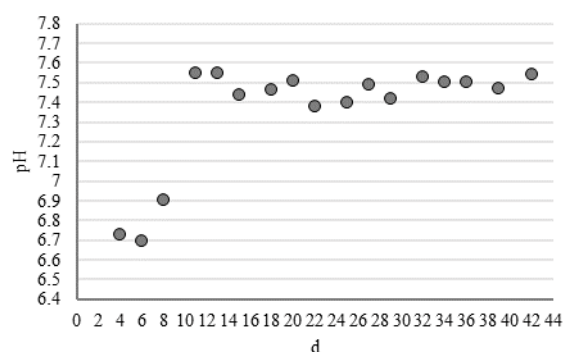


Fig. 3. Monitoring of pH

The ammonium ions concentration during AD has a stable state, as shown in Figure 4. Our experience in other AD experiments with livestock manure from cattle had analogous results.

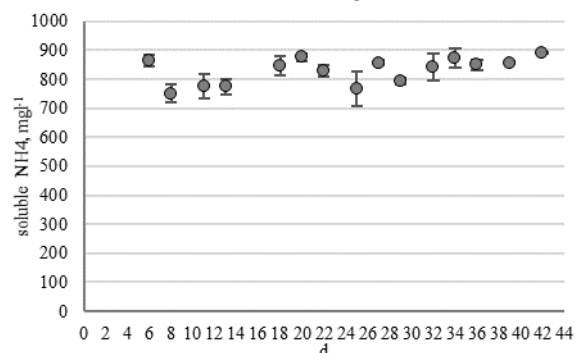


Fig. 4. Monitoring of ammonium ions

CONCLUSION

During the AD process the monitoring of soluble phosphates shows an initial rise of PO₄ until the sixth day of the experiment and a subsequent decrease to values close to the original ones. However, the soluble phosphates concentration is reasonably high for undertaking successive treatment steps of microfiltration and crystallization of struvite by addition of a magnesium source and increase of pH.

ACKNOWLEDGEMENTS

This work was supported by Project BG05M2OP001-1.002-0019: Clean technologies for sustainable environment –water, waste, energy for circular economy (Clean&Circle) for the development of a Centre of Competence.

This work was also supported by the Bulgarian Ministry of Education and Science – National Science Fund under project DN17/14.

REFERENCES

1. Lin, H., J. Gan, A. Rajendran, C. E. R. Reis and B. Hu, Phosphorus Removal and Recovery from Digestate after Biogas Production, *In: Biofuels - status and perspectives*, (2015), pp 517–546.
2. He, Z. and H. Zhang, *Applied Manure and Nutrient Chemistry for Sustainable Agriculture and Environment*, (2014): Springer.
3. Daneshgar, S., A. Callegari, A. G. Capodaglio and D. Vaccari, The Potential Phosphorus Crisis: Resource Conservation and Possible Escape Technologies: A Review, *Resources*, (2018), 7, 37; doi:10.3390/resources7020037.
4. van Dijk, K.C., J.P. Lesschen, O. Oenema, Phosphorus flows and balances of the European Union Member States. *Science of The Total Environment* 542, (2016), 1078–1093.
5. Buckwell, A. and E. Nadeu, *Nutrient Recovery and Reuse (NRR) in European agriculture. A review of the issues, opportunities, and actions*, (2016), The RISE Foundation.
6. Schuiling, R.D. and A Andrade, Recovery of struvite from calf manure. *Environ. Technol.*, (1999), 20(7), 765.
7. Doyle, J.D. and S.A. Parsons, Struvite formation, control and recovery. *Water Res.*, (2002), 36(16), 3925.
8. Burns, R.T., L.B. Moody, I. Celen, J. R. Buchanan, Optimization of phosphorus precipitation from swine manure slurries to enhance recovery. *Wat. Sci. Tech.*, (2003), 48 (1). 139.
9. Uludag-Demirer, S.; M. Othman, Removal of ammonium and phosphate from the supernatant of anaerobically digested waste activated sludge by chemical precipitation. *Bioresour. Technol.*, (2009), 100, 3236.
10. Uludag-Demirer, S. A., Study on nutrient removal from municipal wastewater by struvite formation using Taguchi's design of experiments. *Environ. Eng. Sci.*, (2008), 21,1.
11. Uludag-Demirer, S., G.N. Demirer, S. Chen, Ammonia removal from anaerobically digested dairy manure by struvite precipitation. *Process Biochem.*, (2005), 40, 3667.
12. Yetilmezsoy, K., Z. Sapci-Zengin, Recovery of ammonium nitrogen from the effluent of UASB treating poultry manure wastewater by MAP precipitation as a slow release fertilizer. *J. Hazard. Mater.*, (2009), 167(1), 260.
13. Uludag-Demirer, S., M. Othman, Removal of ammonium and phosphate from the supernatant of anaerobically digested waste activated sludge by chemical precipitation. *Bioresour. Technol.*, (2009), 100, 3236.
14. Guney, K.; A. Weideler, J. Krampe, Phosphorus recovery from digested sewage sludge as MAP by the help of metal ion separation. *Water Res.*, (2008), 42, 4692.
15. Szogi, A.A.; M.B. Vanotti, P.G. Hunt, Phosphorus recovery from poultry litter, *Transactions of ASABE*, (2008), 51,1727.
16. Qian, T., X. Zhang, J. Hu, H. Jiang, Effects of environmental conditions on the release of phosphorus from biochar/ *Chemosphere* 93, (2013), 2069–2075.
17. Dimitrova, J., V. Nenov, H. Yemendzhiev, G. Peeva, R. Koleva, F. Zerrouq, Developments in nutrient removal and recovery. *Journal of Chemical Technology and Metallurgy*, (2018), 53, 5, 816-824.
18. Chen, Y.G., S. Jiang, H.Y. Yuan, Q. Zhou, G.W. Gu, Hydrolysis and acidification of waste activated sludge at different pHs, *Water Res.* 41 (2007) 683–689.
19. Moody, L. B., R. T. Burns, K. J. Stalder, Effect of anaerobic digestion on manure characteristics for phosphorus precipitation from swine waste. *Applied Engineering in Agriculture*, (2009), Vol. 25(1): 97- 102 American Society of Agricultural and Biological Engineers ISSN 0883-8542.

INVESTIGATION OF THE BIOACTIVITY SCORE OF THIRD GENERATION RETINOIDS

Yana Koleva

E-mail: yanuriana@abv.bg

ABSTRACT

Retinoids comprise a family of polyisoprenoid lipids that include vitamin A and its various natural and synthetic analogues. Due to the existence of different types of retinoid receptors, response elements and cofactors, retinoid physiology is mediated by multiple discrete pathways and is highly complex. The aim of this work is to calculate the probable molecular physicochemical properties and bioactivity score of third generation retinoids with Molinspiration software. The data analysis revealed that some third generation retinoids have various molecular properties and structural features and their bioactivity score is active and moderately active.

Key words: *third generation retinoids, predict, bioactivity score, molecular properties*

INTRODUCTION

Retinoids include both naturally occurring molecules and synthetic compounds that have specific biologic activities that resemble those of vitamin A. Vitamin A or retinol is a fat soluble vitamin. Its esterified form, vitamin A palmitate, is supplied in the diet by animal sources such as fish oil, eggs, butter, fortified margarine and animal liver. Vitamin A is also derived from carotenoid pigments, particularly β -carotene, which is found in many green and yellow vegetables [1].

Third Generation: These are poly-aromatic retinoids called arotinoids, which include adapalene, bexarotene, tazarotene, temarotene, mofarotene [2].

The discovery of retinoic acid receptors in the 1980s allowed research directed towards receptor specific, third generation retinoids with a safer therapeutic index and a more selective action. In the 1990s, researchers began devising molecules that would have greater conformational rigidity. As a result, adapalene, a derivative of naphthoic acid having comedolytic, antiproliferative and anti-inflammatory properties [3], was found. It has a similar efficacy to tretinoin but unlike tretinoin, is stable in sunlight and tends to be less irritating. Bexarotene belongs to a subclass of arotinoids called rexinoids, because they bind to the retinoid X receptors which are responsible for controlling cell division. It is a drug of choice in CTCL (cutaneous T-cell lymphoma) [2].

Tazarotene is a novel, acetylenic retinoid, and is the first topical retinoid developed for the treatment of psoriasis. It targets keratinocyte and modulates the major causes of psoriasis. It is rap-

idly metabolized to an active free acid form tazarotenic acid, which is rapidly eliminated in animal species. Tazarotene selectively transactivates RAR β and RAR γ subtypes which are the predominant receptors in epidermis and is inactive at retinoid X receptors (RXRs). It has low systemic absorption after topical administration. Topical doses are neither teratogenic nor carcinogenic and are not sensitizing or photosensitizing. The RAR nuclear receptor is the predominant receptor in the epidermis for which tazarotenic acid has high affinity. Temarotene and mofarotene are newer arotinoids awaiting FDA approval. Temarotene shows no sign of hypervitaminosis A and is not teratogenic presumably due to its lack of a polar group. This can be used clinically in the treatment of proliferative dermatological diseases. Mofarotene can be used as an antineoplastic agent in lymphomas and breast cancer [2].

The aim of this work is to calculate the probable molecular physicochemical properties and bioactivity score of third generation retinoids with Molinspiration software. The data analysis revealed that some third generation retinoids have various molecular properties and structural features and their bioactivity score is active and moderately active.

MATERIAL AND METHODS

Compound Data. Five compounds of third generation retinoids are presented in Table 1 [4].

Molinspiration. Molinspiration supports the internet chemistry community for calculation of important molecular properties (logP, polar sur-

face area, number of hydrogen bond donors and acceptors and others), as well as prediction of bioactivity score for the most important drug targets (GPCR ligands, kinase inhibitors, ion channel modulators, nuclear receptors) [5].

LogP (octanol/water partition coefficient). LogP is calculated by the methodology developed by Molinspiration as a sum of fragment-based contributions and correction factors. The method is very robust and is able to process practically all organic and most organometallic molecules.

Molecular Polar Surface Area TPSA. Molecular Polar Surface Area is calculated based on the methodology published by Ertl et al. [6] as a sum of fragment contributions. O- and N- centered polar fragments are considered. PSA has been shown to be a very good descriptor characterizing drug absorption, including intestinal absorption, bioavailability, Caco-2 permeability, and blood-brain barrier penetration.

Molecular Volume. The method for calculation of molecule volume developed at Molinspiration is based on group contributions. These have been obtained by the fitting sum of fragment contributions to "real" 3D volume for a training set of about twelve thousand, mostly drug-like molecules. 3D molecular geometries for a training set were fully optimized by the semiempirical AM1 method.

"Rule of 5" Properties is a set of simple molecular descriptors used by Lipinski in formulating his "Rule of 5" [7]. The rule states that most "drug-like" molecules have $\log P \leq 5$, molecular weight ≤ 500 , number of hydrogen bond acceptors ≤ 10 , and number of hydrogen bond donors ≤ 5 . Molecules violating more than one of these

rules may have problems with bioavailability. The rule is called "Rule of 5" because the border values are 5, 500, 2×5 , and 5.

The number of Rotatable Bonds – *nrotb*. This simple topological parameter is a measure of molecular flexibility. It has been shown to be a very good descriptor of oral bioavailability of drugs [8]. Rotatable bond is defined as any single non-ring bond, bounded to nonterminal heavy (i.e., non-hydrogen) atom. Amide C-N bonds are not considered because of their high rotational energy barrier.

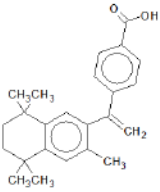
Bioactivity score. Bioactivity of the drug can be checked by calculating the activity score of GPCR ligand, ion channel modulator, nuclear receptor legend, kinase inhibitor, protease inhibitor, and enzyme inhibitor. The drug likeness score of each compound was calculated and compared with the specific activity of each compound, and the results were compared with a standard drug. For organic molecules the probability is: if the bioactivity scores (>0), then it is active, if ($-5.0-0.0$) then moderately active, if (<-5.0) then inactive [5].

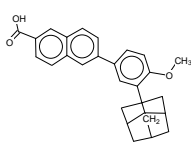
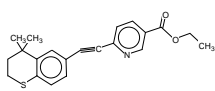
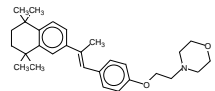
RESULTS AND DISCUSSION

The Molinspiration software has been used for identification of probable parameters: molecular physicochemical properties (Table 1) and bioactivity score (Table 2) of five compounds of third generation retinoids.

The data from the calculation of molecular physicochemical properties of the five retinoid compounds of third generation are presented in Table 1.

Table 1. Calculated data for molecular physicochemical properties of third generation retinoids.

Third generation retinoids	A ₁	A ₂	A ₃	A ₄	A ₅	A ₆	A ₇	A ₈	A ₉
Bexarotene 	6.81	37.30	26	348.49	2	1	1	3	348.76
Adapalene	7.69	46.53	31	412.53	3	1	1	4	387.26

										
Tazarotene										
	4.05	39.20	25	351.47	3	0	0	3	325.29	
Temarotene										
	6.94	21.71	32	433.64	3	0	1	6	442.17	
Mofarotene										

*The following properties are available:

A₁: LogP - octanol-water partition coefficient; **A₂**: PSA - polar surface area; **A₃**: natoms - number of nonhydrogen atoms; **A₄**: MW - molecular weight; **A₅**: nON - number of hydrogen-bond acceptors (O and N atoms); **A₆**: Nohnh - number of hydrogen-bond donors (OH and NH groups); **A₇**: nviolations - number of Rule of 5 violations; **A₈**: nrotb - number of rotatable bonds; **A₉**: volume - molecular volume

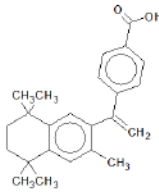
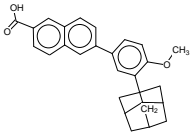
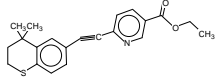
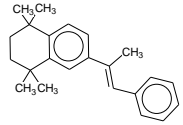
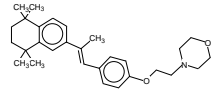
The data analysis in Table 1 shows that:

a) the five retinoid compounds have one value (Tazarotene) less and four values larger (Bexarotene, Adapalene, Temarotene and Mofarotene) than five (log P has to be ≤ 5); b) Molecular weight has to be ≤ 500 ; for the retinoid tested are less than 500; c) The parameter Polar Surface Area is from 0 to 46.53 for the five retinoid compounds, d) Number of hydrogen bond acceptors has to be ≤ 10 and has to be number of hydrogen bond donors ≤ 5 ; It is within limits for the retinoid compounds; e) Number of Rule of 5

violations – the values of compounds are between 0 and 1; f) The topological parameter (number of rotatable bonds) is a measure of molecular flexibility. The value of the retinoid compounds is between two and six; g) Molecular volume. The values of the molecular volume of the five retinoid compounds are from 321.44 to 442.17.

Calculated data of bioactivity score of retinoid compounds are present in Table 2.

Table 2. Calculated data for bioactivity score of the five retinoid compounds

Third generation retinoids	A ₁	A ₂	A ₃	A ₄	A ₅	A ₆
Bexarotene 	0.47	0.14	0.01	0.92	0.02	0.39
Adapalene 	0.11	-0.03	-0.04	0.39	0.04	0.17
Tazarotene 	0.21	-0.07	0.02	0.60	0.06	0.37
Temarotene 	0.25	0.17	0.06	0.75	-0.12	0.28
Mofarotene 	0.21	0.07	0.10	0.59	-0.06	0.17

*The following properties are available:

A₁: GPCR ligand; **A₂**: Ion channel modulator; **A₃**: Kinase inhibitor; **A₄**: Nuclear receptor ligand; **A₅**: Protease inhibitor; **A₆**: Enzyme inhibitor;

The data show that for all calculated bioactivity scores of bexarotene it is active because bio-

activity values are greater than 0 and therefore bexarotene is active. The Adapalene is active for

the following bioactivity score (GPCR ligand, Nuclear receptor ligand, Protease inhibitor and Enzyme inhibitor) and is moderately active for Ion channel modulator and Kinase inhibitor. The Tazarotene is active for the following bioactivity score (GPCR ligand, Kinase inhibitor, Nuclear receptor ligand, Protease inhibitor and Enzyme inhibitor) and is moderately active for Ion channel modulator. Both Temarotene and Mofarotene are active for the following bioactivity score (GPCR ligand, Ion channel modulator, Kinase inhibitor, Nuclear receptor ligand and Enzyme inhibitor) and is moderately active for Protease inhibitor.

The diversity of possible drug targets (of which each requires a different combination of matching molecular characteristics) is so enormous that it is impossible to find a common denominator for all of them and to express molecule drug-likeness by a single "magic number". Simple count criteria (like limits for molecular weight, log P, or a number of hydrogen bond donors or acceptors) have also a relatively limited applicability and are useful only to discard obvious non-drugs [5].

CONCLUSIONS

The five retinoid compounds of third generation may be defined as a complex balance of various molecular properties and structural features.

Their bioactivity score is active and moderately active.

ACKNOWLEDGEMENTS

This study was financially supported by the Burgas University through the Scientific Research Sector, Project number 434/2019.

REFERENCES

1. Orten, J.M., O.W. Neuhaus. *Human Biochemistry*, 10th ed. Mosby, St Louis, 1982, p. 735-746.
2. Archana, J., et al., *J. Pharm. Sci. & Res.*, 2, 2010, p. 376-383.
3. Bikowski, J.B., *Drugs Dermatol.*, 4, 2005, p. 41-47.
4. <https://chem.nlm.nih.gov/chemidplus/>
5. <https://www.molinspiration.com/>
6. Ertl, P., B. Rohde, P. Selzer, *J. Med. Chem.*, 43, 2000, p. 3714-3717.
7. Lipinski, C.A., F. Lombardo, B.W. Dominy, P.J. Feeney. *Adv. Drug Delivery Rev.*, 23, 1997, p. 4-25.
8. Veber, D.F., S.R. Johnson, H.-Y. Cheng, B.R. Smith, K.W. Ward, K. D. Kopple. *J. Med. Chem.*, 45, 2002, p. 2615-2623.

MOLECULAR PROPERTIES AND BIOACTIVITY SCORE OF CYCLODODEC-2-EN-1-YL ETHERS

Yana Koleva, Asen Kolev*
E-mail: yanuriana@abv.bg

ABSTRACT

Cyclododec-2-en-1-yl ethers are derived by the catalytic substitution reaction between isomeric cyclododec-2-en-1-yl acetates and primary aliphatic alcohols in the presence of Pd⁰[PPh₃]₄. Newly synthesized chemicals such as the cyclododec-2-en-1-yl ethers need to be explored for molecular properties and bioactivity score to be introduced in the environment and living organisms. The aim of this work is to calculate the probable molecular physicochemical properties and bioactivity score of cyclododec-2-en-1-yl ethers with Molinspiration software. The data analysis revealed that the newly synthesized cyclododec-2-en-1-yl ethers have good performance for molecular properties and bioactivity score is active for the Ion channel modulator and Enzyme inhibitor and moderately active for GPCR ligand, Kinase inhibitor, Nuclear receptor ligand and Protease inhibitor.

Key words: cyclododec-2-en-1-yl ethers, predict, bioactivity score, molecular properties

INTRODUCTION

Scientific and regulatory activity in environmental (ecological) risk assessment continues to progress globally. In Europe, the REACH programme, together with the new requirements for the ERA of human pharmaceuticals, represent significant developments in regulatory ERA procedures for the industry. The Organisation for Economic Co-operation and Development (OECD), for example, has been developing in vitro and in vivo mammalian and wildlife test guidelines for assessing the developmental and reproductive effects of chemicals in the environment [1, 2].

It is evident that ecological risk assessment (ERA) of synthetic organic compounds can provide a safeguard against pollution [3]. ERA includes three primary phases as defined by U.S. Environmental Protection Agency (US EPA): problem formulation, analysis, and risk characterization [4]. It is obvious that data on physicochemical properties, environmental behaviour and ecotoxicology of organic compounds, are indispensable for the ERA. However, the data have three aspects of problems: 1) Lack of the data [5]; 2) Large expense of testing [6]; 3) Uncertainty in data [7].

Among the numerous compounds used in the perfume industry nowadays, methoxy- and ethoxycyclododecanes as well as (2-methoxyethoxy)- and (2-ethoxyethoxy) cyclododecanes hold an important position. The commonly accepted procedures for the preparation of these compounds are multi-stage, and some of the reaction steps are associated with the formation of highly-toxic, explosive, or expensive chemicals. The cyclododec-2-en-1-yl ethers are derived by the catalytic substitution reaction between isomeric cyclododec-2-en-1-yl acetates [8] and primary aliphatic alcohols in the presence of Pd⁰[PPh₃]₄ [9]. Newly synthesized chemicals such as the cyclododec-2-en-1-yl ethers need to be explored for molecular properties and bioactivity score to be introduced in the environment and living organisms.

The aim of this work is to calculate the probable molecular physicochemical properties and bioactivity scores of cyclododec-2-en-1-yl ethers with Molinspiration software. The data analysis revealed that the newly synthesized cyclododec-2-en-1-yl ethers have good performance for molecular properties and bioactivity score is active for the Ion channel modulator and Enzyme inhibitor and moderately active for GPCR ligand, Kinase inhibitor, Nuclear receptor ligand and Protease inhibitor.

MATERIAL AND METHODS

Compound Data. Some newly synthesized chemicals (cyclododec-2-en-1-yl ethers) are presented in Table 1 [9].

Molinspiration. Molinspiration supports the internet chemistry community for calculation of important molecular properties (logP, polar surface area, number of hydrogen bond donors and acceptors and others), as well as prediction of bioactivity score for the most important drug targets (GPCR ligands, kinase inhibitors, ion channel modulators, nuclear receptors) [10].

LogP (octanol/water partition coefficient). LogP is calculated by the methodology developed by Molinspiration as a sum of fragment-based contributions and correction factors. The method is very robust and is able to process practically all organic and most organometallic molecules.

Molecular Polar Surface Area TPSA. Molecular Polar Surface Area is calculated based on the methodology published by Ertl et al. [11] as a sum of fragment contributions. O- and N- centered polar fragments are considered. PSA has been shown to be a very good descriptor characterizing drug absorption, including intestinal absorption, bioavailability, Caco-2 permeability, and blood-brain barrier penetration.

Molecular Volume. The method for calculation of molecule volume developed at Molinspiration is based on group contributions. These have been obtained by the fitting sum of fragment contributions to "real" 3D volume for a training set of about twelve thousand, mostly drug-like molecules. 3D molecular geometries for a training set were fully optimized by the semiempirical AM1 method.

"Rule of 5" Properties is a set of simple molecular descriptors used by Lipinski in formulating his "Rule of 5" [12]. The rule states that most "drug-like" molecules have logP \leq 5, molecular

weight \leq 500, number of hydrogen bond acceptors \leq 10, and number of hydrogen bond donors \leq 5. Molecules violating more than one of these rules may have problems with bioavailability. The rule is called "Rule of 5" because the border values are 5, 500, 2*5, and 5.

The number of Rotatable Bonds – nrotb. This simple topological parameter is a measure of molecular flexibility. It has been shown to be a very good descriptor of oral bioavailability of drugs [13]. Rotatable bond is defined as any single non-ring bond, bounded to nonterminal heavy (i.e., non-hydrogen) atom. Amide C-N bonds are not considered because of their high rotational energy barrier.

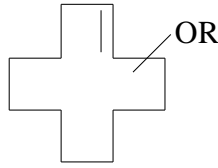
Bioactivity score. Bioactivity of the drug can be checked by calculating the activity score of GPCR ligand, ion channel modulator, nuclear receptor legend, kinase inhibitor, protease inhibitor, enzyme inhibitor. The drug likeness score of each compound was calculated and compared with the specific activity of each compound, and the results were compared with a standard drug. For organic molecules the probability is: if the bioactivity scores (>0), then it is active, if (-5.0-0.0) then moderately active, if (<-5.0) then inactive [10].

RESULTS AND DISCUSSIONS

In the present work, Molinspiration software has been used to identify some probable parameters, molecular physicochemical properties (Table 1) and bioactivity score (Table 2), of newly synthesized chemicals (cyclododec-2-en-1-yl ethers).

Data from the calculation of molecular physicochemical properties of newly synthesized cyclododec-2-en-1-yl ethers are presented in Table 1.

Table 1. Data from the calculation of molecular physicochemical properties of cyclododec-2-en-1-yl ethers.

Cyclododec-2-en-1-yl ethers 	A ₁	A ₂	A ₃	A ₄	A ₅	A ₆	A ₇	A ₈	A ₉
R= -CH ₃	4.98	9.23	14	196.33	1	0	0	1	222.80

R= -C₂H₅	5.36	9.23	15	210.36	1	0	1	2	239.60
R= -C₂H₄OCH₃	5.15	9.23	16	224.39	1	0	1	3	256.40
R= -C₂H₄OC₂H₅	5.53	9.23	17	238.41	1	0	1	4	273.20

*The following properties are available:

A₁: LogP - octanol-water partition coefficient; **A₂**: PSA - polar surface area; **A₃**: natoms - number of nonhydrogen atoms; **A₄**: MW - molecular weight; **A₅**: nON - number of hydrogen-bond acceptors (O and N atoms); **A₆**: Nohnh - number of hydrogen-bond donors (OH and NH groups); **A₇**: nviolations - number of Rule of 5 violations; **A₈**: nrotb - number of rotatable bonds; **A₉**: volume - molecular volume

The data analysis in Table 1 shows that:

a) newly synthesized cyclododec-2-en-1-yl ethers have one value less and three values larger than five (log P has to be ≤ 5); b) Molecular weight has to be ≤ 500 ; for cyclododec-2-en-1-yl ethers it is less than 500; c) The parameter Polar Surface Area is 9.23 for all newly synthesized cyclododec-2-en-1-yl ethers, d) Number of hydrogen bond acceptors has to be ≤ 10 and has to be number of hydrogen bond donors ≤ 5 ; It is within limits for cyclododec-2-en-1-yl ethers; e) Number of Rule of 5 violations – the values of

the cyclododec-2-en-1-yl ethers are between 0 and 1; f) The topological parameter (number of rotatable bonds) is a measure of molecular flexibility. The value of the cyclododec-2-en-1-yl ethers are between one and four; g) Molecular volume. The values of the molecular volume of the cyclododec-2-en-1-yl ethers are from 222.80 to 273.20.

Data from the calculation of bioactivity score of cyclododec-2-en-1-yl ethers are presented in Table 2.

Table 2. Calculation of bioactivity score of cyclododec-2-en-1-yl ethers

Cyclododec-2-en-1-yl ethers	A₁	A₂	A₃	A₄	A₅	A₆
R= -CH ₃	-0.21	0.13	-0.53	-0.41	-0.54	0.23
R= -C ₂ H ₅	-0.24	0.08	-0.58	-0.28	-0.54	0.16
R= -C ₂ H ₄ OCH ₃	-0.16	0.03	-0.40	-0.39	-0.34	0.06
R= -C ₂ H ₄ OC ₂ H ₅	-0.11	0.06	-0.37	-0.26	-0.25	0.09

*The following properties are available:

A₁: GPCR ligand; **A₂**: Ion channel modulator; **A₃**: Kinase inhibitor; **A₄**: Nuclear receptor ligand; **A₅**: Protease inhibitor; **A₆**: Enzyme inhibitor;

The newly synthesized organic chemicals (cyclododec-2-en-1-yl ethers) are active for the following bioactivity score (Ion channel modulator and Enzyme inhibitor) and are moderately active for GPCR ligand, Kinase inhibitor, Nuclear receptor ligand and Protease inhibitor.

The newly synthesized organic chemicals may be defined as a complex balance of various molecular properties and structural features. These properties, mainly hydrophobicity, electronic distribution, hydrogen bonding characteristics, molecule size, flexibility and presence of

specific structural features influence the behaviour of the molecule in a living organism, including bioavailability, transport properties, affinity to proteins, reactivity, toxicity, metabolic stability and many others.

CONCLUSION

Molecular physicochemical properties of newly synthesized cyclododec-2-en-1-yl ethers were selected and calculated for in silico prediction with Molinspiration software. The molecular properties showed that the molecules are active. The newly synthesized organic chemicals (cyclododec-2-en-1-yl ethers) are active for the following bioactivity score (Ion channel modulator and Enzyme inhibitor) and are moderately active for GPCR ligand, Kinase inhibitor, Nuclear receptor ligand and Protease inhibitor.

REFERENCES

1. Vos, J.G., E. Dybing, H. Greim, O. Ladefoged, C. Lambré, J.V. Tarazona, I. Brandt, A.D. Vethaak. *Crit. Rev. Toxicol.*, **30**, 2000, p. 71-133.
2. Gourmelon, A., J. Ahtiainen, *Ecotoxicol.*, **16**, 2007, p. 161-167.
3. Macleod, M., T.E. Mckone, K.L. Foster, R.L. Maddalena, T.F. Parkerton, D. Mackay. *Environ. Sci. Technol.*, **38**, 2004, p. 6225—6233.
4. U.S. Environmental Protection Agency. Guidelines for ecological risk assessment. In: Risk Assessment Forum. Washington: U.S. Environmental Protection Agency, **63**, 1998, p. 26846—26924.
5. Verhaar, H.J.M., J. Solbe, J. Speksnijder, C.J. Van Leeuwen, J.L.M. Hermens. *Chemosphere*, **40**, 2000, p. 875—883.
6. Enterprise & Industry Directorate General and Environment Directorate General. European Commission, REACH in brief. September, 2000. Available online at: <http://ecb.jrc.it/REACH/>
7. Linkov, I., M.R. Ames, E.A.C. Crouch, F.K. Satterstrom. *Environ. Sci. Technol.*, **39**, 2005, p. 6917—6922
8. Kolev, A., M. Skumov and E. Balbolov. *React. Kinet. Catal. L.*, **78**, 2003, p. 325-330.
9. Kolev, A., E. Balbolov, *Annual Assen Zlatarov-Burgas*, **XL**, 2011, p. 34-36.
10. <https://www.molinspiration.com/>
11. Ertl, P., B. Rohde, P. Selzer, *J. Med. Chem.*, **43**, 2000, p. 3714-3717.
12. Lipinski, C.A., F. Lombardo, B.W. Dominy, P.J. Feeney. *Adv. Drug Delivery Rev.*, **23**, 1997, p. 4-25.
13. Veber, D.F., S.R. Johnson, H.-Y. Cheng, B.R. Smith, K.W. Ward, K. D. Kopple. *J. Med. Chem.*, **45**, 2002, p. 2615-2623.

DESIGN OF AIR CATHODES FOR APPLICATION IN MICROBIAL FUEL CELL

Blagovesta Midyurova
E-mail: blagi77@abv.bg

ABSTRACT

The microbial fuel cell (MFC) with air cathode is a promising instrument for conversion of the chemical energy of organic matter into electrical energy. An important factor for the better performance efficiency of the cell is the design of the electrodes. Twelve air cathodes were manufactured containing different amounts of catalyst (Vulcan) and a different number of layers. Electrochemical screening of the different cathodes was carried out to determine their electrochemical potential. Better results were obtained with cathode Teflon: Vulcan – 5: 0.3g with 4 layers on its surface, where the currents measured were in the range from 2000 μ A to 3400 μ A. The application of this kind of air cathode has many advantages, such as high surface area and good transfer of oxygen.

Key words: microbial fuel cell, air cathodes, waste water

INTRODUCTION

Microbial fuel cells (MFC) with air cathode are a new and rapidly developing technology combining two ecologically important aspects – removal of organic and inorganic contaminants from waste flows and generation of energy [1, 2]. The application of these bioelectrochemical systems offers a number of advantages compared to the conventional methods for purification of water. This new approach has gained popularity in recent years with efforts devoted to improvement of the design of the reactors. This is achieved by various optimizations of the electrodes by expansion of their area and increase of their electrochemical activity. Teams of researchers work on the deposition of different types of catalysts, glues and conductive polymeric materials to activate the processes of oxygen transfer through the cathode [3].

Experiments of such kind were carried out by Tatinclaux et al. [4, 5], who studied the effect of cathodes with catalyst MnOx deposited onto a carbon cloth in MFC, with substrate of waste waters after the first precipitator. The researchers established for MFC with air cathode with MnOx that the increase of the ratio between electrode surface and reactor volume could help determine the capacity and efficiency of the MFC by the removal of substantial quantities of organic matter.

A schematic diagram of a microbial fuel cell with air cathode is shown in Fig. 1.

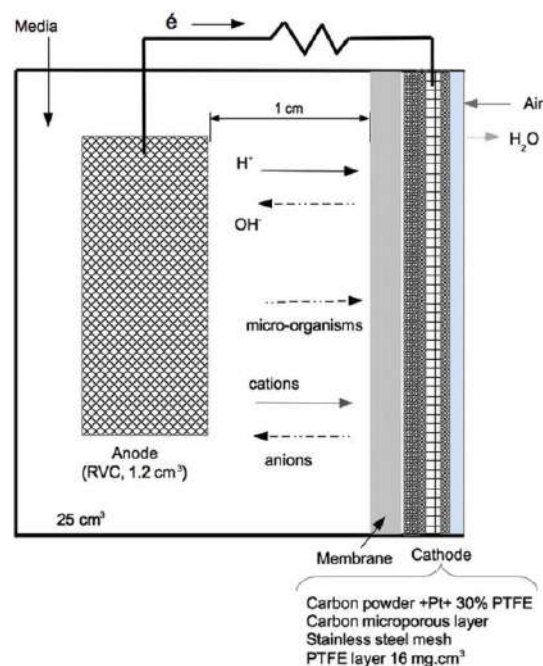


Fig. 1. Microbial fuel cell with air cathode [1]

A more detailed study of this matter can be found in [7-12], who reported different modifications of cathodes with Vulcan and different alternatives of the air cathode. Each modification and new cathode design improve the performance and the efficiency of the bioelectrochemical systems.

More profound and thorough research is necessary regarding the electrochemical potential of the cathode and the creation of new cathodes with possible biotechnological application.

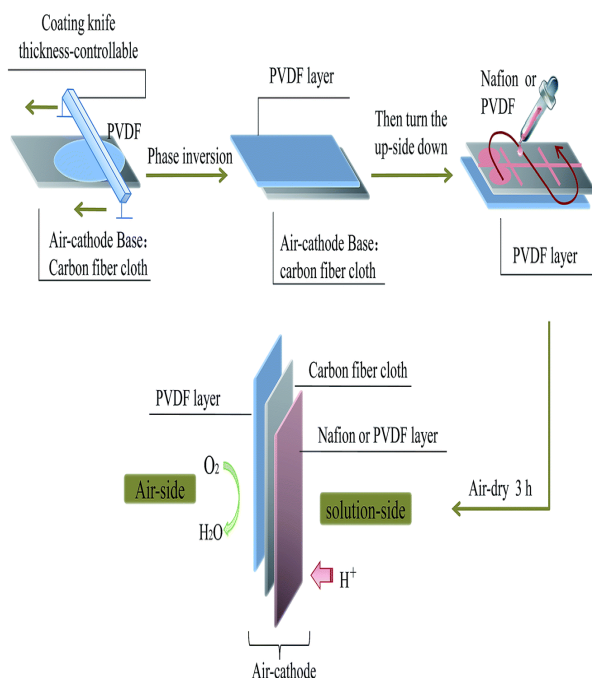


Fig. 2. Design of an air cathode [3]

The deposition of several layers of catalyzing materials is made to increase the specific area and improve the diffusion through the cathode.

The aim of the present work is to study the electrochemical potential of different air cathodes tested by cyclic voltammetry and use selected cathodes in future experiments with MFC on the basis of the results obtained.

PRESENTATION

For the present scientific research, 12 types of air cathodes were manufactured. Based on our previous experiments with metal matrix (stainless steel mesh with opening size $0.42 \mu\text{m}$), different kinds of catalysts in combination with Teflon (60% aqueous emulsion) were deposited on it. The ratio of polymer to additive was 5:0.1g; 5:0.2g; and 5:0.3g for better polymer adhesion to the metal matrix. The cathode was dried at room temperature for 24 h, after which the electrochemical analyses were carried out.

The cathodes developed with catalyst Vulcan and different number of layers had the following compositions:

1. Teflon:Vulcan – 5:0.1g – 1 layer
2. Teflon:Vulcan – 5:0.1g – 2 layers
3. Teflon:Vulcan – 5:0.1g – 3 layers
4. Teflon:Vulcan – 5:0.1g – 4 layers
5. Teflon:Vulcan – 5:0.2g – 1 layer
6. Teflon:Vulcan – 5:0.2g – 2 layers
7. Teflon:Vulcan – 5:0.2g – 3 layers

8. Teflon:Vulcan – 5:0.2g – 4 layers
9. Teflon:Vulcan – 5:0.3g – 1 layer
10. Teflon:Vulcan – 5:0.3g – 2 layers
11. Teflon:Vulcan – 5:0.3g – 3 layers
12. Teflon:Vulcan – 5:0.3g – 4 layers

The electrochemical methods show the behaviour of the electric charges in the vicinity of the boundary surface between two chemical phases. In this case, one phase was electrolyte – 250 mM aqueous solution of NaCl, where the charge transfer occurs through motion of ions. The other phase was an electrode, which was the phase through which the charge was transported by the motion of electrons. The electrochemical reactions of the modified air cathodes were observed by cyclic voltammetry (Fig. 3).

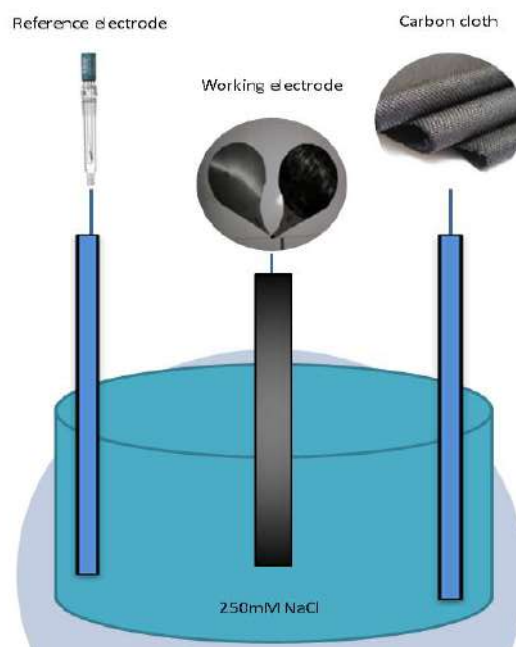


Fig. 3. Electrochemical test cell

The cyclic voltammetry curves of all the modified air cathodes were registered at intervals of 0.00244 and scanning speed 0.1 Vs^{-1} at room temperature ($25 \pm 2^\circ\text{C}$) in 250 mM solution of NaCl. The working electrode in this case was the air electrode the half-reaction of which was studied. The reference electrode was the one on the other side of the cell composed of phases with constant compositions and standard constant parameters. Carbon cloth was used aiming to approximate the conditions of the real system for which the cathodes were designed – a microbial fuel cell. The reference electrode in its three-component configuration was the saturated cal-

omel electrode – silver-silver chloride electrode: Ag/AgCl/KCl (saturated aqueous solution) with potential of 0.222V.

A test electrochemical cell was produced for the experiments (Fig. 3).

The voltammograms obtained consisted of two curves, the first of which corresponds to the increase of the potential. The increase of the potential was accompanied by decrease of the surface concentration and reaching maximal speed of the mass transfer which decreased later due to the effect of exhaustion (because of the slow diffusion). As a result, the current reached a maximum and then started to decrease. After reaching the maximal value of the current, the potential was scanned in the opposite direction, as this is indicated in the second part of the voltammogram (Fig. 4).

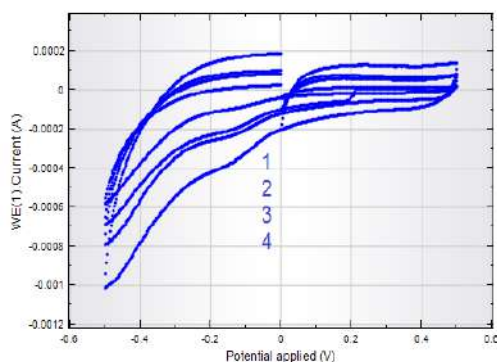


Fig. 4. Voltammograms of cathodes 1 - 4

Fig.4 shows the voltammograms of cathodes 1-4 containing Teflon:Vulcan – 5: 0.1 g with 4 layers deposited on its surface. Values of $600\mu\text{A}$ for the first cathode and $1000\mu\text{A}$ for the fourth one were observed, which resulted from the increased amount of Vulcan catalyst formed by the deposition of 4 layers.

Similar results were observed for cathodes 5-8 (Fig. 5) containing Teflon:Vulcan – 5: 0.2g and 4 layers deposited on their surfaces. The registered current values were from $700\mu\text{A}$ to $2000\mu\text{A}$.

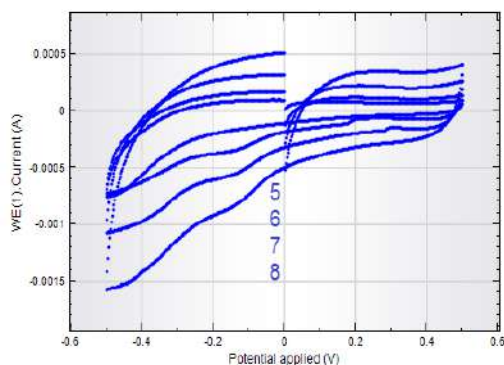


Fig. 5. Voltammograms of cathodes 5-8

Fig. 6 shows the voltammograms of cathodes 9-12 containing Teflon:Vulcan – 5: 0.3g with 4 layers deposited on their surfaces. The current values were in the range from $2000\mu\text{A}$ to $3400\mu\text{A}$.

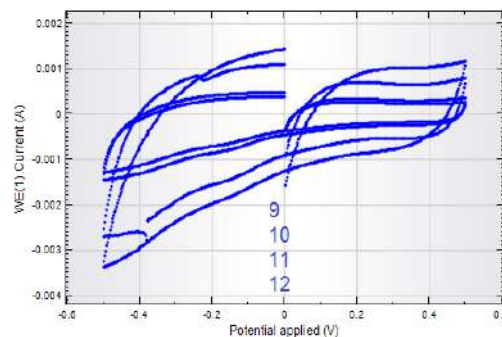


Fig. 6. Voltammograms of cathodes 9-12

Based on the electrochemical analysis, better results were obtained for the air cathodes containing catalyst Vulcan in ratio Teflon:Vulcan – 5: 0.3g with 4 layers deposited on the surface. These results are of preliminary nature and help for fast selection of cathodes possessing electro-active potential.

CONCLUSION

The creation of suitable design for the air cathodes to be applied in MFC is a serious challenge for the researchers working in the field of ecology and water purification.

It can be finally concluded that the cathode Teflon:Vulcan – 5: 0.3g with 4 layers deposited on its surface had better electrochemical stability compared to the other modified air cathodes.

In this respect, the results obtained from the present study are of certain originality and a highly efficient cathode for future application in MFC can be selected on their basis.

ACKNOWLEDGMENT

This work was supported by the Bulgarian Ministry of Education and Science under the National Research Programme “Young scientists and postdoctoral students”, approved by DCM # 577 / 17.08.2018.

REFERENCES

1. Kircheva N., J. Outin, G. Perriera, J. Ramousse et al., Bio-electrochemical characterization of air-cathode microbial fuel cells with mi-

- porous polyethylene/silica membrane as separator, *Bioelectrochemistry*, 106, 115-124, 2015.
2. Mohan S. V., Velvizhi G., Modestra J. A., Srikanth S., Microbial fuel cell: critical factors regulating bio-catalyzed electrochemical process and recent advancements, *Renew. Sustain. Energy Rev.* 40 779–797. 10.1016/j.rser.2014.07.109 3, 2014.
 3. Song J., L. Liu, Q. Yang, J. Liu, Ti. Yu, F. Yang and J. Crittenden, PVDF layer as a separator on the solution-side of air-cathodes: the electricity generation, fouling and regeneration, *RSC Advances* 65, 2015.
 4. Tatinclaux M., K.Gregoire, A.Leininger, J. C.Biffinger, L.Tender, M. Ramirez, A.Torrents, B. V.Kjellerup, Electricity generation from wastewater using a floating air cathode microbial fuel cell, *Water-Energy Nexus*, 1, 2, 97-103, 2018.
 5. Logan B. E., Electricity Generation Using an Air-Cathode Single Chamber Microbial Fuel Cell in the Presence and Absence of a Proton Exchange Membrane, *Environ. Sci. Technol.* 38, 14, 4040-4046, 2004.
 6. Duteanu N., B. Erable, S.M. Senthil Kumar, M.M. Ghangrekard, K. Scott, Effect of chemically modified Vulcan XC-72R on the performance of air-breathing cathode in a single-chamber microbial fuel cell, *Open Archive Toulouse Archive Ouverte*, DOI:10.1016/J.BIORTECH.2010.01.120
 7. Erable, B., Duteanu, N., Kumar, S.M.S., Feng, Y., Ghangrekar, M.M., Scott, K., Nitric acid activation of graphite granules to increase the performance of the non-catalyzed oxygen reduction reaction (ORR) for MFC applications, *Electrochemistry Communications*, 11, 1547–1549, 2009.
 8. Yu E.H., Cheng, S., Logan, B.E., Scott, K., Electrochemical reduction of oxygen with iron phthalocyanine in neutral media, *Journal of Applied Electrochemistry*, 1, 7, 2008.
 9. Zhang, L.,Liu, C., Zhuang, L., Li, W., Zhou, S., Zhang, J., Manganese dioxide as an alternative cathodic catalyst to platinum in microbial fuel cells. *Biosensors and Bioelectronics* 24, 2825–2829, 2009.
 10. Cheng S., Liu, H., Logan, B.E., Power densities using different cathode catalysts (Pt and CoTMPP) and polymer binders (Nafion and PTFE) in single chamber microbial fuel cells, *Environmental Science and Technology*, 40, 364–369, 2006.
 11. Wang, B., Han, J.I., A single chamber stackable microbial fuel cell with air cathode, *Biotechnology Letters*, 31, 387–393, 2009.
 12. Midyurova B., M. Dimova – Todorova, T. Panayotova, Partial ion exchange demineralization of natural waters, *Annual of Assen Zlatarov University*, XLIV, 40-43, 2015.

SOME FEATURES OF GASOIL EXTRACTION

Yordanka Tasheva
E-mail: jtasheva_2006@abv.bg

ABSTRACT

Ultra-deep desulphurization of fuels, particularly of gasoil, has become a very important subject in the global petroleum refining industry. The need for cleaner burning fuels has resulted in a continuing worldwide effort to reduce sulphur levels in gasoil. We investigated the liquid-liquid extraction of three gasoil blends with various polar solvents. Sulphur, arene content and polycyclic arenes were measured. The most effective solvent was furfural, a less effective solvent was N-methyl pyrrolidone and the least effective polar solvent was DEG.

Key words: sulphur, gasoil fraction, arene compounds, extraction

INTRODUCTION

Energy production is one of the most pressing issues of modern times. Economic activity and energy usage are intimately linked. The production of useful goods and services requires energy, and increased global economic output requires more energy usage. World energy usage went up by an average of 1.7% annually from 1980-2001, to a total of 404 quadrillion BTUs [1]. Although the percentage of energy obtained from fossil fuels declined over the same period, the share of world energy from fossil fuels is still over 82%, half of which comes from petroleum [1]

Unfortunately, the predominant modern technique for producing energy, the burning of fossil fuels, has a severe impact on the global environment. Part of this impact is the result of impure fuels. Naturally occurring sulphur compounds left in fuels lead to the emission of sulphur oxide gases. These gases react with water in the atmosphere to form sulphates and acid rain, which damages buildings, destroys automotive paint finishes, and acidifies soil, ultimately leading to loss of forests and other ecosystems [2]

Such utilities are not the only source of atmospheric sulphur. Automobiles are also adversely affected by sulphur compounds. Sulphur levels in automotive fuels have a profound effect of the efficacy of catalytic converters. Sulphur affects these emission control devices by strongly adsorbing to the precious metal catalysts, preventing the adsorption and reaction of hydrocarbons, nitrogen oxides, and carbon monoxide. The EPA estimates [3] that reducing sulphur levels from 400 ppm to 10 ppm reduces emissions of hydrocarbons by 45.9%, NO_x by 7.01%, and CO

by 31.12% by reducing the poisoning effect of sulphur. Obviously, emissions of SO_x are also reduced by an amount equivalent to the sulphur reduction. The US national average sulphur level in automotive fuel in 1997 was 339 ppm [4].

Producing energy in a clean and responsible manner can be accomplished in a number of ways. The use of non-fossil fuel energy sources such as solar, wind, and nuclear power will eventually replace fossil fuels. However, many of these technologies will take years to develop before they can provide the amounts of energy needed. In the near future, fossil fuel-based energy production will continue, and new technologies need to be developed in order to produce clean fuels to power our societies.

There is a stringent need for new methods of reducing sulphur content in fuel oils in order to satisfy the upcoming legislation that will limit the sulphur content more and more drastically. Indeed, environmental regulations for on-road diesel fuels planned in Europe call for a sulphur content reduction from the current level of 350 to 50 ppm by 2005 [5] and to 10 ppm by 2009, while in the US the actual level of 500 ppm will have to be decreased to 15 ppm in 2006 [3]. Similarly, Japan will impose a decrease from 500 to 50 ppm by the end of 2004 and is planning to further lower this limit to 15 ppm in the short/mid term. To achieve these new goals with the current hydrodesulphurization (HDS) technology, the use of higher temperature, higher pressure, larger reactor volume, and more active catalysts is indispensable, but costly. Therefore, new solutions were alternatively proposed; among them, desulfurization (DS) appeared as particularly promising. Indeed, DS can be con-

ducted at room temperature and under atmospheric pressure, which allows a substantial cost reduction. In such a process, DBTs are converted into sulphates that can be subsequently easily removed by conventional separation operations (e.g. distillation, solvent extraction, and adsorption) as their properties are significantly different from those of the hydrocarbons that constitute most of the fuel oils.

The aim of this paper is to study the desulphurization of gasoil fractions by extraction and to evaluate the effectiveness and selectivity of individual extraction systems.

EXPERIMENT

The extraction procedure is described in previous papers [6, 7].

It's known that the extraction process is generally represented as a heterophasic system because the mutual solubility at the selected experimental temperatures between solvents and petroleum products is negligible (below 0.001% by weight). It is obvious that, under intense stirring of the solvent-oil system at a certain number of revolutions, it will become a nanosystem since the size of the average diameter of the solvent droplets and those of the petroleum product will be below 100 nm. In intense stirring, a huge range of different quantities of diameters of the various droplets is obtained, which does not allow the use of conventional chemical kinetics to measure reaction rates. Apparently, in this case, fractal analysis and fractal kinetics should be applied, which requires special additional equipment to measure the diameter of the drops and their distribution by diameters. Since we did not use this apparatus, we refrained from examining the system using the methods of classical kinetics.

It must be noticed that the desulphurization of gasoil fractions by extraction was carried out in ambient temperature and atmospheric pressure. The conditions of extraction processes were established experimentally as follow: temperature – 60 °C, duration – 1.5, 3.0, 4.5 and 6.0 hours, and ratio gasoil blend: solvent = 1:1, 1:2.

It must be noticed that the extraction process of the individual systems was carried out at a constant stirring speed of 800 rpm.

In previous papers it has been established that the most effective solvents to apply in the extraction process of fuels are N-methyl pyrrolidone /NMP/, furfural and diethylene glycol /DEG/. Thus we used these organic polar solvents in

present investigations. The physical properties of solvents, dielectric constants and dipole moments are given in [5]. The dipole moment gives us preliminary information on the selectivity of the solvents, and the assessment of solvent solubility with respect to the individual raw materials gives us the critical dissolution temperature. As is known, the relative dielectric permeability (dielectric constant) characterizes the polarity of the solvents, and the extraction of sulphur compounds and arene hydrocarbons depends to a large extent on the nature of the solvent and especially on its polarity (μ).

As raw material we used gasoil fractions produced in Bulgaria, the so-called B-1, B-2 and B-3. The physicochemical properties of liquid fractions are given in Tables 1 to 3.

The critical dissolution temperatures of investigated gasoil blends are presented in Table. 4.

The sulphur content in raffinates was measured according to BSS EN ISO 8754 and the quantity of arene hydrocarbons were measured according to BSS ISO 2977.

The polycyclic arenes of the raffinates were measured, too.

Table 1. Physicochemical properties of B-1

	Parameters	Value
1.	Density at 20 °C, kg/m ³	827.0
2.	Distillation characteristics	
	i.p., °C	49
	10 %, °C	112
	20 %, °C	150
	30 %, °C	205
	40 %, °C	254
	50 %, °C	297
	60 %, °C	340
	To 130 °C, %	15.0
	To 150 °C, %	20.0
	To 200 °C, %	28.0
	To 360 °C, %	65.0
	e.p., °C	360
	Yield, %	70.0
	Residue + losses, %	30.0
3.	Asphaltene content, %	0.30
4.	Sulphur content, %	0.12

Table 2. Physicochemical properties of B-2

No	Parameters	Value
1.	Density at 20 °C, kg/m ³	836.0

2.	Distillation characteristics	
	i.p., °C	58
	10 %, °C	100
	20 %, °C	156
	30 %, °C	225
	40 %, °C	272
	50 %, °C	315
	60 %, °C	355
	To 130 °C, %	13.0
	To 150 °C, %	17.0
	To 200 °C, %	26.0
	To 360 °C, %	62.0
	e.p., °C	360
	Yield, %	67.0
	Residue + losses, %	33.0
3.	Asphaltene content, %	0.36
4.	Sulphur content, %	0.15

Table 3. Physicochemical properties of B-3

№	Parameters	Value
1.	Density at 20 °C, kg/m ³	849.0
2.	Distillation characteristics	
	i.p., °C	64
	10 %, °C	137
	20 %, °C	196
	30 %, °C	260
	40 %, °C	305
	50 %, °C	345
	60 %, °C	-
	To 130 °C, %	9.0
	To 150 °C, %	13.0
	To 200 °C, %	20.0
	To 360 °C, %	55.0
	e.p., °C	-
	Yield, %	65.0
	Residue + losses, %	35.0
3.	Asphaltene content, %	0.42
4.	Sulphur content, %	0.17

Table 4. Critical dissolution temperatures of gasoil blends

Gasoil blends	Critical dissolution temperature, °C		
	NMP	furfural	DEG
Gasoil blend B-1	68	65	76
Gasoil blend B-2	63	62	68
Gasoil blend B-3	65	64	67

RESULTS AND DISCUSSION

The obtained results from desulphurization and dearomatization processes by extraction are given in the following tables. The experimental data presented in Tables from 5 to 7 confirmed the literature data that the sulphur content depends mainly on the composition of raw material. The experimental results proved the decrease of sulphur and arene hydrocarbons at contact time more than 4.5 hours.

Table 5. Results of sulphur and arene content in raffinates from gasoil B-1

№	Sulphur content, ppm	Polycyclic arenes, %	Arene content, %
1.	498.6	4.6	12.6
2.	456.2	4.5	12.3
3.	405.3	4.4	11.7
4.	385.4	4.3	11.5
5.	356.1	4.1	11.4
6.	334.5	3.8	11.2
7.	298.9	3.6	11.0
8.	275.6	3.4	10.7

initial sulphur content – 1200 ppm, polycyclic arenes – 5.6 % (m/m), arenes – 20.2% (m/m)

Table 6. Results of sulphur and arene content in raffinates from gasoil B-2

№	Sulphur content, ppm	Polycyclic arenes, %	Arene content, %
1.	488.5	3.9	11.7
2.	436.6	3.6	11.5
3.	375.4	3.5	11.3
4.	355.6	3.4	11.1
5.	322.1	3.3	10.8
6.	287.3	3.2	10.7
7.	276.9	2.9	10.5
8.	256.8	2.9	10.3

initial sulphur content – 1500 ppm, polycyclic arenes – 5.6 % (m/m), arenes – 20.2% (m/m)

Table 7. Results of sulphur and arene content in raffinates from gasoil B-3

№	Sulphur content, ppm	Polycyclic arenes, %	Arene content, %
1.	475.6	4.2	11.6
2.	421.2	4.0	11.4
3.	385.6	3.7	10.9
4.	352.3	3.5	10.7
5.	312.6	3.3	10.5
6.	289.6	3.2	10.2
7.	277.4	2.8	9.9
8.	269.5	2.7	9.7

initial sulphur content – 1700 ppm, polycyclic arenes – 5.6 % (m/m), arenes – 20.2% (m/m)

It can be seen from the tables that the selective solvents lead to the purification of sulphur compounds to a large part. Furfural can be distinguished as the most selective solvent, N-methylpyrrolidone is less selective, and the least effective is the DEG.

The degree of decrease of arene hydrocarbons during the time contact was calculated. The degree of decrease of arene hydrocarbons in percentage terms from duration is presented in Figures 1 to 3.

As can be seen the extraction processes of the investigated gasoil and its purification from arene hydrocarbons are the best at duration of the individual extraction systems of 6 hours, for 4.5 hours the degrees of decrease of arene hydrocarbons are about 30 %, respectively. The smallest percentage of decrease of arene hydrocarbons is obtained at 3.0 and 1.5 hours for all used polar solvents and mixtures B-1, B-2 and B-3.

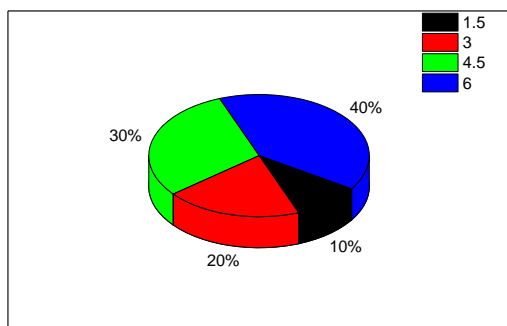


Fig. 1. Dependence of degree of decrease of arene hydrocarbons on duration of the extraction process with furfural of B-1

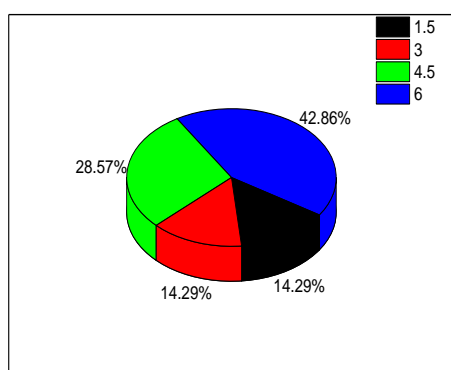


Fig. 2 Dependence of degree of decrease of arene hydrocarbons on duration of the extraction process with DEG of B-2

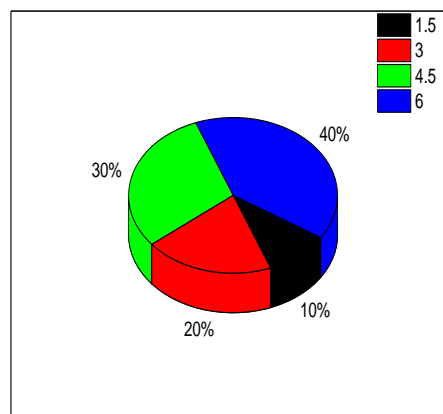


Fig. 3 Dependence of degree of decrease of arene hydrocarbons on duration of the extraction process with N-methylpyrrolidone of B-3

CONCLUSION

The possibility of extraction with selective solvents has been investigated to reduce the content of sulphur compounds and arenes hydrocarbons from gasoil mixtures produced in Bulgaria. It has been found out that all selected and tested by us selective solvents reduce, albeit to varying degrees, the content of sulphur compounds. The most polar solvents used by us are N-methylpyrrolidone, furfural and diethylene glycol. The content of polycyclic hydrocarbons was measured, too. The dependencies of the degree of decrease on the duration the extraction processes indicate that the best duration of extraction for all gasoil blends is 6.0 hours, better decrease of arene hydrocarbons is obtained at duration of 4.5 hours.

ACKNOWLEDGMENT

This research has been supported by contract №KII-06-H27/12 of 11.12.2018 “Modeling and elaboration of complex system for selection of transport technology in transport network”, funded by the National Science Fund of the Ministry of Education and Science of Bulgaria.

REFERENCES

1. Nehlsen, J. *Disertation of Faculty of Princeton University*, Nov., 2005.
2. Ishihara, A., D. Wang, H. Amano et all. *Applied Catalysis A: General*, **279**, (2005), p. 279.
3. Eneh, O. *Journal of applied Sciences*, **11**, (2011), p. 2680.

4. Jiang, Z., L. Hongyinga, Zh. Yongna et al., *Chinese Journal of Catalysis*, **32**, (2011), p.707.
5. Wang, H., H. Jianxun, Y. Cairong et al., *China Petroleum Processing and Petrochemical Technology Scientific Research*, **16**, (2014), p. 65.
6. Lazarov, I., P.Petkov, J.Tasheva et al. *Oxidation Communications*, **30**, (2007), p.51.
7. Tasheva, Y., *PhD thesis*, HAC – Sofia,2006.

TESTING RAW COW MILK USED FOR DAIRY PRODUCTS

Galina Grigorova
E-mail: galinakirova@abv.bg

ABSTRACT

This paper presents a microbiological and physicochemical study of raw cow milk to be used for dairy products. This study was performed in the months April, May and June. The results were referenced to the mandatory standards as per Regulation No. 2/27.02.2017. The resulting details demonstrate satisfactory results for all samples of raw cow milk.

Key words: raw cow milk, freezing point, fat, total microbial count, somatic cells.

INTRODUCTION

In recent years, human nutritional demands have been associated with balanced and healthy food. Modern studies of milk and the related dairy products are focused on improving their biological sufficiency and health effects. Milk is the product of living organisms subjected to a continuous contact with the environment, and changes occurring in the environment result in changes of the properties of milk and its components. Milk is a favourable environment for microorganisms, which cause further and more significant changes in milk. The quality of dairy products is determined on the basis of both milk quality and development of microbiological and physicochemical processes in the milk during processing [1]. Various factors influence milk composition and properties: animal breed, animal age and fat and protein content. The highest percentage of fat can be seen with cows aged approx. 4 years, during lactation period 5, while the lowest content of fat in milk is found during months 2 to 3 lactation period [1]. Prior to the end of milk production (10-15 days) at the end of the lactation period, the fat in milk gradually increases. Further factors that influence milk composition are the health condition of the animal, diet, and in the case of prolonged malnutrition, milk quality deteriorates, decreasing the level of fat, proteins and dry substance. Milk composition is associated with environmental effects. High temperature and high relative humidity result in decreased level of fat in milk. The quality and quantity compositions of micro flora of raw milk vary in wide ranges. Even in milk produced in aseptic conditions, it contains microorganisms and their quantity may vary from a single cell to thousands of cells per millilitre. Milk micro flora is

comprised mainly of lactic acid bacteria, staphylococci, streptococci, and micrococci. Ambient temperature in the range of 20 to 37°C causes the development of mainly lactic acid micro flora, and it leads to increased milk acidity that stimulates coagulation. Such micro flora is represented by streptococci, though endobacteria, which are resistant to temperature variations, may also develop. At 5-15°C, psychotrophic micro flora of gram-negative bacteria will develop, among numerous lipolytic and protolithic species that will slowly, though certainly impair the quality of milk [2]. The addition of water to milk is the most frequent counterfeit. It results in lower nutritional value; lower production yields, and potential contamination with hazardous pathogenic micro flora [1]. Mandatory norms related to the total microbial burden of milk, as specified in Regulation No. 2/ 2017, state that the total microbial count for raw milk must not exceed 100 000 CFU/ml, while the total count of somatic cells must be 400 000 count/ml.

The aim of this analysis is to study the quality of raw cow milk for use in dairy production. In order to achieve this goal, I have set the following tasks: study of the physicochemical parameters (fat and freezing point) and of the microbiological condition of raw cow milk.

EXPERIMENT

Materials and methods

Materials

For determination of fat content in milk, use is made of 3-methylbutanole and sulphuric acid supplied by Sigma-Aldrich, Germany. Colony counting is performed in solid nutrient media (Skim Milk PCA), manufactured by HiMedia;

and Maximum Recovery Diluent, supplied by HiMedia.

Samples of raw cow milk to be analyzed were collected during April, May and June in the region of Burgas.

Methods

Determination of freezing point of raw cow milk via a cryoscopy method using CryoStar I, Funke Gerber as per BDS EN ISO 5764 [3].

Samples are stored at temperatures in the range of 0 to 5°C. The temperatures of the standard solutions (Calibration Standard A – 0.000 ±0.0005°C and Calibration Standard with - 0.557 ±0.0005°C, made by Funke-Gerber), and the milk samples temperature are identical. The glass with the sample is turned upside down with care and agitated via circular movements until the contents have been homogenized. Then, 2.5ml of the milk sample is transferred in a clean, dry glass container using a pipette. Then, the tube containing the sample of milk is placed in a cryoscope (CryoStar I, Funke Gerber).

Determination of fat content in raw cow milk as per ISO 2446 [6]

By using this method, we separate the fat component from the milk with a butyrometer (Funke Gerber - Berlin) using centrifugation, following a protein reaction with sulphuric acid. Fat separation is promoted by addition of 1 ml (3-methylbutanole). To a portion of 10 ml concentrated sulphuric acid, density 1,816 ±0,04 kg/dm, we add 11 ml milk at the walls of the butyrometer. Following complete destruction of protein, we agitate well and add 1 ml 3-methylbutanole. The sample is then tempered and centrifuged. We read fat level as percentage from the butyrometer scale.

Determination of total microbial count (TMC) as per BDS EN ISO 4833-1 [5]

Under sterile conditions using a well-homogenized sample we take 1 ml milk and transfer it into a portion of 9 ml diluent (Maximum Recovery Diluent). On the inoculate we pour approx. 15-18 ml melted and cooled fat (down to 44 - 47°C from the solid nutrient media (Skim Milk PCA). Plates are cultivated bottoms up in a thermostat at temperature of 30°C for 72h. We determine the aerobe and optional anaerobic microorganisms using a

colony counter, Conta colonie, 185, Astori, where counting is applied for plates that contain more than 15 and less than 300 colonies.

Determination of Total Somatic Cell Count (TSCC) as per BDS EN ISO 13366-1 [7]

From the test sample prepared by this method, we spread milk using a micropipette; amount 0, 01 ml, on the slide sized 1 cm². Following sample drying, dye reagents are applied, Newman - Lampert modification. We make determination under a microscope (BM 180, Boeco) of cells equal to or greater than 8 µm diameter, with well visible nuclei.

RESULTS AND DISCUSSION

The determination was performed with raw cow milk used in dairy production by physicochemical methods: fat content and freezing point, and microbiological TMC and TSCC. The samples of raw milk were tested in the period April – June. The test results for raw cow milk based on physicochemical parameters are summarized in Table 1. The determination showed that the quality of test samples for the parameters of fat content and freezing point comply with the requirements of Regulation No 2. Fat content in the test samples was in the range of 3,5% to 3,8%, in conformity with the standards for fat level in raw cow milk. The determination showed that the fat level was the lowest, 3,5%, in June. The fat content of all samples was higher than 3,4%, corresponding to the requirements of Regulation No 2. The freezing point parameter was within the normal range for cow milk, from -0,534 to -0,518°C. As per the requirements of Regulation No2, the freezing point parameter did not exceed -0,507.

Table 1. Physicochemical parameters of raw cow milk (n=30)

Parameters	Period	Raw cow milk Average	Statutory requirements of Regulation 2
Fat, %	April	3,8% ±0,1	Minimum or equal to 2,6%
	May	3,7% ±0,1	
	June	3,5% ±0,1	

Freezing point, C°	April	Minus 0,531 ⁰ C	Minus 0,507 ⁰ C
	May	± 0,006	Maximum
		Minus 0,529 ⁰ C	
	June	± 0,005	
		Minus 0,528 ⁰ C	
		± 0,004	

The microbiological parameters of raw cow milk are shown in Table 2. The determination demonstrated that all 30-off test samples analyzed are in the allowable range in terms of total microbial count. The average TMC of the samples of raw milk was $8,5 \times 10^4$ CfU/ml⁴

Table 2. Microbiological parameters of raw cow milk (n=30)

Period	Somatic cells Count /ml	Total microbial count CfU/ml, (average count)
April	209 500	73 545
May	234 700	83 363
June	305 803	97 272

As found from the microbiological studies, the various forms of mastitis in cows and goats are due to bacteria from the group of staphylococci, enterobacteria, mycoplasmas, etc. [9]. Determination was made of the average content of somatic cells for the entire study period, from April: 209 500 count /ml; May 234 700 count /ml, June 305 803 count /ml. Regarding the total microbial count in raw cow milk, the determination showed that all milk types were within the specified range in conformity with Regulation No 2. With reference to the maximum allowable limit for total microbial count, raw cow milk must not exceed 100 000. All test samples analyzed contained less than 400000 count/ml $\times 10^3$ somatic cells, being

in conformity with the requirements of Regulation No 2. This shows that such raw milk can be used for processing, without having to apply pasteurization. According to the maximum allowable limits for dairy products, as specified in Regulation No 2, avoiding thermal process, all milk samples analyzed in the period April – June have TMC below 100 000. This means that, in terms of microbiological parameters, they were conformant to the norms. Hygiene control of raw cow milk process is of high importance for its safety.

REFERENCES

1. Dimov, N. Iv. Georgiev, S.Velev and H.Chomakov. *Milk and dairy products control*, Sofia (1974), p.9-15
2. Antonova-Nikolova, S. L.Yocheva and I. Ivanova. *Nutritional microbiolog*, University publishing house “Sv. Climent Ochridski”, Sofia, (2015), p.131-133
3. BDS EN ISO 5764 *Milk-Determination of freezing point-Thermistor cryoscope method (Reference method)*.
4. BDS ISO 7218: 2002 / A1:2013. *Microbiology – Main rules for microbiological testing*).
5. BDS EN ISO 4833-1:2013. *Microbiology of food and animal feeding stuffs - Horizontal method for the enumeration of microorganisms - Colony-count technique at 30 degrees*).
6. ISO 2446. Milk. *Determination of fat content. Routine method (Gerber method)*
7. BDS EN ISO 13366-1. *Milk. Counting of somatic cells. Part 1: Microscopic method. (Reference method)*.
8. Regulation No. 2 dated February 23, 2017. *on the Specific requirements for production, collection, transport and processing of raw cow milk, offered at the market for milk and dairy products and the relevant official control*.

BREAD YEAST - VITALITY AND VIABILITY, ENDURANCE AND STORAGE STABILITY

Galina Yordanova, Milka Atanasova, Ruska Nenkova

E-mail:burdelova@abv.bg

ABSTRACT

The quality of Saccharomyces cerevisiae bread yeast is determined by many parameters, including its viability and freezing resistance. Fresh yeast was frozen at a temperature of - 20°C and thawing was carried out at room temperature. The storage stability of three different types of bread yeast, fresh, dry and frozen, was also investigated. It was found out that, with increasing the time, viability gradually decreased. As a result of continuous freezing and thawing there was a decline in the vitality and viability of bread yeast. These results will help to ensure quality control of yeast and bread respectively.

Key words: *Saccharomyces cerevisiae, viability, freezing, stability, storage*

INTRODUCTION

The assessment of bread yeast cells is very important in many areas of industrial microbiology. Controlling the total number, dead and living cells, as well as active yeast cells is crucial in the production of bread yeast. The most common method to determine cell number is related to yeast staining with methylene blue and counting by microscopic examination on a glass slide. Methylene blue staining is a bright-field staining procedure in which dead or nonviable cells are stained blue, whereas viable cells are able to exclude (or reduce) the dye and remain colourless. This method is simple, but must be used with caution, because the results can be influenced by the physical state of the cell membrane or the physiological state of individual cells, which vary depending upon their age, culturing conditions, and position in the cell cycle.

In this work we used a new fluorescence image cytometer, Easycounter YC (Milkotronic Ltd., Bulgaria), for determination of total cell number and viability of yeast cells. Introduction of automated devices for counting live and dead cells and determining their viability is very important for the accuracy of the analysis because it eliminates the human factor present in the microscopic counting of cells. In addition, the replacement of methylene blue with a fluorescent dye allows for a more sensitive analysis to be made. The fluorescent dye binds to the DNA of dead cells and thus determines their number. This method is suitable for effective quality control of yeast production, as well as for monitor-

ing yeast stability over time. The developed method uses a new DNA fluorescent dye with a higher fluorescence yield that is not permeable to viable cells [1].

The ability of cells to survive freezing and thawing is expected to depend on the physiological conditions experienced prior to freezing. Loss of viability was proportional to the freezing duration, indicating that freezing is the main determinant of freeze-thaw damage. Yeast did not adapt to freeze-thaw stress following repeated freeze-thaw treatment with or without a recovery period between freeze-thaw cycles, nor could it adapt following pre-treatment by cold shock [2].

Freezing is used for many industrial, medical, food technological, and scientific purposes, such as strain preservation, organ preservation, and cryosurgery. The *Saccharomyces cerevisiae* yeast is an appropriate eukaryotic organism to study the physiological parameters that affect the cell ability to survive freeze-thaw injury. Moreover, there is a range of available mutations affecting cellular responses to various types of stress that may be incurred during freeze-thaw injury which can be exploited to understand the nature of freeze-thaw injury and how to avoid it. Intracellular ice formation during freezing has been described for many cellular systems, and the rate at which ice is formed determines the type of freezing damage suffered by cells [3, 4]. Cells can be injured during freezing by physical factors such as ice crystal formation and dehydration. At high freezing rates, intracellular freezing occurs, leading to cell damage mainly by ice crystal formation. The freezing rate is

determined by the characteristics of a cell, such as shape, structure, surface area-to-volume ratio, and membrane permeability. Therefore, each cell has its own specific freezing rate for fast or slow freezing. Cells can also undergo biochemical damage, including oxidative stress from reactive oxygen species formed during the thawing process. Yeast cells show different degrees of tolerance, depending on their growth state, and indicating that their physiological state determines the stress resistance. Like other stress situations, yeast cells can handle freezing and thawing by the synthesis of stress proteins or metabolites such as trehalose and glycerol, which are produced in large quantities in abnormal situations [2].

Other authors study the effects of freezing and frozen storage of bread dough and compressed yeast on bread quality. Besides, the effects of compressed yeast freezing on cell viability, gas production and release of substances by the yeast cells are examined. Freezing and frozen storage of dough made with fresh yeast have more negative effects on baking quality than the addition of frozen yeast to dough. When the compressed yeast is frozen and stored at -18°C , CO_2 production decreases, while the amount of dead cells, the total protein, and the total reducing substances leached from the yeast increases as the length of yeast frozen storage increases [5].

In this work, the influence of freezing and thawing on the viability and vitality of yeast cells and endurance of yeast in time was studied. The aim of this study was to determine the resistance of bread yeast to frequent freezing and thawing under the refrigeration conditions. The storage stability of bread yeast depending on their vitality and viability was also investigated.

MATERIALS AND METHODS

1. Materials

Saccharomyces cerevisiae – fresh, dry and frozen compressed yeast from various manufacturers was supplied from the market. A fluorescence image cytometer, Easycounter YC (Milkotronic Ltd., Bulgaria) for determination of total cell count and viability of yeast cells was used. A

new fluorescent DNA dye POTEDM-1 with high fluorescence quantum yield was employed.

2. Methods

Yeast freezing. The compressed yeast was frozen at -20°C . The samples were evaluated at the beginning and then frozen for a fixed period (days). Viability and vitality of yeast cells were determined based on the total number and the number of dead cells after thawing for 30 min at 25°C .

Determination of cell viability: The fluorescence imaging cytometer has an innovative optical system based on tuneable thin-film optical filters, Semrock's VersaChrome filters. The apparatus detects individual cells in suspension using image-based technology. EASYCOUNTER YC detects individual cells in suspension by detecting fluorescent signals of stained DNA in the cell nuclei. Fluorescent dye SOFIA GREEN was used. This fluorescence dye is not permeable to viable cells. It can only penetrate through a compromised cell membrane of dead cells, allowing the cellular DNA to be stained. For determination of the total number of cells, it was necessary to mix the yeast cell suspension with a lysis reagent and a fluorescent dye, which had been dried in advance. The lysis reagent permeates the yeast cell wall and the membranes, allowing the cellular DNA to be stained. $8\mu\text{l}$ of the final sample with all cells stained was loaded into the Easycounter YC counting chip. The second sample with stained dead cells only was loaded into another Easycounter YC counting chip, then imaged and counted on the Easycounter YC cytometer. The duration of the analysis depends on the number of recorded fields.

Determination of cell vitality: The method is based on measuring the activity of the esterase enzyme using the esterase substrate 5-carboxyfluorescein diacetate (CFDA). For the purpose it was necessary to determine the total number of cells by the method described above. The CFDA penetrated the cell membrane of living cells, diacetate groups were cleaved by non-specific esterases, and a fluorescent charged substrate (carboxyfluorescein) was formed. As a result of this reaction, the cells were stained in green.

A very important factor is the dilution of the sample.

$$\text{Viability, \%} = \frac{\text{total cell number} - \text{number of dead cells}}{\text{total cell number}} * 100$$

Calculation of the coefficient of variation (CV): The coefficient of variation (CV) is a measure of relative variability. It is generally accepted that a random event follows the Poisson distribution, according to which the expected standard deviation is equivalent to the square root of the number of counted cells. Therefore the CV is the ratio of the standard deviation to the mean (average).

$$\text{Coefficient of Variation} = \frac{\text{Standard Deviation}}{\text{Mean}} * 100.$$

RESULTS AND DISCUSSION

Vitality and viability of yeast cells (fresh, frozen and dry) were determined using a fluorescence image cytometer, Easycounter YC.

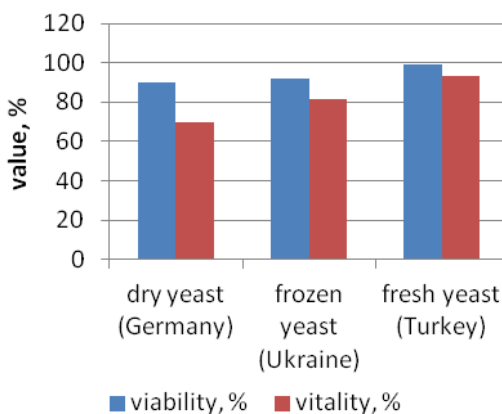


Fig. 1. Vitality and viability of yeast cells (fresh, frozen and dry)

Figure 1 shows that viability and vitality were the highest for fresh yeast compared to the other two types. The results were confirmed by previous work [6]. The living cells in the three types of yeast were in a large number compared with the metabolically active cells.

The coefficient of variation (CV, %) was determined. In most cases, when comparing fresh and frozen yeast, the coefficient of variation of fresh yeast was lower. Both yeast types had a lower coefficient of variation in the range of $7,5 \cdot 10^4$ - $5 \cdot 10^6$. The highest deviation resulted after $1 \cdot 10^7$.

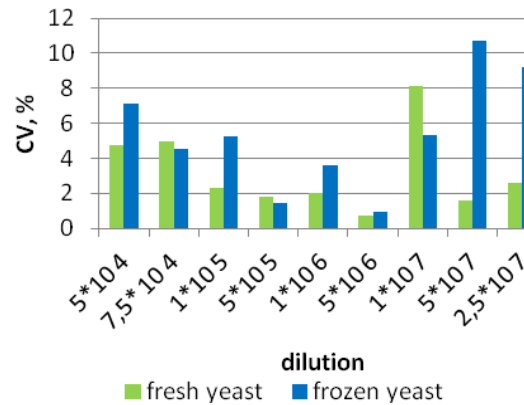


Fig. 2. Coefficient of variation for fresh and frozen yeast at different dilution

The resistance of fresh yeast to freezing (-20°C) and thawing (room temperature) was also investigated.

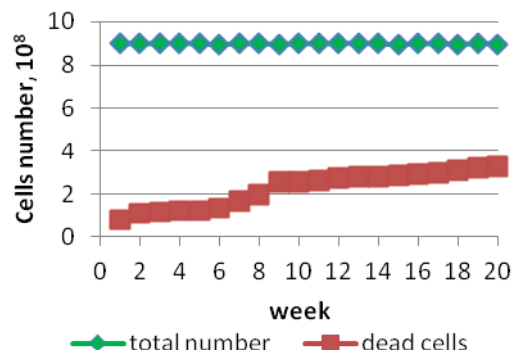


Fig. 3. Total number and dead cells of fresh yeast during freezing and thawing

The total number and the dead cells number of fresh yeast were determined during the process of freezing and thawing and the results are presented in Fig. 3. As could be seen, the number of dead cells increased with time. This was evidenced by the microscopic images taken at the initial stage and after 40 days.

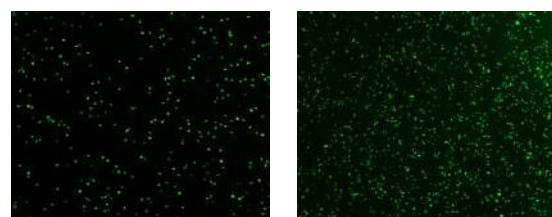


Fig. 4. Images of samples of *Saccharomyces cerevisiae*: a) dead cells number at the initial stage b) dead cells number after 40 days;

Vitality and viability of fresh yeast cells during the freezing and thawing process were investigated.

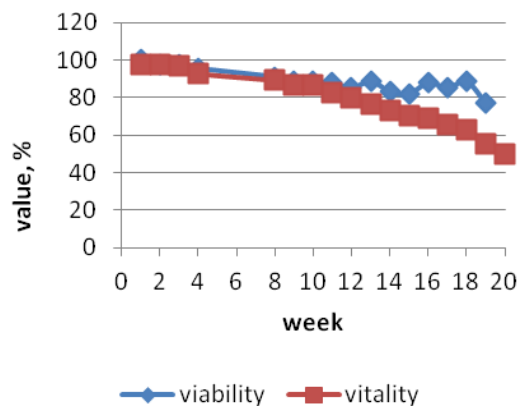


Fig. 5. Vitality and viability of fresh yeast cells during the freezing and thawing process

The presented results show that the vitality of the fresh yeast cells gradually decreased after repeated freezing and thawing. Similar results were observed for the viability of yeast cells, but its values remained slightly higher.

The stability of the three types of bread yeast stored at different temperatures was also measured: fresh yeast (temperature 4 - 8°C), frozen yeast (temperature -20°C), dry yeast (temperature 20°C).

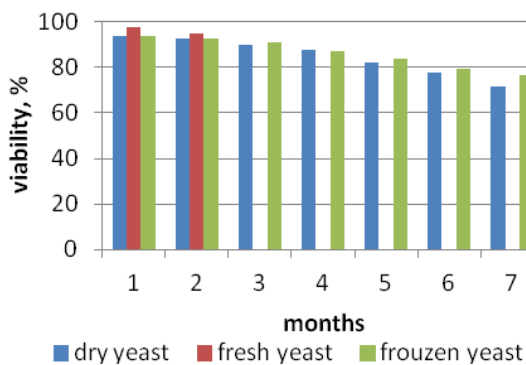


Fig. 6. Viability and storage stability of the three types of yeast (dry, fresh and frozen)

There was no significant difference in viability between the three types of yeast in the first two months after opening. In the third month the fresh yeast was contaminated with mold, so it was removed from the analysis. In the next four months a slow decrease in the viability of dry and frozen yeast was noticed.

CONCLUSION

Viability and vitality of yeast cells (fresh, frozen and dry) were measured with an EasyCounter YC fluorescence counter. The highest viability and vitality were determined for the fresh yeast cells. The living cells in the three types of bread yeast were in a large number compared with the metabolically active cells.

The coefficient of variation of fresh yeast is lower than the frozen yeast. The resistance of fresh yeast to freezing and thawing was also investigated. The results showed that the number of dead cells increased over time.

The stability of the three types of bread yeast stored at different temperatures was also measured and no significant difference in viability was noticed in the first two months after opening.

REFERENCES

- Atanasova M, G. Yordanova, R. Nenkova, Y. Ivanov, T. Godjevargova & D. Dinev. *Brewing Yeast Viability Measured Using A Novel Fluorescent Dye And Image Cytometer. Biotechnology & Biotechnological Equipment.* 2019.
- Park J, M C. Grant, P. V. Attfield and I. W. Dawes. *The Freeze-Thaw Stress Response of the Yeast Saccharomyces cerevisiae Is Growth Phase Specific and Is Controlled by Nutritional State via the RAS-Cyclic AMP Signal Transduction Pathway. Applied And Nvironmental Microbiology,* Vol. 63, No. 10 Oct. 1997, p. 3818–3824.
- Mazur P. 1970. *Cryobiology: the freezing of biological systems. Science* 168:939–949.
- Toner M., E. G. Cravalho, and M. Karel. 1993. *Cellular response of mouse oocytes to freezing stress: prediction of intracellula ice formation. J. Biomech. Eng.* 115:169–174.
- Ribotta P. D., A. E. León and M. C. Añón. *Effects of Yeast Freezing in Frozen Dough Cereal Chem.* 2003, 80(4):454–458.
- Yordanova G, M. Brinkova, D. Yordanov, R. Nenkova. *Study Of The Viability Of Baker's Yeast And Optimal Development Conditions. Annual Of Assen Zlatarov University, Burgas Bulgaria,* 2018, v. XLVII (1).

AN OPTIMAL ORIENTED APPROACH TO THE SUSTAINABLE SUPPLY CHAIN DESIGN FOR BIOREFINERY

Desislava Nikolova
E-mail: desislava-nikolova@btu.bg

ABSTRACT

The paper deals with the problem of optimal oriented approach to the sustainable biorefinery supply chain design. This is a key instrument for achieving sustainability. The document considers the economic, environmental, social, political and technological influencing factors for sustainability. The problem is formulated in terms of Multi-Objective Optimization. Compromise between five conflicting criteria is achieved by non-domination of any other solution.

Key words: supply chain, biorefinery, optimization approach, sustainability

INTRODUCTION

Biorefineries have been popular as a sustainable alternative to fossil sources in the production of energy, chemicals and materials. However, controversies related to the actual sustainability effects of biorefineries have been raised in recent years [1]. The sustainability of biorefineries is increasingly monitored and evaluated through certification schemes that measure the impact of bio production [2]. To address the problem new Clean Energy for All Europeans rules came into force in 2015 to reduce the risk of indirect land use change – in both the Renewable Energy Directive 2009/28/EC and the Fuel Quality Directive 2009/30/EC. As a result, sustainability has become a central topic of study for bio-refining systems.

According to the International Energy Agency (IEA), "bio-refining is the sustainable synergistic processing of biomass in a wide scale of products (chemicals, materials) and energy (fuels, heat)" [3]. Essentially, biorefineries include facilities only for biomass processing [4]. According to the feedstock used, biorefineries can be classified into a few generations. First-generation biorefineries use food crops such as sunflower, sugar beet and others. Most of the feedstock used in this process can be used as food, too [5]. In this way they endanger the safety of food supply. Second-generation biorefineries use non-food materials, such as agricultural residues, wood and energy crops, usually

having a high lignocellulose content [6]. Third generation biorefineries use algae biomass [7].

The production from biorefineries necessitates a flow of the biomass feedstock from the supply centers to the demand centers. Along this scheme, the biomass passes through some facilities and undergoes various processes called supply chain for biorefinery. In addition, depending on the type of biomass, final product, and the conversion technology, it may be necessary to introduce some pre-treatment, intermediate, and blending sites in the supply chain. The striving for higher economic results coupled with social satisfaction, while respecting the environmental requirements, can be met by building and managing an appropriate supply chain.

In this paper a new approach, called TBL þ or Triple Bottom Line Plus, is researched. This approach differs from the typically used sustainability criteria that include only economic, social and environmental aspects. The sustainability lines in the current paper also cover technological and political factors [8]. An optimally oriented approach to the sustainable supply chain design for a biorefinery is presented. The aim is to find solutions that achieve a compromise between several conflicting criteria. The problem is formulated as a multi-objective problem.

PROBLEM DESCRIPTION

The solutions related to the sustainable supply chain for a biorefinery are a hierarchical model of 3 levels (Fig. 1):



Fig. 1 The hierarchical model

Strategic planning is a forecast level. Tactical planning aims to relate forecasts to specific user requests. Operational planning solves tasks related to creating optimal schedules.

The problem of designing a sustainable supply chain (for biorefinery) is very extensive. In general, strategic activities are formulated as a search for the following solutions:

- target markets selection;
- target the plant location;
- capacity and production technology;
- biomass selection type and location.

These decisions aim at the realization of a sustainable supply chain for biorefineries, namely by observing economic, social, environmental, political, and technical aspects.

MATHEMATICAL MODEL

Biorefinery supply chain configuration related to the strategical decision-making level is characterized by a set of decision variables. They are graphically presented in Fig. 2.

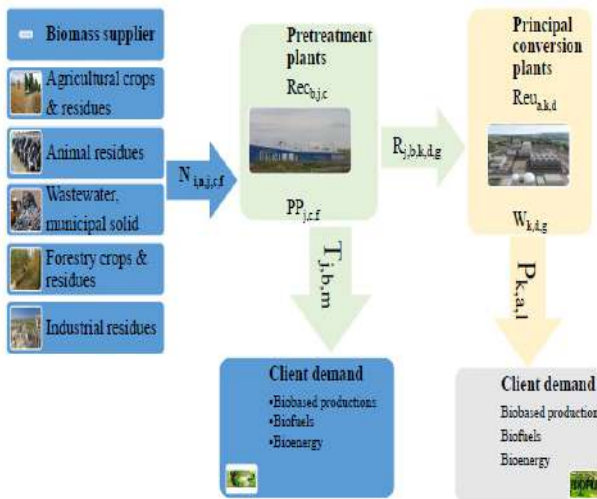


Fig. 2 Biorefinery supply chain configuration

The presented mathematical model includes five objective functions. A similar task was developed in [9]. This type of problems is known as Multi-Objective Optimization Problems. In

this case the objectives are often in conflict with each other. Thus, the improvement of one objective may lead to the deterioration of another. An optimal oriented solution is the one that is non-dominated by any other solution.

The mathematical formulation is presented as follows:

Indices:

- a - Type of final product;
- b - Type of intermediate product;
- c - Production technology at pre-treatment;
- d - Production technology at conversion plants;
- f - Transformation capacity at pre-treatment;
- g - Transformation capacity at conversion plant;
- i - Location of supplier;
- j - Location of pre-treatment;
- k - Location of conversion plants;
- l - Location of final product demand;
- m - Location of intermediate product demand;
- n - Type of feedstock.

Binary variables:

- $W_{k,d,g}$ - 1 If the main production plant is built in location k with technology d and capacity g , 0 otherwise;
- $PP_{j,c,f}$ - 1 If the pre-treatment plant is built in location j with technology c and capacity f , 0 otherwise;

Continuous variables:

- $N_{i,n,j,c,f}$ - Flow of raw materials type n from the supplier located at i to pre-treatment located at j to be processed with technology c and processing capacity f ;
- $R_{j,b,k,d,g}$ - Flow of intermediate products type b , from pre-treatment located at j to the main production plant located at k to be processed with technology d and processing capacity g ;
- $T_{j,b,m}$ - Flow of intermediate products type b from pre-treatment located at j to the client located at m ;
- $P_{k,a,l}$ - Flow of final products type a from the main production plant located at k to the client located at l ;
- $Re_{b,j,c}$ - Reuse flow of intermediate products type b at pre-treatment plant located at j and processed by technology c ;

$Reu_{a,k,d}$ - Reuse flow of final products type a at the main production plant located at k and processed by technology d ;

$IncP_j$ - Amount of government incentives for biorefinery plants installation at location j ;

$IncW_k$ - Amount of government incentives for setting up a production plant at location k ;

$InvTechW_d$ - Amount invested by the government in technology d ;

$InvTechP_c$ - Amount invested by the government in technology c ;

$GovInvE$ - Governmental investments constraint for electric infrastructure.

Parameters:

$TaxRed_a, TaxRed_b$ - Tax exemption in euro per ton of sold bio product types a and b ;

$DiscountRate$ - Value of discount rate for biorefinery projects;

y - Years for project evaluation;

ε - The soil deterioration rate.

Restrictions:

The restrictions apply to:

- Raw materials to be consumed in biorefineries are limited by its availability at each supplier location;
- Restrictions related to production capacity at pre-treatment plants and principal plants respectively;
- Production capacity and technology by plant;
- Maximum demand

Objective functions:

Economic optimization includes maximization of the profit:

$$\begin{aligned} & \text{Max} \sum_{y=1}^T \frac{NetCashFlow_y}{(1 + DiscountRate)^y} - \\ & \text{InitialInvestment} + \left(\sum_j IncP_j + \sum_k IncW_k \right) \end{aligned} \quad (1)$$

Environmental optimization includes minimization of the total amount of equivalent CO_2 generated at the whole biorefinery supply chain:

$$\begin{aligned} & \left. \begin{aligned} & \sum_i \sum_n CO_{2i,n} \left(\sum_j \sum_c \sum_f N_{i,n,j,c,f} \right) + \\ & \sum_n \sum_c \sum_f CO_{2n,c,f} \left(\sum_j \sum_i N_{i,n,j,c,f} \right) + \\ & \sum_b \sum_d \sum_g CO_{2b,d,g} \left(\sum_k \sum_j R_{j,b,k,d,g} \right) + \\ & \sum_a CO_{2,a} \left(\sum_k \sum_l P_{k,a,l} \right) + \sum_b CO_{2,b} \left(\sum_j \sum_m T_{j,b,m} \right) + \\ & \sum_i \sum_n \sum_j CO_{2i,n,j} \left(\sum_c \sum_f N_{i,n,j,c,f} \right) + \\ & \sum_j \sum_b \sum_k CO_{2j,b,k} \left(\sum_d \sum_g R_{j,b,k,d,g} \right) + \\ & \sum_k \sum_a \sum_l CO_{2,k,a,l} P_{k,a,l} + \sum_j \sum_b \sum_m CO_{2,j,b,m} T_{j,b,m} \end{aligned} \right\} \quad (2) \end{aligned}$$

Social optimization includes minimization of the locations selected in lands with conflicts:

$$\begin{aligned} & \left. \begin{aligned} & \sum_i ConfLand \left(\frac{\sum_n \sum_j \sum_c \sum_f N_{i,n,j,c,f}}{\sum_n \sum_j \sum_c \sum_f N_{i,n,j,c,f} + \varepsilon} \right) + \\ & \sum_j ConfLand \sum_c \sum_f (PP_{j,c,f}) + \\ & \sum_k ConfLand \sum_d \sum_g (W_{k,d,g}) \end{aligned} \right\} \quad (3) \end{aligned}$$

Political optimization includes minimization of the government expenditures:

$$\begin{aligned} & \text{Min} \left(IncP_j + IncW_k + \sum_b TaxRed_b \left(\sum_j \sum_m T_{j,b,m} \right) + \right. \\ & \left. GovInvE - \sum_a TaxRed_a \left(\sum_k \sum_l P_{k,a,l} \right) + \sum_c InvTechP_c + \sum_d InvTechW_d \right) \end{aligned} \quad (4)$$

Technological optimization includes minimization of the total amount of raw materials:

$$\text{Min} \left\{ \sum_n \sum_i \sum_j \sum_c \sum_f N_{i,n,j,c,f} \right\} \quad (5)$$

This optimal oriented approach is used to transform multicriteria problems in objective optimization. The aim of the optimization is to determine the values of variables that provide an optimum of the objective functions according to the restrictions. This problem is formulated as a multi-objective problem.

CONCLUSIONS

The current dynamic market development requires quick capacities regrouping of the bio-processing industry. Therefore, the formation of

supply chains for biorefinery is essential in order to achieve the desired flexibility in accordance with a sustainable progress.

This paper presents an optimal oriented approach for the design of Supply Chain for biorefinery using economic, environmental, social, technological and political criteria. The presented model allows for maximization of the economic profit, reduction of the harmful emissions released, minimization of social and political requirements in the chain by making the necessary compromises. The design of an optimal supply chain for biorefinery can solve a wide range of issues (includes strategic decisions), because this area changes very fast.

The problem is formulated as a task of mixed integer non-linear mathematical programming (MINLP).

ACKNOWLEDGEMENTS

This work was supported by the Bulgarian Ministry of Education and Science under the National Research Programme “Young scientists and postdoctoral students”, approved by DCM # 577 / 17.08.2018”.

REFERENCES

1. Condon, N., Klemick, H., Wolverton, A., *Food Policy*, **51**, (2015), p. 63
2. European Commission, n.a. Biofuels, Energy. European Commission
3. van Ree, R., van Zeeland, A. *Bioenergy, I.E.A.*, (2014), Task **42**
4. EL, (2009) What Is a Biorefinery? *Biomass Research. NREL*
5. Banerjee, S., Mudliar, S., Sen, R., Giri, B., Satpute, D., Chakrabarti, T., Pandey, R., *Biofuels Bioprod. Bior.* **4**, (2010), p. 77
6. Guo, M., Song, W., Buhain, J., *Renewable Sustainable Energy Rev.* **42**, (2015), p. 712
7. Parajuli, R., Dalgaard, T., Jørgensen, U., Adamsen, A.P.S., Knudsen, M.T., Birkved, M., Gylling, M., Schjørring, J.K., *Renewable Sustainable Energy Rev.* **43**, (2015), p. 244
8. Bautista, S., Narvaez, P., Camargo, M., Chery, O., Morel, L., *Ecol. Indicat.* **60**, (2016), p. 84
9. Perez A., Rincon P., Camargo M., Marchant M., *J.of Cl. Prod.*, **223**, (2019), p. 189

PREPARATION AND STRUCTURE OF PAN/CLAY NANOCOMPOSITE MEMBRANES

Milena Miteva, Dimitrina Kiryakova, Stoyko Petrov
E-mail: rmkpetrovi@abv.bg

ABSTRACT

Nanomer 1.28E was used in different amounts as nanoparticles dispersed in 17 wt.% solution polyacrylonitrile (PAN) with dimethylformamide (DMF) and dimethylsulfoxide (DMSO). From the respective solutions nanocomposite membranes were formed by the phase inversion method. The composition and morphology of the fabricated membranes were analyzed by FT-IR, SEM. The permeability and rejection of modified membranes were investigated using water and albumin as calibrants. At the optimal concentration of 1.5 wt.% in the polymer solution, the membrane rejection reaches 70% at permeability 137 l/m²h.

Key words: polyacrylonitrile, nanoparticles, nanocomposite

INTRODUCTION

Membrane technology has an effective industrial application in the food, chemical, textile, and paper industries, ammunitions production, etc [1-4]. Membrane processes are used both for separation of target components from the product mixtures and removal of organic and inorganic contaminants. According to the type of membrane process, a wide range of membrane materials are used: ceramic: silica, alumina, titania, etc., polymeric: polyvinylidene fluoride (PVDF), polyamide (PA), polyether sulfone (PES), polysulfone (PSF), etc. and metallic: palladium, silver, etc. [5-7].

Polymer nanocomposite research, including applications, has been carried out with a wide range of nanofillers, such as layered silicates (clays), carbon nanotubes/nanofibers, colloidal oxides, double-layered hydroxides, quantum dots, nanocrystalline metals and so on.

Polymeric nanocomposite membranes are fabricated using technologies, such as phase inversion, interfacial polymerization, physical coating, electrospinning and cross-linking, self-assembly, layer-by-layer assembly, and chemical grafting [8-12].

This study aims to report the possibility of obtaining a PAN/clay nanocomposite membrane by phase inversion from a solution and characterization of the membrane structures formed.

The use of nanoparticles in polymer matrices, thus creating a nanocomposite, can yield an

optimal multi-functional material for different applications.

The organic treatment of the clay makes the normally hydrophilic montmorillonite organophilic, allowing it to the interface of many different polymer matrices, remaining as micron-sized particles and serving as a traditional filler. The clay could enhance the surface morphology, mechanical and barrier properties as well as keep other properties intact.

EXPERIMENT

The membranes were formed by dry-wet phase inversion technique from polymer solutions in a water coagulation bath. Polymer solutions of the following compositions: 17 wt% PAN and 17 wt% PAN with added Nanomer 1.28E in concentrations of 1.0 - 2.5 wt. % dissolved in DMSO and DMF product of Fluka, Germany. Polyacrylonitrile fibres obtained from the ternary copolymer poly (acrylonitrile–methylacrylate–2-acryloami-de–2-methylpropanesulphonic acid) produced by LUKOIL Neftochim Bourgas Co., Bulgaria. Nanomer 1.28E product of Sigma-Aldrich was montmorillonite clay $Al_2[(OH)_2Si_2O_5]_2 \cdot nH_2O$, surface that was modified with 25 – 30 wt.% trimethyl stearyl ammonium >99%, < 80nm.

The PAN solution was prepared at room temperature until full dissolution of the polymer. The Nanomer 1.28E containing solutions was

prepared to obtain a homogeneous dispersion of the necessary quantity at room temperature, then PAN was added until full dissolution and homogenization of the solution obtained by stirring. After filtering and deaeration, the polymer solution was cast on a calendered polyester matt attached on a glass plate. The polyester matt brand FO-2403, product of Velidon Filtren, Germany had density of 100 ± 5 g/m² and thickness 2 ± 0.1 mm. About a minute after the deposition, the solution was placed in a bath of distilled water at temperature of $25 \pm 1^\circ\text{C}$ to carry out the process of phase inversion and formation of the membrane structure. The membranes were left for half an hour in the coagulation bath, then they were thoroughly washed with water for total removal of the solvent.

The rejection ($R, \%$) and permeability ($J, \text{l/m}^2\cdot\text{h}$) of the membranes towards albumin as calibrant were measured on a laboratory module Sartorius SM-165, England. The albumin concentration was determined on a spectrometer UV/VIS UNICAM 8625, France at wavelength $\lambda = 280$ nm.

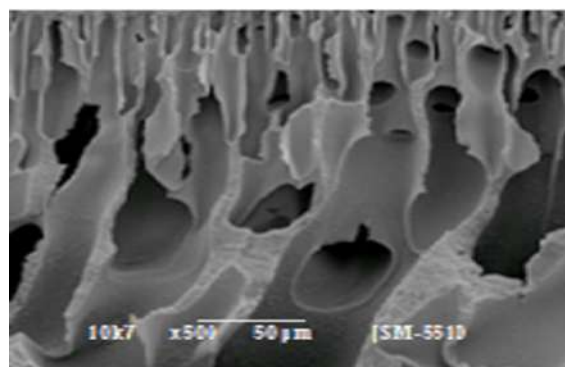
Infrared spectroscopy of the solid samples of membranes was carried out on a TENSOR 27 FT - IR spectro-photometer (Bruker, Germany).

The scanning electron microscope observations were performed on JSM-5510 apparatus, product of JEOL, Japan.

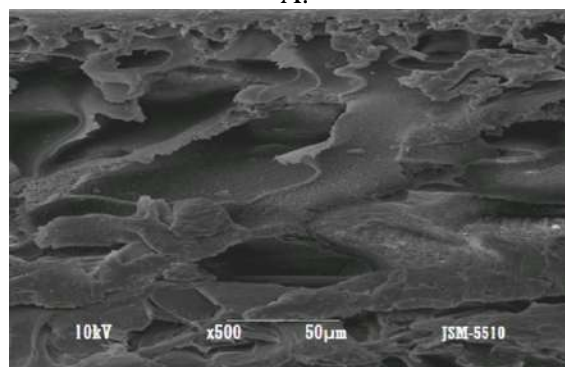
RESULTS AND DISCUSSION

The importance of Nanomer 1.28E for the membranes was studied with polymer solutions of constant PAN concentration and increasing content of Nanomer 1.28E. It was found out that nanoparticles can be used as an additive to the polymer solution with a constant concentration of PAN from 17 wt.%. This concentration was chosen on the basis of preliminary experiments carried out in the range 15 – 18 wt.% solution.

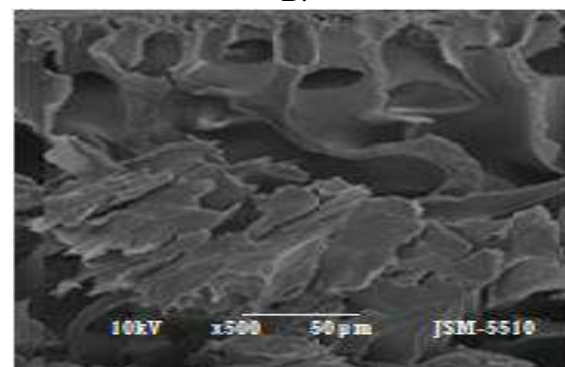
The PAN membrane and those formed from solutions containing respectively 1.0, 1.5, 2.5 wt.% nanoclay particles were investigated with SEM. The captured cross-sectional images of the membranes are presented in Fig. 1. They enabled us to find that all membranes have an asymmetrical structure. The presence of Nanomer 1.28E in polymer solutions affected the morphology of the asymmetric structure. As the nanoparticle concentration increased, the height and density of the selective layer decreased. This affected the shape of the pore channels in this part of the membrane structure.



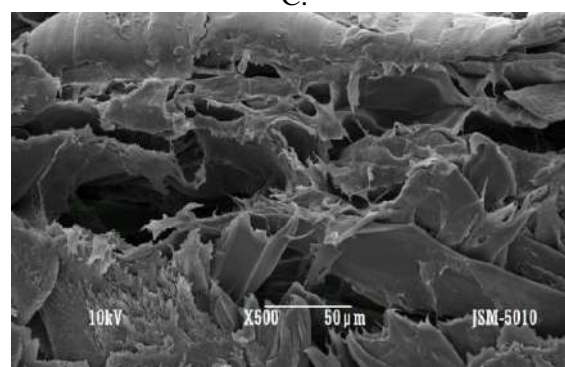
A.



B.



C.



D.

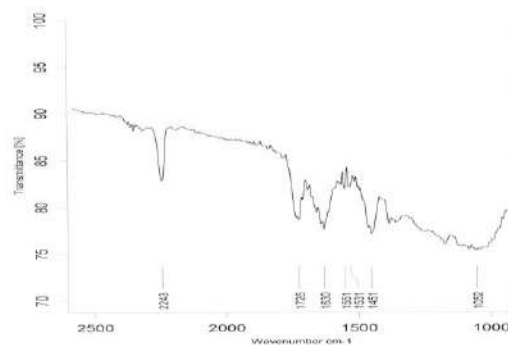
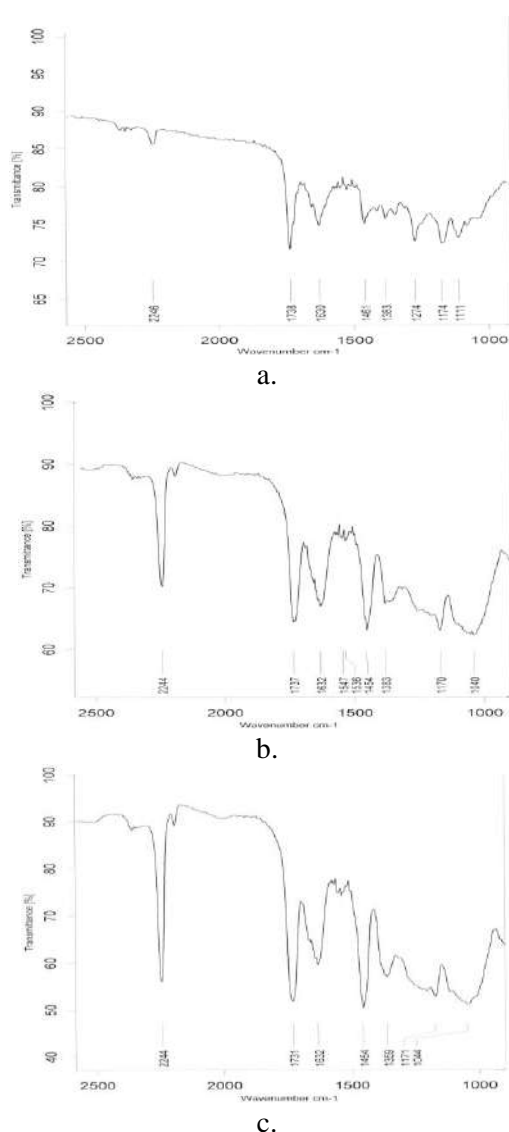
Fig. 1. SEM image of cut-off of asymmetric membranes: A - 17% PAN, B - 17% PAN/1.0% clay, C - 17% PAN/1.5% clay, D - 17% PAN/2.5 % clay.

With the formation of the macro sublayer, the pore channels are combined to varying degrees and form different macro-voids, in proportion to

the increase in the concentration of nanoclay. This is especially noticeable for membranes formed from a solution containing 1.0 and 2.5 wt.% (Fig. 1 B, D).

The morphological differences in the structure are the result of the different conditions under which the phase inversion takes place. These differences are caused by the different amounts of nano additive.

The retention of the nanoparticles in the structure of membranes and their participation in the construction of the structure were studied and proven by infrared spectroscopy. Solid samples of the membranes under consideration were investigated and the corresponding spectra are presented in Fig. 2.



d.
Fig. 2. FT-IR spectra of the membranes: a-17% PAN, b-17% PAN/1% clay, c-17% PAN/1.5% clay, d-17% PAN/2.5% clay

The spectral data from samples of membranes containing Nanomer 1,28E (Fig. 2 b, c, d) reflected its presence by registering a characteristic peak in the interval $1100-1000\text{ cm}^{-1}$ corresponding to $\nu(\text{Si-O-Si})$ [13]. In comparison, there was no such peak in the spectral band of the PAN membrane (Fig. 2 a). This difference identifies the physical presence of the nanoclay in the membranes and shows that it is not affected by the non-solvent in the phase inversion process. It is also clear from the spectral analysis that this presence influenced $\nu(\text{C}\equiv\text{N})$ at 2244 cm^{-1} in PAN.

The results obtained from the study of the permeability and selectivity of the polymer membranes carried out at 0.3 MPa immediately after their formation and preparation for the experiments are shown in Table 1 and Fig. 3.

The membranes had permeabilities in a wide range, with permeability for water from $68\text{ l/m}^2\cdot\text{h}$ at the PAN membrane to $137\text{ l/m}^2\cdot\text{h}$ at the PAN/clay membrane. Different amounts of Nanomer 1.28E are integrated differently in the respective structures and this affects the values of water permeability.

Table 1. Permeability of membranes measured at 0.3 MPa

Membranes	$J_{\text{H}_2\text{O}}, \text{l/m}^2\cdot\text{h}$	$J_{\text{alb}}, \text{l/m}^2\cdot\text{h}$
17% PAN	68	43
17% PAN/1% clay	75	30
17% PAN/1.5% clay	137	40
17% PAN/2.5% clay	99	37

With the increase of nanoparticle concentration from 1.0 wt.% to 1.5 wt.% the permeability values increase, for water from 75 l/m²h to 137 l/m²h and for albumin from 30 l/m²h to 40 l/m²h., but at a concentration of 2.5 wt.% decrease for water to 99 l/m²h and for albumin to 37 l/m²h. Different amounts of Nanomer 1.28E are integrated to a varying degree into the respective structures and this affects permeability values. The explanation of these changes is that the concentration of 2.5 wt.% is the limit value compatible with the concentration of the polymer to obtain an effective membrane structure.–We assume that this reduces the homogeneous dispersion of the nanoparticles during the phase inversion. These results are fully consistent with the structural features shown in Fig. 2.

The values of rejection are influenced similarly by the structure of the membranes containing Nanomer 1.28E. For membranes containing 1.0 wt.% and 2.5 wt.%, respectively, retention is reduced to 55% and 57% compared to the PAN membrane (Fig. 3).

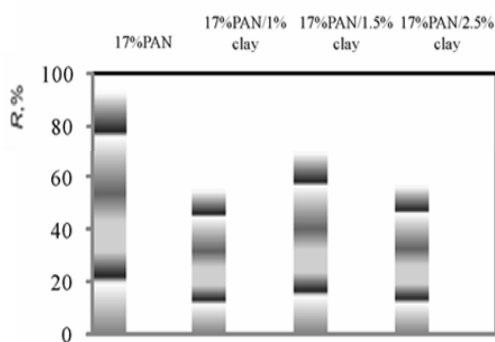


Fig. 3. Rejection of the membranes at 0.3MPa

The changes in structural morphology resulting from nanoparticle distribution are optimal at a concentration of 1.5 wt.% as membrane retention reaches 70% at permeability 137 l/m²h.

CONCLUSIONS

Nanomer 1.28E is available in all membranes as a participant in the building of

polyacrylonitrile nanocomposite.

Nanomer 1.28E influences the structure of the membranes and the modifying effect on the membranes morphological characteristics is in accordance with the amount of the nanoparticles, and the optimal amount found is 1.5 wt.%.

PAN/clay nanocomposite membranes were found to have optimal permeability of 137 l/m²h and rejection of 70% at participation of 1.5 wt.% Nanomer 1.28E in the polymer solution.

REFERENCES

1. Kirby, R.M., Bartram, J., Carr, R., *Food Control*, 14, (2003), p. 283.
2. Fersi, C., Dhahbi, M., *Desalination*, 222, (2008), p.263.
3. McClelland, J.D., Horowitz, J.K., *Land Econ.*, (1999), p. 220.
4. Hu, X.C., Andrews, D.Q., A.B. Lindstrom, T.A. Bruton, L.A. Schaidler, P. Grandjean, R. Lohmann, C.C. Carignan, A. Blum, S.A. Balan, *Environ. Sci. Technol. Lett.*, 3, (2016), p.344.
5. Yasuda, H., Tsai, J., *J. Appl. Polym. Sci.*, 18, (1974), p.805.
6. Meng, F., Chae, S.-R., Drews, A., Kraume, M., Shin, H.-S., Yang, F., *Water Res.*, 43, (2009), p.1489.
7. Pendergast, M.M., Hoek, E.M., *Energy Environ. Sci.*, 4, (2011), p.1946.
8. Hofs B., Ogier J., Vries D., Beerendonk, E., F., Cornelissen, E.R., *Sep. Purif. Technol.*, 79, (2011), p. 365.
9. Lee, A., Elam, J.W., Darling, S.B., *Environ. Sci. Water Res. Technol.*, 2, (2016), p.17.
10. Shaffer, D.L., Werber, J.R., Jaramillo, Lin, H. S., Elimelech, M., *Desalination*, 356, (2015), p.271.
11. Hoek, E.M.V, Ghosh, A.K., Huang, X., Liong, M., Zink, J.I., *Desalination*, 283, (2011), p.89.
12. Kim, E.-S., Hwang, G., Gamal El-Din, M., Liu, Y., *J. Membr. Sci.*, 394–395, (2012), p.37
13. Lai, J.Ch. H., Rahman, R.Md., Hamdan, S., *Int. J. Polym. Sci.*, 2015, (2015), p.8.

APPLICATION OF A MODEL FOR ASSESSMENT AND ANALYSIS OF RADIOACTIVE ACTIVITY

Plamena Atanasova, Sabina Nedkova

E-mail: pl.veleva@abv.bg

ABSTRACT

The study presents the application of an interactive method for assessment and analysis of radioactive activity and the radioactive situation, which is developed for the case of explosion in a nuclear power station. The interactive model is developed with MATLAB software and presents the inhaled dose of radioactivity and the dose from the external radioactivity for the time of stay in the radioactively contaminated zone.

Key words: radioactive situation

INTRODUCTION

The assessment of a radiation situation is of great importance when planning methods and tools for crisis management in the case of an accident in a nuclear power plant. This process involves solving a number of problems, analysing the results and choosing an action and a behaviour mode that guarantees minimal losses. Due to the seriousness of this situation, knowledge of its nature and mastery are part of the training of students studying "Technical safety and disaster protection".

EXPERIMENTAL

Training for determination of the radiation situation as a result of an accident in a nuclear power plant (NPP) involves the extent of radioactive contamination by radioactive substances in the area and the atmosphere, which have a negative impact on human health and the sustainable operation on the sites. The shape of the radioactive contamination zones (extremely dangerous and dangerous ones) is represented by isosceles triangles. Depending on the incorporated dose values, two radioactive contamination zones are distinguished and presented on a map [1].

The contamination zones are determined after choosing their length L and width B . The radiation situation also includes: estimation of the time for the radiation cloud to reach the object at a distance x_1 , as well determination of the radioactive doses received through inhalation and from external exposure when residing in a radionuclide-contaminated area. For the determination

of these doses an interactive model is used, developed with MATLAB software, based on the methodology used for modelling a passive system of a car [2]. The model is applied as part of a practical exercise in the Technical safety and disaster protection course taken by fourth- and third-year students from the Faculty of Technological Sciences of Prof. Dr Asen Zlatarov University, Burgas.

RESULTS AND DISCUSSION

1. Contamination zones determination

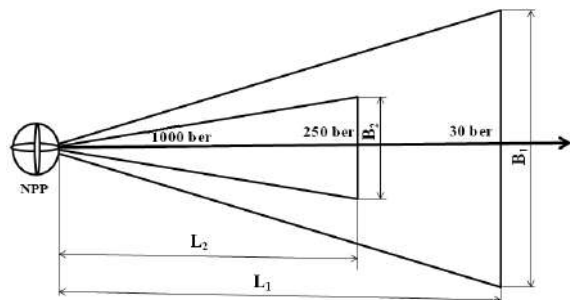


Fig.1 Hazardous radioactive contamination zone

The radioactive contamination zones are determined in accordance with the incorporated radioactivity in a living organism, measured in "ber", which is the biological equivalent of the R (roentgen) unit. In the hazardous radioactive contamination zone, the inside dose is 250 ber and at the inside border it is 30 ber, while in the extremely hazardous zone, the inside dose is 1000 ber, and along the outside border it is 250 ber, as shown in Fig. 1.

2. Evaluation and analysis of the radiation situation

For the evaluation and analyses of the radiation situation, students use the following data taken from the experimental data of a hypothetical NPP located in a map area:

2.1. Type and capacity of reactor. The type of the reactors is usually WWEP –Water energy reactor, with capacity (power – P) 1000 MW and 440 MW.

2.2. The beginning of the accident - time of the day and month. These data are very important for developing an evacuation strategy.

2.3. Coordinates of the scene of the accident – x and y, longitude and latitude, which are taken from the experiment map.

2.4. Distance of an industrial unit, marked with x_i and measured in kilometres, to the reactor.

2.5. Coefficient of the reactor – Cr (1). When the power of the reactor is 1000 MW, Cr is 1 and, when 440 MW, it is 0.44.

$$Cr = \frac{P}{1000} \quad (1)$$

2.6. Coefficient of protection Cp (2)

$$Cp = 2^{\frac{z}{d}} \quad (2)$$

2.7 Resistance to atmospheric conditions. This includes horizontal stability, with a) wind speed v in m/s and b) wind direction in azimuth. This information is needed for determination of the direction where the radioactive cloud could start to move taken by the wind. For determination of this direction a coordinate system with degrees and directions is used (Fig. 2).

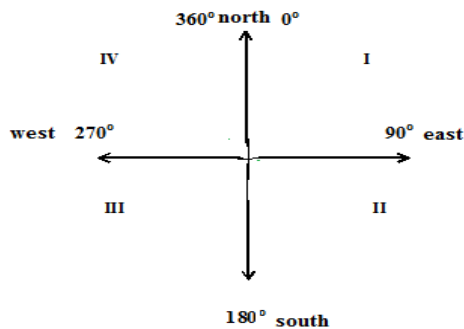


Fig. 2. Coordinate system for wind direction

The coordination system describes four quadrants. If the wind direction is at the 0-90 geographical degrees range, it has northeast direction, at the 90-180 geographical degrees range, it has southeast direction, at the 180-270 geographical degrees range, it has southwest direction and

at the 270-360 geographical degrees range, a northwest direction.

Vertical stability is described with two temperatures: t_1 – measured at 50 cm. from the ground and t_2 – measured at 200 cm. from the ground. If the two temperatures are equal, $t_1 = t_2 \rightarrow$ isothermy, and if they are different $t_1 > t_2 \rightarrow$ convection and $t_1 < t_2 \rightarrow$ inversion. The worst case scenario is usually considered, when the vertical stability of the atmosphere is inversion. This situation is static and because of the lack of air movement, the contamination from the radioactive contaminants can last longer.

3. Practical assessment of the radiation situation

For determination of L_1 and L_2 (lengths) and B_1 and B_2 (widths), as shown in Fig. 2, a special nomogram developed in the methodology is used [1]. From this nomogram it can be seen that for an incorporated zone $D_{ink.} = 30$ ber, $L_1 = 134$ km, and for an incorporated zone, $D_{ink.} = 250$ ber, $L_2 = 80$ km. Knowing the square of the triangular shapes of the zones, $S_1 = 680$ km² and $S_2 = 190$ km² and using formula (3), the two widths B_1 and B_2 are determined.

$$B = \frac{2S}{L}, \quad km \quad (3)$$

4. Determining the time when the radiation cloud will reach the object at distance x_1 .

The formula needs the distance x and the wind velocity in km/h (4)

$$\tau = \frac{x}{v} \quad (4)$$

5. Determination of doses of radioactive contamination.

For determination of the Inhalation zone $D_{inh.}$ formula (5) is used, and an interactive MATLAB model for its assessment, based on D estimated (estimated dose of radiation, which corresponds to a distance) from the nomogram used above and the coefficient of the reactor – Cr , is developed.

$$D_{inh.} = \frac{Dest. Cr}{2,7} ber \quad (5)$$

The MATLAB interactive model allows students to determine the inhalation dose, giving different values for the estimated dose, corresponding to a distance from the reactor (in km)

and for the coefficient of the reactor. In Fig. 3, the inhalation dose is determined for $Cr = 1$ (Kp in the figure). In Fig. 4, the inhalation dose is determined for $Cr = 0.44$. Both estimated doses are 1500 ber, because they are determined for an object which is located at a distance of 30 km from the reactor.

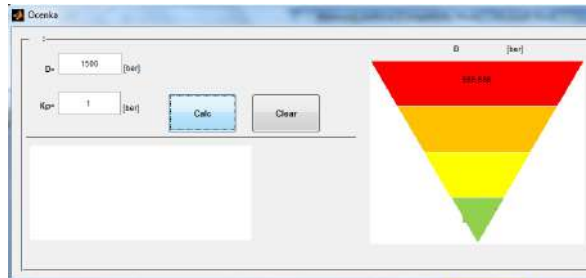


Fig. 3 Inhalation zone for $Cr=1$

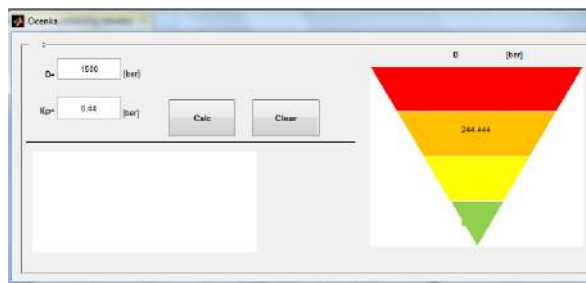


Fig. 4 Inhalation zone for $Cr=0,44$

It can be seen from the figures that people staying in a place which is located at a distance of 30 km from the reactor, with estimated dose of 1500 ber of the environment, would receive serious doses of radiation from inhalation of the contaminated air. If the problematic reactor has a capacity of 1000 MW, and $Cr=1$ (Fig. 3), the dose would lead to the development of the most severe form of radiation sickness having a value of 555, 556 bers. This is why, in the coloured code it is shown in the red, highly dangerous zone. The people located on the same site at the same distance from a less powerful reactor 440 MW, with $Cr=0.44$, would receive a dose from the inhalation of contaminated air which is of average danger and, that is why, it falls in the orange zone, the one of danger. It is important to mention, that in the case of accident, the person reactive radioactive contamination received in all three ways forms the so-called incorporated dose: the contamination coming from the penetrating (external) radiation (point 6) in the radioactive area; the contamination from the inhaled air; and the radiation received from the use of contaminated water and food.

6. Determination of the absorbed dose of external radiation when residing in a radionuclide-contaminated area.

The used formula for the development of the MATLAB model includes data for:

P_{st} - the exposure power of the area at the beginning (start) of the radiation accident, R/h (P_H in the picture);

P_{end} - exposure power at the end of exposure, R/h (P_{Kp} in the picture);

C_p - coefficient of protection (K in the picture);

t - duration of exposure, h.

$$D = \frac{P_{st} + P_{end}}{2 C_p} \cdot t \cdot Cr \quad (6)$$

As can be seen from Fig. 5 and 6, for an accident with a reactor with 440 MW capacity and coefficient of reactor 0.44, we have described two situations.

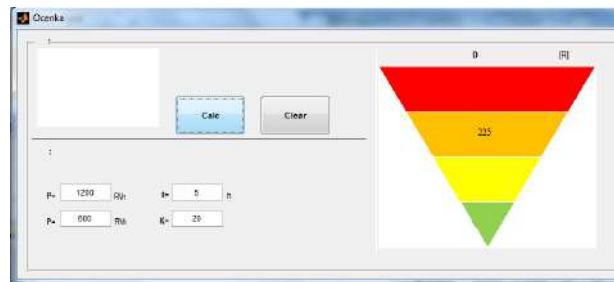


Fig. 5. Absorbed dose from ext. radiation, for $Kp=20$

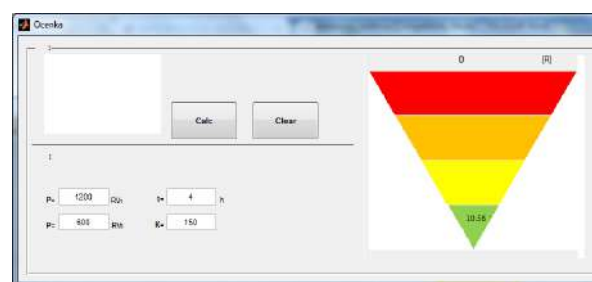


Fig. 6. Absorbed dose from ext. radiation, for $Kp=150$

In Fig. 5, the people staying at the same distance of 30 km from the crushed reactor in a shelter (a light structure building, such as a shed, with quite low coefficient of protection 20), for 5 hours since the accident would receive 225 R of radiation, which is an average danger dose, leading to a second degree of radiation sickness, which is curable.

The same people at the same distance, but staying in more stable (yet not massive) building, with coefficient of protection of 150 (e.g. a hut) for 4 hours would receive the not dangerous dose of 10.56 R. In the case of radiation situation, any shelter can give protection from the external radiation, but more stable buildings have a higher coefficient of protection and are better at stopping this radiation.

AKNOWLEDMENT

This work was supported by the fund for inner university research projects, NIH 416/2018.

REFERENCES

1. Dragolov, D. *Zashtita na naselenieto ot avarii, prirodni bedstviya i opazvane na okolnata sreda*, UI, "Sv.sv Kiril i Metodii", Veliko Tarnovo, 2011.
2. L. Staneva, Yulian Petrov, Stancho Edrev. Modelirane na pasivna sistema na chetvart model na avtomobil s matlab vyv vryzka sys seminarni uprajnenia po teoriya na avtomobila, 2015, *Industrialni technoogii*, Tom. 2 (1), Burgas, 2015, v.XXXVI

CRISIS MANAGEMENT AND ITS RELATION WITH THE ANXIETY STATE OF PEOPLE WORKING IN THE CHEMICAL INDUSTRY

Sabina Nedkova, Plamena Atanasova
E-mail: sabina_nedkova@abv.bg

ABSTRACT

The study presents the results of the anxiety level as one of the pillars of emotional resilience, crucial for crisis management in the chemical industry. As a complex activity, crisis management combines diverse actions: identification of the risk, a characterization of possible consequences, coordination and organization of the necessary crisis response forces. In dealing with the prevention and management of the actions of crisis management, people have to plan their activities on the basis of their knowledge and skills, but their emotional resilience will be decisive for their right and proper way of application.

Key words: crisis management, anxiety level

INTRODUCTION

Anxiety is a major indicator of emotional resilience as a feeling associated with experiencing insecurity, helplessness and unbalance, accompanied by negative emotions caused by the inability to satisfy a subject's need. Its measurement is particularly important as it is largely determinant of the subject's behaviour in a given situation, especially in the chemical industry, where the risk zones are specific and the probability and severity of the critical events have high values. In this industry a crisis event requires diverse actions and serious work: identification of the risk, a characterization of the possible consequences, and coordination and organization of the necessary crisis response forces. In dealing with the prevention and management of crisis management actions, people have to plan their activities, based on their knowledge and skills, but their emotional resilience will be decisive for their right and proper way of application.

EXPERIMENT

The following study shows the application of the State-Trait anxiety inventory (STAI), a test developed by Charles Spielberg, R. L. Gorsuch and R. E. Lushene as a list of questions used for assessment of the two major types of anxiety: state anxiety and trait anxiety. State anxiety (S-anxiety) can be defined as fear, nervousness, discomfort, etc. and the arousal of the autonomic nervous system induced by different situations that are perceived as dangerous. This type of

anxiety refers more to how a person is feeling at the time of a perceived threat and is considered temporary. Trait anxiety (T-anxiety) can be defined as feelings of stress, worry, discomfort, etc. that one experiences on a day-to-day basis. This is usually perceived as how people feel across typical situations that everyone experiences on a daily basis [1]. The situational (state) anxiety is a dynamic mental state, which is accompanied by a subjective experience of emotions, arises in a particular situation and responds quickly as soon as the cause is resolved. The state of situational anxiety arises as an emotional response to a stressful situation and can vary in intensity and dynamics over time. It is associated with nervousness, tension and feelings of undetermined threat, danger and frustration. Personal anxiety is an individual characteristic that reflects a person's degree of predisposition to anxiety, or to emotional negative reactions to different life situations which carry threats to his/her self. As a predisposition, personal anxiety is activated to perceive certain incentives which are assessed by the person as dangerous and related to specific situations of threat to his/her prestige and self-esteem.

STAI is applied to three groups of responders, who self-assessed themselves. The first group is university students taking a course related to the chemical industry, the second group is people actively involved in the process of management of risk and crisis situations in the chemical industries as workers, and the third group is people also working in the chemical industry, but in the administrative sector. The difference between the

three groups of people is in the level of their engagement in the process of solving problems as part of the crisis management process. The second and the third groups are chosen because they work in the chemical industry, but have different tasks and responsibilities in case of crisis and the implementation of crisis management action. Despite their different level of engagement, these two groups feel that anxiety is a key factor in making decisions in their everyday activity. The choice of the people in the first group is related to the thesis that education affects the indicators: positive daily functioning; positive self-esteem and positive expectations for the future. Individuals with good school (university) performance are more likely to replace negative thoughts with positive ones than those with average and poor one performance [2]. This principle in perception of the reality would be of help in their future realization in the chemical industry, where they will have to take active part in the process of crisis management.

Spielberger's self-rating scale includes 40 judgment questions, 20 of which are designed to assess the level of situational anxiety (while answering the question "How do I feel at this moment?") and 20 to assess the level of personal anxiety (while answering the question "How do I feel usually?"). For S-anxiety or assessing the current situation the following answers are used: not at all; somewhat; moderately so, and very much so. For assessing T-Anxiety or how the responder feels in general, the following answers are used: almost never, sometimes, often, and almost always.

Each STAI item is given a weighted score of 1 to 4. A rating of 4 (maximum rate) for each question indicates the presence of a high level of anxiety for ten S-Anxiety items and eleven T-Anxiety items (e.g., "I feel frightened," "I feel upset"). A high rating indicates the absence of anxiety for the remaining ten S-Anxiety items and nine T-Anxiety items (e.g., "I feel calm," "I feel relaxed"). The scoring weights for the anxiety-present items are the same as the blackened numbers on the test form. The scoring weights for the anxiety-absent items are reversed, i.e., responses marked 1, 2, 3, or 4 are scored 4, 3, 2, or 1, respectively. The anxiety-absent items for which the scoring weights are reversed on the S-Anxiety and T-Anxiety scales are: S-Anxiety: 1, 2, 5, 8, 10, 11, 15, 16, 19, 20 and T-Anxiety: 21, 23, 26, 27, 30, 33, 34, 36 and 39. To obtain scores for the S-Anxiety and T-Anxiety scales, the weighted scores for the twenty items that

make up each scale are added, taking into account the fact that the scores are reversed for the above items. Scores for both the S-Anxiety and the T-Anxiety scales can vary from a minimum of 20 to a maximum of 80 [3].

RESULTS AND DISCUSSION

The three groups of people are asked to assess themselves by answering the 40 items of the STAI test, choosing from four types of answers. Following the answering score algorithm, the score for T and S anxiety is obtained, after which each result is divided by 20. In assessing the obtained results the following list of points is used:

Points range:	Level of anxiety
3.5 - 4.0 points	very high anxiety
3.0 - 3.4 points	high anxiety
2.0 - 2.9 points	average anxiety
1.5 - 1.9 points	low anxiety
0.0 - 1.4 points	very low anxiety

The results (presented in Fig. 1 and Table 1) in assessing the Situational anxiety (S-anxiety) show that 67% of the responders have low levels of this type of anxiety, which makes them people who perceive the current situation in a reasonable and calm manner and are internally stable as a behavioural response to certain life situations.

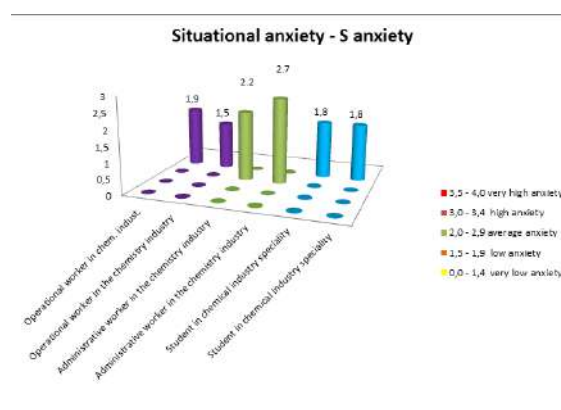


Fig. 1. Scores of Situational anxiety (S anxiety)

These 67% are the people from the first and the second group of responders, students and employees actively involved in the activities related to the chemical industry. For the first group of people, with scores 1.5 and 1.9 these results can be explained by the fact that they are still not practically implementing their knowledge and they do not have so many opportunities for using it in real situations. This might

also be related to their lack of practical experience, but presence of theoretical one. The low level of S-anxiety in the group of people working actively in the chemical industry can be explained by their professional experience and the skills they have gained at work, which make them feel safe and confident while dealing with their everyday tasks. An interesting fact is that both groups are in the age range of 20 to 30, that is relatively young people, which can be another reason for their low level of anxiety provoked by a situation, because they might not feel engaged enough or motivated enough to take active part in dealing with a situation. The administrative workers have average levels of S-anxiety. They are people aged 45-47 on average, which means that they have relatively long experience in a field where their duties often require following time schedules and dealing with deadlines in a high stressful environment, such as the chemical industry.

Table 1. S-anxiety results, information

Initials	Occupation	Age,gender	Result
D.M	Worker	30,male	1,9-low
S.D	Worker	30, male	1,5 -low
K.D	Adm.wor.	45,female	2,2 -aver.
L.D	Adm.wor.	47, female	2,7 -aver.
I.G	Student	20, female	1,8 -low
S.Y	Student	20, female	1,8-low

The scores for Personal anxiety are listed in Table 2 and are shown in Fig. 2, from which can be seen that all respondents have average levels of personal anxiety. In general, this can be interpreted as an average disposition to emotional negative reactions in different situations which carry a threat. These scores describe rather confident people, who respond to stressful and hectic situations of everyday life in a normal way.

As an individual characteristic, this reflects a person's degree of predisposition to anxiety or to emotionally negative reactions to different life situations carrying some threat. Personal anxiety is related to the way of perceiving certain stimuli which are assessed by the person as dangerous.

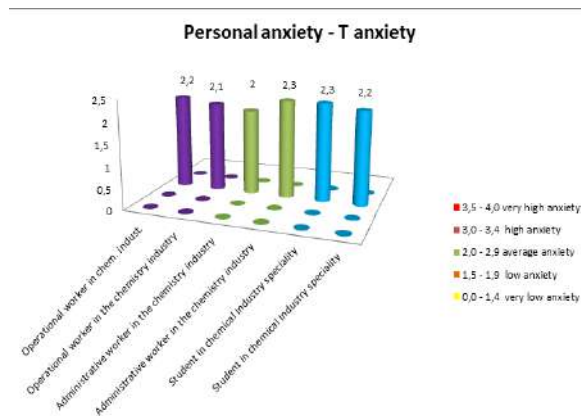


Fig. 2. Scores of Personal anxiety (T anxiety)

Table 2. T-anxiety results, information

Initials	Occupation	Age	Result
D.M	Worker	30,male	2,2- aver.
S.D	Worker	30, male	2,1 - aver.
K.D	Adm.wor.	45,female	2,0 -aver.
L.D	Adm.wor.	47, female	2,3 -aver.
I.G	Student	20, female	2,3 aver.
S.Y	Student	20, female	2,2-aver.

CONCLUSIONS

Anxiety is a major indicator of emotional resilience as a feeling associated with experiencing insecurity and helplessness, a state of inner anxiety and unbalance accompanied by negative emotions caused by the inability to satisfy a subject's need. This condition is particularly important especially in the case of crisis management in the chemical industry, as it is largely determinative of the subject's behaviour in a critical situation. In case of these situations, the behaviour is a result of signals coming from the environment (temperature, air pressure, humidity, odour, presence of chemicals and materials, etc.), which are assessed by the knowledge and skills that the person has, and signals coming from the person (inner signals) related to his personal characteristics. The proper anxiety level, both personal and state, is of high importance for the right perception and interpretation of the two type of signals to be used in the process of planning, organizing and carrying out of crisis management activities.

AKNOWLEDGMENT

This work was supported by the Bulgarian Ministry of Education and Science under the National Research Programme “Young scientists and postdoctoral students”, approved by DCM # 577 /17.08.2018

REFERENCES

1. Spielberger, Charles D.; Sydeman, Sumner J. (1994). "State-Trait Anxiety Inventory and State-Trait Anger Expression Inventory". In Maruish, Mark Edward (ed.). *The use of psychological testing for treatment planning and outcome assessment*. Hillsdale, NJ: Lawrence Erlbaum Associates. pp. 292–321. ISBN 978-0-8058-1162-9.
2. Koleva, N., (2019) *Cognitive-Behavioral Schemes and Their Repercussion in Anxiety Personality Education.*, ICTTE'2019, 17-18.10.2019, Yambol, Bulgaria.
3. Spielberger C. *Manual for the State-Trait Anxiety Inventory*. rev. ed. Consulting Psychologists Press; Palo Alto (CA): 1983

INTERCRITERIA ANALYSIS APPLIED TO HEALTHCARE RANKINGS

Veselina Bureva, Krassimir Atanassov, Nikolay Andreev
E-mail: vbureva@btu.bg

ABSTRACT

In the current investigation the healthcare topic is discussed. The medical and regional information is selected from websites and healthcare databases are studied. Intercriteria analysis is applied to the healthcare rankings to present the behaviour of the healthcare systems in the selected countries. The obtained results can classify the countries according to the consumer service provided by their healthcare systems.

Key words: *intercriteria analysis, healthcare, rankings*

INTRODUCTION

Healthcare is an extensive research section that includes a variety of closely specialized fields. The literature on healthcare assessment such as healthcare ratings and statistical measures is studied. In the current research work the Euro Health Consumer Indexes are investigated. The aim of healthcare rankings is to make a comparison between the European health care systems according to waiting times, outcomes and generosity. The Euro Health Consumer Index 2018 ranks the performance of the healthcare service from a consumer viewpoint. Therefore, the Index presents only the consumer information, and not medically or individually sensitive information. The quality of the data is imperfect because it depends on the way of gathering and storing. The Euro Health Consumer Index 2018 uses different types of information sources for healthcare systems in the countries. The Europe healthcare rankings contain a small number of indicators in a definite number of evaluation fields. The received combination presents how the healthcare consumer is served by the respective systems. In 2018 the Euro Health Consumer Indexes evaluate the health systems of 35 countries according 6 sub-disciplines. The countries are the following: Norway, Denmark, Belgium, Finland, Luxembourg, Sweden, Austria, Iceland, France, Germany, Portugal, Czech Republic, Estonia, United Kingdom, Slovakia, Serbia, Spain, Italy, Slovenia, Ireland, Montenegro, Croatia, North Macedonia, Cyprus, Malta,

Lithuania, Greece, Latvia, Bulgaria, Poland, Hungary, Romania, Albania [9]. The sub-disciplines in the Euro Health Consumer Index are:

- Patient rights and information;
- Accessibility (waiting times for treatment);
- Outcomes;
- Range and reach of services;
- Prevention;
- Pharmaceuticals.

Each sub-discipline is calculated from several indicators. The sub-disciplines weighted scores are calculated using the mix of selected indicators. In the Euro Health Consumer Index 46 healthcare indicators are selected and then structured in six sub-disciplines. These indicators are evaluated using a three-grade scale for each indicator. The scale contains green, amber and red scores, meaning respectively good, so-so and not-so-good. The scores are evaluated in the following way: green score earns 3 points, amber score is 2 points and red score or a “not available” is 1 point. For each of the sub-disciplines, the country’s score is calculated as a percentage of the maximum possible. Thereafter, the sub-discipline scores were multiplied by the weight coefficients (Table 1) and added up to receive the final country score. Therefore, an “All Green” score on the 46 indicators would yield 1000 points. “All Red” scores would give 333 points [9]. The weight coefficients used for sub-disciplines indicators calculation have the following form:

Table 1. Sub-discipline weights

<i>Sub-discipline</i>	<i>Relative weight</i>	<i>Points for a green score in each sub-discipline</i>
1. Patient rights, information and e-Health	125	12.5
2. Accessibility	225	37.5
3. Outcomes	300	33.33
4. Range and search of services	125	15.62
5. Prevention	125	17.85
6. Pharmaceuticals	100	16.67
Total sum of weights:	1000	

INTERCRITERIA ANALYSIS APPLIED TO HEALTHCARE RANKINGS

The InterCriteria analysis (ICA) theory is introduced in [5, 7]. The ICA method is based on the theories of intuitionistic fuzzy sets [2, 4, 6] and index matrices [3]. It is a useful tool for determining the degrees of dependence and non-dependence between selected objects depending on the appropriate criteria. The procedure includes comparing the pairs of values of two columns in two rows and calculating the values according to the received relations. The InterCriteria analysis produces three main categories of relationships: negative consonance, dissonance and positive consonance. On the other hand, these three categories are divided into three sub-categories: negative consonance-weak negative consonance, negative consonance and strong negative consonance, dissonance-weak dissonance, dissonance and strong dissonance, positive consonance-weak positive consonance, positive consonance and strong positive consonance. The InterCriteria analysis is applied successfully in the datasets of many scientific fields, such as evaluation of university rankings [13, 14, 19], neural networks preprocessing procedure [18], genetic algorithms [11, 17], the global competitiveness reports [8], chemical investigations [21, 22], etc. In [23] an application of the ICA approach to data connected with health-related quality of life is presented. Health-related quality of life has been used in medicine and public health as a reliable outcome measure and

a needs assessment frame [1, 10, 24]. In [20] the ICA method is applied for studying some statistical data for registered patients with oncological diseases for 2018 in Burgas. The same approach can be applied to data connected to metastatic melanoma [15, 16], diabetic foot [26, 27] and colorectal cancer [25, 28].

Table 2. InterCriteria analysis applied to healthcare rankings

<i>Type of consonance</i>	<i>Number of pairs</i>
Dissonance (D) [0,33; 0,43)	6
Strong Dissonance (SD) [0,43; 0,57)	21
Dissonance (D) [0,57; 0,67)	9
Weak Dissonance (WD) [0,67; 0,75)	80
Weak Positive Consonance (WPC) [0,75; 0,85)	108
Positive Consonance (PC) [0,85; 0,95)	293
Strong Positive Consonance (SPC) [0,95; 1]	65

In the current research InterCriteria analysis is applied over the healthcare ranking using ICraData software [12]. The relationships between the 35 countries according to 6 sub-disciplines are investigated. The results from the application of ICA over the healthcare rankings have the following form: 21 pairs of countries in strong dissonance, 15 pairs of countries in dissonance, 80 pairs of countries in weak dissonance, 108 pairs of countries in weak positive consonance, 293 pairs of countries in positive consonance and 65 pairs of countries in strong positive consonance (Table 2).

The obtained results of the InterCriteria analysis over the healthcare rankings are presented in the intuitionistic fuzzy triangle in Fig. 1. Two groups of data points are visualized with different colours. The green data points represent the pairs of countries with dependencies in their healthcare systems functioning in the way of providing services to consumers. The pink data points are the pairs of counties whose healthcare systems have no dependencies.

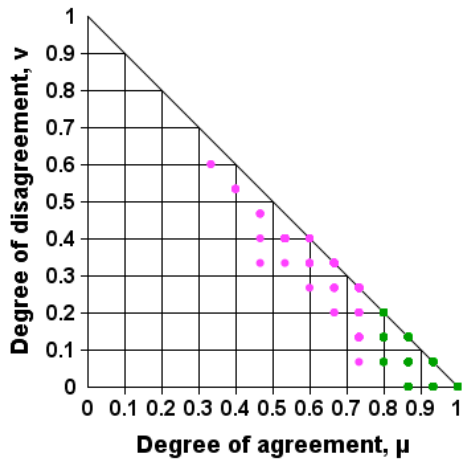


Fig. 1 InterCriteria analysis applied to healthcare rankings

RESULTS

The results from the application of InterCriteria analysis over healthcare rankings have been studied. A comparison between the countries has been made. The following outcomes have been obtained:

- The pairs of countries in weak positive consonance have similar behaviour according to the investigated sub-disciplines. These pairs of countries have similarities in the functioning of their healthcare systems.
- The pairs of countries in positive consonance have close similarities according to the investigated sub-disciplines. These pairs of countries have identical manner of functioning of their healthcare systems.
- The pairs of countries in strong positive consonance have dependencies according to the investigated sub-disciplines. The identical manner of functioning of the healthcare systems and the same consumer service are determined.
- The pairs of countries in weak dissonance, dissonance or strong dissonance are independent. The healthcare systems and consumer service of these pairs of countries are independent of each other.

The results received from the application of ICA over healthcare rankings presents the groups of countries with similar functioning of their healthcare systems. The total number of pairs of countries having similar performance of providing consumer service is 466. These pairs of countries have different degrees of dependence according to the obtained results. The conducted investigation provides the information for 116

pairs of countries that have independent behaviour of functioning of their healthcare systems.

According to the results of the InterCriteria application for the healthcare system of Bulgaria, the following outcomes are obtained:

- **Dissonance:** Ireland-Bulgaria;
- **Weak dissonance:** Sweden-Bulgaria, France-Bulgaria, United Kingdom-Bulgaria, Malta-Bulgaria;
- **Weak positive consonance:** Netherlands-Bulgaria, Belgium-Bulgaria, Finland-Bulgaria, Luxembourg-Bulgaria, Slovenia-Bulgaria, Montenegro-Bulgaria;
- **Positive consonance:** Switzerland-Bulgaria, Norway-Bulgaria, Denmark-Bulgaria, Austria-Bulgaria, Iceland-Bulgaria, Germany-Bulgaria, Portugal-Bulgaria, Czech Republic-Bulgaria, Estonia-Bulgaria, Slovakia-Bulgaria, Serbia-Bulgaria, Spain-Bulgaria, Italy-Bulgaria, Croatia-Bulgaria, Cyprus-Bulgaria, Lithuania-Bulgaria, Greece-Bulgaria, Latvia-Bulgaria, Bulgaria-Hungary;
- **Strong positive consonance:** North Macedonia-Bulgaria, Bulgaria-Romania.

The consumer service of the healthcare system of Bulgaria is similar to the consumer service of the healthcare systems of North Macedonia and Romania. The InterCriteria analysis results presented strong dependencies between the healthcare systems of Bulgaria, Romania and North Macedonia. The obtained results present dependencies of the consumer service of the healthcare system of Bulgaria and the consumer service of healthcare systems of Switzerland, Norway, Denmark, Austria, Iceland, Germany, Portugal, Czech Republic, Estonia, Slovakia, Serbia, Spain, Italy, Croatia, Cyprus, Lithuania, Greece, Latvia and Hungary. These healthcare systems have similar trends of work. Weak dependencies are determined for the consumer service of the healthcare systems of Bulgaria and Netherlands, Belgium, Finland, Luxembourg, Slovenia and Montenegro. The processes of these healthcare systems are similar but their functioning is not the same. The countries whose healthcare systems are independent with regards to the consumer service of the healthcare system of Bulgaria are Ireland, Sweden, France, United Kingdom and Malta.

CONCLUSION

In the current research work the authors have used ICA to reveal some hidden patterns in

healthcare rankings. The InterCriteria analysis is applied to the Euro Health Consumer Index to discover possible dependencies between the healthcare systems of the countries in Europe. In future research the authors aim to trace the current tendency by analyzing the healthcare ranking for the past five years (2014-2018). InterCriteria analysis will be applied to the healthcare rankings to determine the possible relationships between the indicators of the sub-disciplines.

ACKNOWLEDGMENT

This work is partially supported by the Bulgarian National Science Fund under Grant Ref. No. KP-06-N22/1/2018 "Theoretical research and applications of InterCriteria Analysis" for section 3 and "Intelligent Instruments for Knowledge Discovering and Processing" (No. NIH-418/2018) for section 2.

REFERENCES

- Atanasov A., E. Lefterov, V. Vasilev, A. Kehayov, M. Savov, V. Penchev, B. Dashkov, *Evaluation of the quality of life in patients with various abdominal anastomoses in case of colon carcinoma*, Regional Scientific Conference, ISBN 978 -954-397-023-0, Svilengrad, 17 - 19.11.2011, 110-112.
- Atanassov, K. *On Intuitionistic Fuzzy Sets Theory*, Springer, Berlin, 2012.
- Atanassov, K. *Index Matrices Towards an Augmented Matrix Calculus*. Studies in Computational Intelligence Series, Vol. 573, Springer, Cham, 2014.
- Atanassov, K., Atanassova, V., Gluhchev, G. *InterCriteria Analysis: Ideas and problems*, Notes on Intuitionistic Fuzzy Sets, 21(1), 2015, 81–88.
- Atanassov, K., Mavrov, D., Atanassova, V. *InterCriteria Decision Making: A New Approach for Multicriteria Decision Making*, Based on Index Matrices and Intuitionistic Fuzzy Sets. Issues in Intuitionistic Fuzzy Sets and Generalized Nets, 11, 2014, p. 1–8.
- Atanassov, K., Szmidt, E., Kacprzyk, J. *On intuitionistic fuzzy pairs*, Notes on Intuitionistic Fuzzy Sets, 19(3), 2013, p. 1–13.
- Atanassova V., L. Doukovska, A. Michalíková, and I. Radeva *Intercriteria analysis: from pairs to triples*, Notes on Intuitionistic Fuzzy Sets, vol. 22, no. 5, 2016, p. 98–110.
- Atanassova, V., L. Doukovska, D. Mavrov, K. Atanassov *InterCriteria Decision Making Approach to EU Member States Competitiveness Analysis: Temporal and Threshold Analysis.*, In P. Angelov et al. (eds), Intelligent Systems'2014, Advances in Intelligent Systems and Computing 322, 2014, p. 95–106.
- Björnberg A., A. Phang, *Euro Health Consumer Index 2018 Report*, Health Consumer Powerhouse, 2019, ISBN 978-91-980687-5-7.
- Ducheva D., R. Paskaleva, I. Popov, *The role of kinesiotherapy in improving motor activity and quality of life in elderly people, 65 years* Medical College - Stara Zagora, Collection of Papers, ISBN 978-954-9443-63-9, October 2012, p. 57-63.
- Fidanova, S., O. Roeva, *Comparison of Different Metaheuristic Algorithms based on InterCriteria Analysis*, Journal of Computational and Applied Mathematics, Available online 7 August 2017, <https://doi.org/10.1016/j.cam.2017.07.028> IF = 1.357.
- Ikonomov N., P. Vassilev, O. Roeva, *ICrA-Data – Software for InterCriteria Analysis*, *INT.J.BIOAUTOMATION*, 22(1), 2018, p.1-10.
- Krawczak, M., V. Bureva, E. Sotirova, E. Szmidt. *Application of the InterCriteria Decision Making Method to Universities Ranking*, In: Novel Developments in Uncertainty Representation and Processing, Vol. 401, Advances in Intelligent Systems and Computing, Springer, 2016, p.365-372.
- Parvathi R., V. Atanassova, L. Doukovska, C. Yuvapriya, K. Indhurekha *InterCriteria Analysis of rankings of Indian universities*, ICIFSS, 8–10 January 2018, Erode, Tamil Nadu, India Notes on Intuitionistic Fuzzy Sets Print ISSN 1310–4926, Online ISSN 2367–8283 Vol. 24, No. 1, 2018, p. 99–109.
- Popov I., R. Zheliazkov, D. Ivanova, G. Shomov, *Metastatic Melanoma and Kidneys*, Nephrology, dialysis and transplantation, ISSN 1312-5257, 21 (3), 2015, 21-24.
- Popov I., R. Zheliazkov, D. Ivanova, G. Shomov, *Metastatic Melanoma – Kidneys, Myocard, Lungs and Liver, Spleen*. Clinical case. Nephrology, dialysis and transplantation, ISSN 1312-5257, 21, (2), 2015, 9.
- Roeva O., P. Vassilev, S. Fidanova, M. Paprzycki, *InterCriteria Analysis of Genetic Algorithms Performance*, Recent Advances in Computational Optimization, Springer, 2016.
- Sotirov, S., V. Atanassova, E. Sotirova, V. Bureva, D. Mavrov. (2015) *Application of the*

- Intuitionistic Fuzzy InterCriteria Analysis Method to a Neural Network Preprocessing Procedure*. Proc. of 16th World Congress of the International Fuzzy Systems Association (IFSA), 9th Conference of the European Society for Fuzzy Logic and Technology (EUSFLAT), 30.06-03.07.2015, Gijon, Spain, p.1559–1564.
19. Sotirova E., Bureva V., Chountas P., Krawczak M. *An application of intercriteria decision making method to the rankings of universities in the United Kingdom*, Notes on Intuitionistic Fuzzy Sets, 22(3), 2016, p. 112–119.
 20. Sotirova, E., Y. Petrova, H. Bozov, *InterCriteria Analysis of oncological data of the patients for the city of Burgas*, Notes on Intuitionistic Fuzzy Sets, Vol. 25, No. 2, 2019, p. 96–103.
 21. Stratiev, D., Shishkova, I., Nedelchev, A., Kirilov, K., Nikolaychuk, E., Ivanov, A., Sharafutdinov, I., Veli, A., Mitkova, M., Tsaneva, T., Petkova, N., Sharpe, R., Yordanov, D., Belchev, Z., Nenov, S., Rudnev, N., Atanassova, V., Sotirova, E., Sotirov, S., Atanassov, K. *Investigation of relationships between petroleum properties and their impact on crude oil compatibility*, Energy Fuels, 29(12), 2015, p. 7836–7854.
 22. Stratiev, D., Sotirov, S., Shishkova, I., Nedelchev, A., Sharafutdinov, I., Veli, A., Mitkova, M., Yordanov, D., Sotirova, E., Atanassova, V., Atanassov, K., Stratiev, D., Rudnev, N., Ribagin, S. *Investigation of relationships between bulk properties and fraction properties of crude oils by application of the intercriteria analysis*, Petroleum Science and Technology, Vol. 34 (13), 2016 p. 1113–1120.
 23. Vankova D., E. Sotirova, V. Bureva, *An application of the InterCriteria Analysis approach to health-related quality of life*, Notes on Intuitionistic Fuzzy Sets, 21(5), 2015, 40–48.
 24. Vankova, D., Kerekovska, A., Kostadinova, T., Usheva, N., *Health-related Quality of Life in the Community. Assessing the Socio-Economic, Demographic and Behavioural Impact on Health-related Quality of Life at a Community Level: Evidence from Bulgaria*, Proceedings database, 2013,
 25. Vassilev, V. D. Tanev, T. Kavtrakov, H. Abrashev, *Our experience in surgical treatment of the complicated forms of colorectal cancer*, Trakia Journal of Sciences, No 4, 2015, 68-70
 26. . Vasilev V., *Clinical Algorithm for Diagnosis and Treatment of Diabetic Foot Syndrome*, Management and Education Magazine, ISSN 1312-6121, Vol. X (5) 2014, 21-24.
 27. Vassilev, V., O. Matkov, T. Kavtrakov, H. Abrashev, *Vascular aspects in treatment of diabetic foot*, Trakia journal of scientific, ISSN 1313-7050, 2014, 241-243.
 28. Vasilev, V. D. Tanev, T. Kavtrakov, H. Abrashev, *Our experience in surgical treatment of the complicated forms of colorectal cancer*, Trakia Journal of Sciences, No 4, 2015, 68-70.

**GENERALIZED NET MODEL OF STOCHASTIC
EXPECTATION-MAXIMIZATION ALGORITHM**

Stanislav Popov

E-mail: stani_popov@yahoo.com

ABSTRACT

The Expectation-Maximization (EM) algorithm is a way to find maximum-likelihood estimates for model parameters when the data is incomplete, has missing data points, or has unobserved (hidden) latent variables. A variation (Stochastic Expectation-Maximization algorithm – SEM) of the above-stated algorithm is presented in the current research with the usage of Generalized nets apparatus. The constructed Generalized net can be used for describing and monitoring the parallel processes in the SEM algorithm.

Keywords: Stochastic Expectation-Maximization algorithm, Generalized nets.

INTRODUCTION

Expectation–Maximization is successfully applied in data mining as an iterative method that attempts to find the maximum likelihood estimator of a parameter θ of a parametric probability distribution. The aim is to maximize the Q -function which is the result of subtraction between the target value and initial estimate of θ .

The standard EM auxiliary function is the best estimate of the complete-data log-likelihood in the sense of the conditional mean squared error [9]. The idea underlying the Stochastic Expectation-Maximization algorithm, like other stochastic EM variants, is that there might be no need to ask for such a “good” estimate. Therefore, SEM replaces the standard auxiliary function with: $\hat{Q}(\theta | \theta') = \log p(z' | \theta')$, where z' is a random sample drawn from the posterior distribution of the unobserved variable⁶, $p(z | y, \theta)$. This leads to the following modified iteration; given a current estimate θ_n [13]:

- Simulation step: compute $p(z | y, \theta_n)$ and draw an unobserved sample z_n from $p(z | y, \theta_n)$;
- Maximization step: find:
 $\theta_{n+1} = \arg \max_{\theta} p(z_n | \theta)$.

Various schemes can be used to derive a pointwise limit, such as averaging the estimates over iterations once stationarity has been reached. It was established in some specific cases that

stationary parametric density function concentrates around the likelihood maximizer with a variance inversely proportional to the sample size.

**GENERALIZED NET MODEL OF THE
STOCHASTIC EXPECTATION-
MAXIMIZATION ALGORITHM**

The concept of Generalized nets (GNs) is introduced in [2-4]. Examples of constructed Generalized nets for data mining processes are presented in [1, 6-8, 11, 12, 14, 15].

In the current research, the GN of the Stochastic Expectation-Maximization algorithm contains 8 transitions and 23 places (Fig. 1). The Generalized net consists of the following set of transitions:

$$A = \{Z_1, Z_2, Z_3, Z_4, Z_5, Z_6, Z_7, Z_8\},$$

where:

- Z_1 - “choosing random observed variable (y)”;
- Z_2 - “choosing latent variable (z)”;
- Z_3 - “formulating the parametric density of y and parametric density of z ”;
- Z_4 - “formulating the aggregate parametric density of y and z , $p(z | y, \theta)$ ”;
- Z_5 - “computing $p(z | y, \theta_n)$ ”;
- Z_6 - “extracting an unobserved sample (z_n) from $p(z | y, \theta_n)$ ”;
- Z_7 - “forming the replacement function $\hat{Q}(\theta | \theta_n)$ ”;
- Z_8 - “finding $\theta_{n+1} = \arg \max_{\theta} p(z_n | \theta)$ ”;

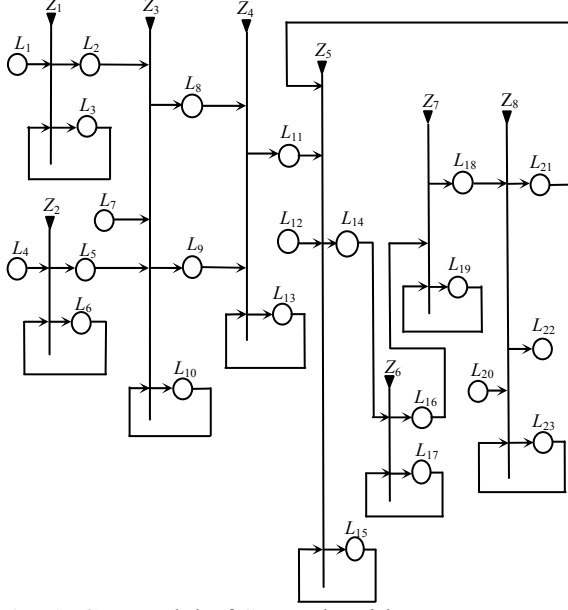


Fig. 1. GN model of SEM algorithm

α -token enters the GN via place L_1 . The token has initial characteristic “*observed variables*”. The token entering L_3 does not obtain any new characteristic. After the activation of transition Z_1 , the α -token moves to place L_2 and obtains the following characteristic “*chosen observed variable*”.

Transition Z_1 has the following form:

$$Z_1 = \langle \{L_1, L_3\}, \{L_2, L_3\}, R_1, \vee(\wedge(L_1, L_3)), \rangle$$

where:

$$R_1 = \begin{array}{c|cc} & L_2 & L_3 \\ \hline L_1 & false & true \\ L_3 & W_{3,2} & true \end{array}$$

and

$W_{3,2}$ = “the observed variable is chosen”.

β -token enters the GN via place L_4 with initial characteristic “*latent variables*”. The token entering L_6 does not obtain any new characteristic. After the activation of transition Z_2 , the β -token moves to place L_5 and obtains the following characteristic “*chosen latent variable*”.

Transition Z_2 has the following form:

$$Z_2 = \langle \{L_4, L_6\}, \{L_5, L_6\}, R_2, \vee(\wedge(L_4, L_6)), \rangle$$

where:

$$R_2 = \begin{array}{c|cc} & L_5 & L_6 \\ \hline L_4 & false & true \\ L_6 & W_{6,5} & true \end{array}$$

and

$W_{6,5}$ = “the latent variable is chosen”.

γ -token enters the GN via place L_7 with initial characteristic “*parameter to estimate*”. The to-

kens entering L_{10} do not obtain any new characteristic. After the activation of transition Z_3 , the tokens from places L_2 , L_5 and L_7 merge into two tokens (α_1 and β_1) in places L_8 and L_9 with characteristics, respectively, “*formed parametric density of the observed variable*” and “*formed parametric density of the latent variable*”.

Transition Z_3 has the following form:

$$Z_3 = \langle \{L_2, L_5, L_7, L_{10}\}, \{L_8, L_9, L_{10}\}, R_3, \vee(\wedge(L_2, L_5, L_7), L_{10}), \rangle$$

where:

$$R_3 = \begin{array}{c|ccc} & L_8 & L_9 & L_{10} \\ \hline L_2 & false & false & true \\ L_5 & false & false & true \\ L_7 & false & false & true \\ L_{10} & W_{10,8} & W_{10,9} & true \end{array}$$

and

$W_{10,8}$ = “the parametric density $p(y/\theta)$ is formed”;

$W_{10,9}$ = “the parametric density $p(z/\theta)$ is formed”

After the activation of transition Z_4 , the tokens in places L_8 and L_9 merge into one α_2 -token in place L_{11} with characteristic “*formed aggregate parametric density, $p(z|y, \theta)$* ”. The tokens entering L_{13} do not obtain any new characteristic.

Transition Z_4 has the following form:

$$Z_4 = \langle \{L_8, L_9, L_{13}\}, \{L_{11}, L_{13}\}, R_4, \vee(\wedge(L_8, L_9), L_{13}), \rangle$$

where:

$$R_4 = \begin{array}{c|cc} & L_{11} & L_{13} \\ \hline L_8 & false & true \\ L_9 & false & true \\ L_{13} & W_{13,11} & true \end{array}$$

and

$W_{13,11}$ = “the aggregate parametric density of y and z is formed, $p(z|y, \theta)$ ”.

δ -token enters the GN via position L_{12} with initial characteristic “*current estimation*”. At the first activation of the Z_5 transition, the tokens from places L_{11} and L_{12} merge into a new γ_1 -token in place L_{14} with characteristics “*parametric density of current estimation, $p(z|y, \theta_n)$* ”.

At the second activation of the transition, the tokens from places L_{11} , L_{12} and L_{21} merge into a new γ_2 -token with characteristic “*parametric density of next estimation, $p(z|y, \theta_{n+1})$* ”. The tokens entering L_{15} do not obtain any new characteristic.

Transition Z_5 has the following form:

$$Z_5 = \langle \{L_{11}, L_{12}, L_{15}, L_{21}\}, \{L_{14}, L_{15}\}, R_5, \vee(\wedge(L_{11}, L_{12}, L_{15}), L_{21}) \rangle,$$

where:

$R_5 =$		L_{14}	L_{15}
	L_{11}	<i>false</i>	<i>true</i>
	L_{12}	<i>false</i>	<i>true</i>
	L_{15}	$W_{15,14}$	<i>true</i>
	L_{21}	<i>false</i>	<i>true</i>

and

$W_{15,14}$ = “the current estimation of $p(z|y, \theta_n)$ is made” (at the first activation of the transition);

$W_{15,14}$ = “the next estimation of $p(z|y, \theta_{n+1})$ is made” (at the second activation of the transition);

After the activation of transition Z_6 , the γ_I -token from place L_{14} moves to place L_{16} and obtains the following characteristic “*drawn unobserved sample, z_n* ”. The token entering L_{17} does not obtain any new characteristic.

Transition Z_6 has the following form:

$$Z_6 = \langle \{L_{14}, L_{17}\}, \{L_{16}, L_{17}\}, R_6, \vee(L_{14}, L_{17}) \rangle,$$

where:

$R_6 =$		L_{16}	L_{17}
	L_{14}	<i>false</i>	<i>true</i>
	L_{17}	$W_{17,16}$	<i>true</i>

and

$W_{17,16}$ = “an unobserved sample is extracted from $p(z|y, \theta_n)$ ”.

After the activation of transition Z_7 , the token from L_{16} moves to place L_{18} with the following characteristic “*formed $\hat{Q}(\theta / \theta_n)$* ”.

Transition Z_7 has the following form:

$$Z_7 = \langle \{L_{16}, L_{19}\}, \{L_{18}, L_{19}\}, R_7, \vee(L_{16}, L_{19}) \rangle,$$

where:

$R_7 =$		L_{18}	L_{19}
	L_{16}	<i>false</i>	<i>true</i>
	L_{19}	$W_{19,18}$	<i>true</i>

and

$W_{19,18}$ = “the replacement $\hat{Q}(\theta / \theta_n)$ is formed”.

ε -token enters the GN via place L_{20} with initial characteristic “*criterion for maximization, $\arg \max_{\theta} p(z_n | \theta)$* ”. After the activation of transition Z_8 , the tokens from places L_{18} and L_{20} move to place L_{21} or L_{22} depending on whether the criterion is met with characteristics respectively “ $\theta_{n+1} \neq \arg \max_{\theta} p(z_n | \theta)$ ” for L_{21} and

“ $\theta_{n+1} = \arg \max_{\theta} p(z_n | \theta)$ ” for L_{22} . The tokens entering L_{23} do not obtain any new characteristic.

Transition Z_8 has the following form:

$$Z_8 = \langle \{L_{18}, L_{20}, L_{23}\}, \{L_{21}, L_{22}, L_{23}\}, R_8, \vee(\wedge(L_{18}, L_{20}), L_{23}) \rangle,$$

where:

$R_8 =$		L_{21}	L_{22}	L_{23}
	L_{18}	<i>false</i>	<i>false</i>	<i>true</i>
	L_{20}	<i>false</i>	<i>false</i>	<i>true</i>
	L_{23}	$W_{23,21}$	$W_{23,22}$	<i>true</i>

and

$W_{23,21}$ = “the n -th estimate of θ is increased by 1”;
 $W_{23,22}$ = “a parameter θ which maximizes the Q -function is found”

CONCLUSION

The EM algorithm and its variants are regularly used to solve a broad range of today’s estimation problems, from the multiple EM for motif-finding in DNA sequences [5], to fitting mixture models to disambiguate targets from clutter in radar [16]. The GN model presented in the current research shows how the Stochastic Expectation-Maximization algorithm works by splitting its two main steps into smaller ones and describing them in detail.

REFERENCES

1. Atanassov, K. Generalized Nets as a Tool for the Modelling of Data Mining Processes, IN: *Innovative Issues in Intelligent Systems, Vol. 623 of the series Studies in Computational Intelligence*, 2016, pp.161-215
2. Atanassov, K., E. Sotirova, Generalized Nets, Prof. Marin Drinov Academic Publishing House, 2017 (in Bulgarian)
3. Atanassov, K. Generalized Nets, World Scientific, Singapore, 1991
4. Atanassov, K., On Generalized Nets Theory, Prof. M. Drinov Academic Publishing House, Sofia, 2007
5. Bailey, T., C. Elkan, Unsupervised learning of multiple motifs in biopolymers using expectation maximization, *Machine Learning, Vol. 21*, pp. 51–80, 1995.
6. Bureva, V., E. Sotirova, K. Atanassov, Hierarchical generalized net model of the process of clustering, *Issues in Intuitionistic Fuzzy Sets and Generalized Nets, Vol.1*, Warsaw

- School of Information Technology, 2014, pp.73-80.
7. Bureva, V., E. Sotirova, K. Atanassov, Hierarchical generalized net model of the process of selecting a method for clustering, *15th Int. Workshop on Generalized Nets*, Burgas, 16 October 2014, pp. 39–48.
 8. Bureva, V., E. Sotirova, S. Popov, D. Mavrov, V. Traneva, Generalized Net of Cluster Analysis Process Using STING: A Statistical Information Grid Approach to Spatial Data Mining, Henning Christiansen, Hélène Jaudoin, Panagiotis Chountas, Troels Andreasen, Henrik Legind Larsen (Eds.): *Flexible Query Answering Systems - 12th International Conference, FQAS 2017, London, UK, June 21-22, 2017. Proceedings. Lecture Notes in Computer Science 10333*, Springer, 2017, ISBN 978-3-319-59691-4
 9. Celeux, G. and J. Diebolt, *The SEM Algorithm: a Probabilistic Teacher Algorithm Derived from the EM Algorithm for the Mixture Problem*. Computational Statistics Quarterly, 2:73– 82, 1985.
 10. Gupta, M., Y. Chen, Theory and Use of the EM Algorithm, *Foundations and TrendsR in Signal Processing* Vol. 4, No. 3, 2010, pp.224–228
 11. Han, J., M. Kamber, J. Pei, *Data Mining Concepts and Techniques*, Third Edition, Elsevier, 2012
 12. Krawczak M., S. Sotirov, E. Sotirova, Generalized net model for parallel optimization of multilayer neural network with time limit, Proc. of 6th IEEE Int. Conf. on Intelligent Systems IS'12, 2012, pp.173-177. Print ISBN: 978-1-4673-2276-8
 13. Roche, A., EM algorithm and variants: an informal tutorial, Service Hospitalier Frederic Joliot, CEA, F-91401 Orsay, France, Spring 2013, p.12.
 14. Roeva O., T. Pencheva, A. Shannon, K. Atanassov, *Generalized Nets in Artificial Intelligence. Volume 7: Generalized Nets and Genetic Algorithms*, Prof. Marin Drinov Academic Publishing House, 2013, ISBN:978-954-322-700-6
 15. Sotirova, E., D. Orozova, Generalized net model of the phases of the data mining process, *Developments in Fuzzy Sets, Intuitionistic Fuzzy Sets, Generalized Nets and Related Topics. Vol. II: Applications*, Poland, 2010, pp. 247–260.
 16. Wang, J., A. Dogandzic, A. Nehorai, Maximum likelihood estimation of compound-Gaussian clutter and target parameters, *IEEE Transactions on Signal Processing*, vol. 54, no. 10, October 2006, pp. 3884–3898

THERMOELECTRIC ENERGY CONVERTORS: FEATURES AND OPERATING MODES

Ivaylo Belovski
E-mail: ivbel@abv.bg

ABSTRACT

Thermoelectric energy converters have become very popular in recent years. This is due to the continuous improvement of the materials used for their manufacturing and the increase of their efficiency. They can work as thermoelectric refrigerators or heaters (depending on the polarity of the power supply) or as thermoelectric generators of electromotive voltage. This wide spectrum of their application is based on the different physical effects which this type of converters uses in their operation. The purpose of this article is to present the specific features and parameters of thermoelectric energy converters and their other operation modes.

Key words: thermoelectric energy converters, Peltier-Seebeck effect, TEC, TEG

INTRODUCTION

Thermoelectric energy converters can be generally classified into three groups depending on the effect employed:

- Thermoelectric generators;
- Thermoelectric refrigerators;
- Thermoelectric heaters.

Thermoelectric generators use the Seebeck effect in their operation, while thermoelectric refrigerators use the Peltier effect. The effect of Thomson is another thermoelectric effect.

The Seebeck effect is conversion of the heat gradients existing in nature or resulting from human activities ΔT directly into electric power [1]. This effect was discovered accidentally for the first time by the German-Estonian physicist Thomas Johan Seebeck in 1821. He found that electric voltage is generated between the two ends of a metal rod when there is temperature difference ΔT in it. He also established that the magnetic needle of the compass deflects if placed near a closed circuit built of two different metal wires if there is temperature difference between the points of their connection (place of measurement).

The Seebeck effect is described as follows: if in an open electric circuit consisting of two different conductors (Fig. 1) and one contact is kept at temperature T_1 while the other at T_2 , then if $T_1 > T_2$, thermal electromotive force (thermal EMF) is generated at the ends of the circuit

[2]. When the circuit is closed, an electric current passes through it.

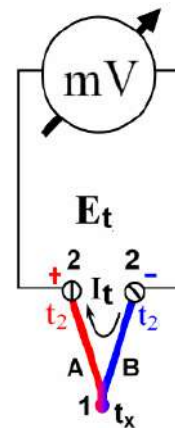


Fig. 1. Thermoelectric element consisting of two dissimilar materials: A, B, with different coefficients of thermal EMF

The Peltier effect is the conversion of electric energy into temperature difference ΔT [3, 4]. If an electric current is passed through a thermoelectric element consisting of two semiconductors with a different kind of conductivity, then a certain amount of heat is absorbed or emitted at the joints (depending on the current direction).

The Peltier effect is explained by simplified band diagram at the juncture N-type semiconductor – Metal – P-type semiconductor (Fig. 2).

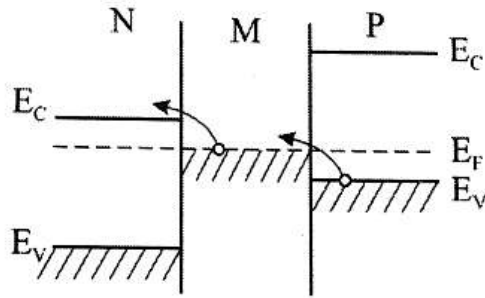


Fig. 2. Band diagram at the junction N-type semiconductor – Metal – P-type semiconductor

When a current I is driven in the direction shown, the electrons passing from P-type to N-type semiconductor at the joint must go to higher energy levels, thus absorbing thermal energy from the crystal lattice of the metal and the semiconductor, thereby cooling them down. In reverse direction of the current, the electrons descend to lower energy levels, give off heat at the joints and they are heated.

The Thompson effect is also a thermoelectric effect. It explains the fact that, if a current is driven through a conductor or semiconductor where there is a temperature gradient, a certain amount of heat is absorbed or generated in addition to the Joule heat, depending on the current direction [5, 6].

Due to the exhaustion of the conventional sources of energy, alternative sources are becoming increasingly popular: thermoelectric generators, photovoltaic systems, fuel cells [7-10], etc.

THESIS

A. Thermal electromotive force generation mode.

A schematic diagram of a thermoelectric unit operating in generator mode is presented in Fig.3. If the junctions between the two materials have different temperatures, T_1 and T_2 , then there will be a thermoelectric current in the circuit [2, 11, 12]. In an open circuit, thermal electromotive force E will be observed:

$$E = \int_{T_2}^{T_1} [\alpha_1(T) - \alpha_2(T)] dT \quad (1),$$

where α_1, α_2 - coefficients of thermal EMF for materials 1 and 2. If α_1, α_2 dependence on temperature is negligible, then:

$$E = (\alpha_1 - \alpha_2)(T_1 - T_2) \quad (2)$$

If the thermoelectric circle is built from several thermocouples connected in series, then the total EMF is defined as the sum of the individual EMF of all thermocouples.

For thermoelectric units the branches of which are built from semiconductors of different type of conductivity connected at one end with metal bridge (Fig. 3), the metal junctions 1, 2 and 3 placed under the same temperature conditions will not affect the total EMF generated [2].

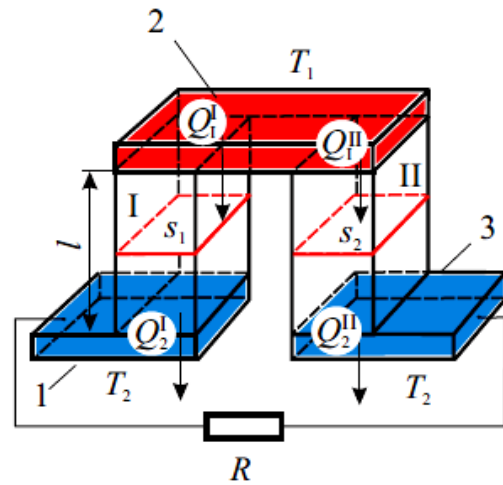


Fig. 3. Thermoelectric unit - Q_1', Q_1'' - incoming heat flows, Q_2', Q_2'' - outgoing heat flows, T_1, T_2 - temperatures of the hot and cold side, respectively, l - branch height, s_1, s_2 - areas of the cross-sections of the branches.

The efficiency coefficient of the thermoelectric unit η is determined by the law of conservation of energy by taking into account the heat flow through the thermoelectric unit and the electric current I flowing through external load R . In this case,

$$Q_1' + Q_1'' - Q_2' - Q_2'' = I^2 R \quad (3)$$

And for the efficiency we obtain:

$$\eta = \frac{Q_1' + Q_1'' - Q_2' - Q_2''}{Q_1' + Q_1''} \quad (4)$$

The numerator is the electric power over the load R and the denominator is the dissipated heat power.

In the absence of an electric current I (without load R), the heat flow is determined only by the heat conductivity of the material:

$$-ks \frac{dT}{dx} = \frac{s}{l} \int_{T_2}^{T_1} k dT, \quad (5)$$

where k is the coefficient of heat conductivity.

With load R connected to the circuit, the effects of both heats of Joule and Thompson must be taken into account.

$$Q_J = \frac{I^2}{s} \int_0^l \rho dx, \quad (6)$$

$$Q_T = I \int_{T_2}^{T_1} \tau_T dT, \quad (7)$$

where Q_J and Q_T are the heats of Joule and Thompson, respectively, ρ - specific resistance, τ_T - coefficient of Thompson.

It is well known that half of the heat powers of Joule and Thompson dissipated in the thermoelectric unit is driven to the hot side and the other half is absorbed by the cold side.

For a rough estimation of the efficiency (differing by no more than 10% from the one made with more precise methods), the following expression can be used:

$$\eta = \frac{1}{4} \frac{T_1 - T_2}{T_1} Z_0 T', \quad (8)$$

where:

$$T' = \frac{T_1 + T_2}{2} \quad (9)$$

$$Z_0 = \frac{\alpha^2}{((\sqrt{k_1 \rho_1}) + (\sqrt{k_2 \rho_2}))^2} \quad (10),$$

Z_0 - quality factor of the thermoelectric unit; $\alpha = \alpha_1 - \alpha_2$; k_1, k_2 - coefficients of heat conductivity of the two branches of the unit; ρ_1, ρ_2 - specific resistances of the materials.

For a more precise calculation of the efficiency, one should take into account not only the internal resistance of the N and P semiconductors r but also the resistance at the junctures with the metal plates. Approximately, the effective electric resistance at the switching plates can be determined by the equation [11]:

$$R_{plate} = \frac{\rho_p (b - \frac{2a}{3})}{s}, \quad (11)$$

where: ρ_p - specific resistance of the plate material; s - area of its cross-section; b - plate length; a - width of thermoelectric unit branches.

The efficiency of thermoelectric devices can be increased by both, using materials of higher quality factor Z_0 and increasing ΔT . The quality factor is usually increased by the so-called "cascading", where several thermoelectric units are placed one over the other to form a heat chain connected in series. In this case, the materials and the temperature interval ensure the highest possible Z_0 .

B. Cooling mode

Refrigeration using the Peltier effect was investigated by the German scientist Edmund Altenkirch back in 1911 [13]. For his studies, he used a thermocouple of metal conductors. The analysis of the results obtained led him to the conclusion that this method of refrigeration has no perspective. Only after the researches of the Russian scientist Abram Yoffe and his associates, the perspectives for the use of this method with the application of semiconductors was clarified in the 1950-ies and theoretical studies aimed at the practical implementation of semiconductor thermoelectric units began.

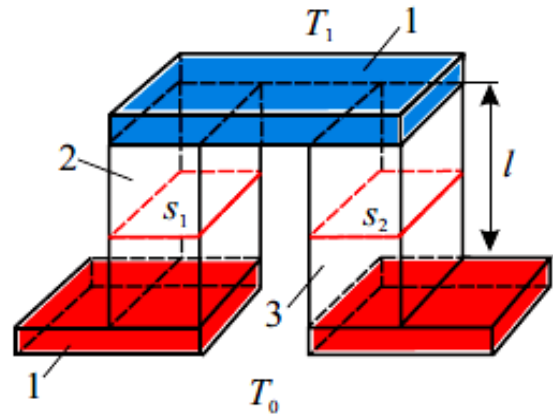


Fig. 4. Thermoelectric refrigerator: 1 – switching plates; 2, 3 – N and P type semiconductors

Thermoelectric converters using the Peltier effect are called thermoelectric refrigerators (TER). TERs contain two branches of different types of semiconductor – N and P , with cross-sections s_1, s_2 and length l (Fig. 4) [2].

If electric current I is driven through such a thermoelectric unit from N to P semiconductor at normal constant temperature, it can be observed

after a short period (several seconds) that the upper end has cooled to temperature T_1 - lower than the ambient, while the lower end has been heated to temperature T_0 - higher than the ambient. The analysis of the thermoelectric unit takes into account the dissipated Joule heat but neglects the Thompson effect. In this case, it is assumed that half of the Joule heat is transferred to the cold side while the other half is transferred to the hot side [2, 14]

The heat power absorbed by the cold side is:

$$Q = -\Pi I + 0.5rI^2, \quad (12)$$

where: Π - Peltier coefficient, r - resistance of the thermoelectric unit, I - the current through it.

The cold end absorbs the heat Q_0 dissipated by the object to be cooled or from the environment contacting with it, as well as the heat transferred through the branches (due to heat conductivity) from the hot to the cold end.

Three modes of operation are known for the thermoelectric refrigerator:

- 1) *Maximal refrigeration mode* – for maximal temperature difference ΔT ;
- 2) *Maximal refrigeration production mode*;
- 3) *Maximal saving mode*.

Maximal refrigeration mode is achieved under conditions of $Q_0 = 0$ (no heat load). In this case, the heat balance equation for the cold end becomes:

$$-k_0\Delta T = -\Pi I + 0.5rI^2, \quad (13)$$

where k_0 - coefficient of heat conductivity of the branches.

It follows from (12) and (13) that:

$$I_{opt} = \frac{\Pi}{r} \quad (14)$$

$$Q_{max} = \frac{\Pi^2}{2r} \quad (15)$$

The maximal temperature difference is:

$$\Delta T_{max} = \frac{\Pi^2}{2k_0r}, \quad (16)$$

where:

$$r = l \left(\frac{1}{\sigma_1 s_1} + \frac{1}{\sigma_2 s_2} \right), \quad k_0 = \frac{1}{l} (k_1 s_1 + k_2 s_2) \quad (17)$$

σ_1, σ_2 - coefficients of electric conductivity of the branches; k_1, k_2 - coefficients of heat conductivity.

Expression (16) can be written as:

$$\Delta T_{max} = 0,5Z_0T_1^2, \quad (18)$$

where:

$$Z_0 = \left[\frac{\alpha_1 - \alpha_2}{\sqrt{\frac{k_1}{\sigma_1}} + \sqrt{\frac{k_2}{\sigma_2}}} \right]^2 \quad (19)$$

α_1, α_2 - coefficients of thermal EMF of the two branches. The minimal temperature of the cold side is determined by the expression:

$$T_{1min} = \frac{\sqrt{1 + 2T_0Z_0} - 1}{Z_0} \quad (20)$$

Maximal refrigeration production mode is achieved under condition $Q_0 = Q_{0max}$, i.e. in the presence of maximal heat load. Then, the heat balance equation is:

$$(\alpha_1 - \alpha_2)IT_1 - 0.5rI^2 - k_0\Delta T = Q_0 \quad (21)$$

The temperature difference in the maximal refrigeration production is:

$$\Delta T = \Delta T_{max} - \frac{Q_0}{k_0} \quad (22)$$

For description of the maximal saving mode, refrigeration coefficient ε is introduced as follows:

$$\varepsilon = \frac{Q_0}{W}, \quad (23)$$

where

$$W = rI^2 + (\alpha_1 - \alpha_2)\Delta TI \quad (24)$$

W - electric power consumed by the thermoelectric unit.

The optimization by current, where $\varepsilon = \varepsilon_{max}$ is:

$$I_{opt} = \frac{(\alpha_1 - \alpha_2)\Delta T}{r \left[\sqrt{1 + 0,5Z_0(T_0 + T_1)} - 1 \right]} \quad (25)$$

$$\varepsilon_{\max} = \frac{T_1}{\Delta T} \frac{\sqrt{1+0,5Z_0(T_0+T_1)} - T_0/T_1}{\sqrt{1+0,5Z_0(T_0+T_1)} + 1} \quad (26)$$

While the optimal voltage supply of the thermoelectric unit should be:

$$U_{opt} = \frac{(\alpha_1 - \alpha_2)\Delta T}{\sqrt{1+0,5Z_0(T_0+T_1)} - 1} \quad (27)$$

It follows from (26) that the refrigeration coefficient ε depends not only on the quality factor Z_0 but also on the average temperature and the temperature difference ΔT . At $\Delta T \rightarrow \Delta T_{\max}$, $\varepsilon \rightarrow 0$. This is normal as long as ΔT_{\max} is reached at $Q_0 = 0$.

At $\Delta T \rightarrow 0$, ε_{\max} increases.

C. Heating mode – thermoelectric heaters

Thermoelectric units are less frequently used as heaters. Their wider use is as sources of EMF and thermoelectric refrigerators. For this purpose, some of the main dependencies and parameters of this mode of operation will be presented in this paper rather than a detailed review.

The model presented in Fig. 4 can be used for the description of the thermoelectric unit, assuming that the cold side is thermostatted at temperature T_0 and the hot side dissipates heat power Q_w at temperature T_1 . Current direction is opposite to that in refrigeration mode. In this case, the heat power dissipated at the hot end is [2]:

$$Q_w = (\alpha_1 - \alpha_2)T_1 I + 0,5I^2 \left(\frac{1}{\sigma_1 s_1} + \frac{1}{\sigma_2 s_2} \right) - \frac{T_1 - T_0}{l} (k_1 s_1 + k_2 s_2) \quad (28)$$

The efficiency of the thermoelectric heating is determined by the coefficient of conversion K_h .

$$K_h = \frac{Q_w}{W} \quad (29)$$

The optimization by the voltage supply is obtained from the condition: $\frac{dK_h}{dU} = 0$ and it is:

$$U_{opt} = \frac{(\alpha_1 - \alpha_2)(T_1 - T_0)}{M - 1}, \quad (30)$$

where:

$$M = \sqrt{1+0,5Z(T_1+T_2)} \quad (31)$$

CONCLUSIONS

The following conclusions can be made on the basis of the discussion above:

The thermoelectric units depending on the effect employed can be used as generators of thermoelectric EMF, thermoelectric refrigerators or heaters.

The thermoelectric efficiency of a particular thermoelectric device depends entirely on the materials from which it is made and the temperature gradient applied.

The future development of technologies and the expected improvement of the efficiency of the thermoelectric devices is aimed mainly at the development of new materials with higher efficiency.

ACKNOWLEDGMENT

This work was supported by the Bulgarian Ministry of Education and Science under the National Research Programme “Young scientists and postdoctoral students”, approved with DCM #577/17.08.2018.

REFERENCES

1. Rowe D. M., 2006. *Thermoelectrics Handbook*. Macro to Nano, Taylor & Francis. ISBN 0- 8493-2264-2.
2. Anatyshuk L.I. 2003. *Thermoelectric energy converters*, Kyiv, Chernivtsi. Institute of Thermoelectricity
3. Aleksandrov, A. 2012. *Poluprovodnikov elementi i integralni shemi*, Gabrovo, Eks-pres.
4. Bulat L. P., 1997, *Thermoelectricity*, 4, 3-34
5. Godfrey S., 1996. *An Introduction to Thermoelectric Coolers*, Electronics Cooling, vol.2. No.3.
6. Thomson, W. 1851. *On a mechanical theory of thermoelectric currents*. Proc.Roy.Soc.Edinburgh: 91–98.
7. Midyurova B., Nenov V., *Simultaneous energy generation and organic matter removal in a single chamber microbial fuel cell*, Academic Journal Industrial technologies, vol V (1) 83-87, 2018.
8. Midyurova B., Nenov V., *Electricity Generation in Microbial Fuel Cell as a Function of Air: Cathode Configuration*, 2017, International Journal of Alternative Fuels and Energy, 1.

9. Midyurova B., *Effect of Different External Resistance on Sedimentation Microbial fuel cells Performance*, Proc. X National Conference with International Participation Conference "Electronica 2019", May 16 - 17, 2019, Sofia, Bulgaria
10. Midyurova B., *Bioelectricity production and waste water treatment by air cathode microbial fuel cell*, XVI-th International Conference on Electrical Machines, Drives and Power Systems ELMA 2019, 6-8 June 2019, Varna, Bulgaria
11. Iofee A. F. 1956. *Thermal Conductivity of Semiconductors*, Izv. Akad. Nauk SSSR, Ser. Fiz., **20** 1956, 65, Columbia Tech. Transl. p. 55.
12. Anatyuk L.I. 1998. *Physics of Thermoelectricity*. Kyiv, Chernivtsi. Institute of Thermoelectricity.
13. Altenkirch E., 1911. *Electrothermische Kalteerzeugung und reversible elektrische Heizung*, Phys. Z.,12, (21), 920-924.
14. Snyder G., E. S. Toberer, R. Khanna, W. Seifert, 2012. *Improved Thermoelectric Cooling Based on the Thomson Effect*. *Physical Review B* 86, 045202

SURVEY OF THE IMPACT OF SEASONS OVER THE EFFECTIVENESS OF SOLAR PANELS

Vasil Ivanov, Ivailo Belovski
E-mail: vasil_bi@abv.bg

ABSTRACT

The purpose of the study is the monitoring of solar panels (Solar PV) in a solar network (Solar PV array) in real working conditions to analyse their output during the seasons. The monitoring results are related to external factors (air temperature, temperature of the solar panels and intensity of solar radiation) and internal parameters (voltage, current and power). The analysis of the power output from the solar network proves the higher efficiency of transformation during the transitional seasons, spring and autumn, for large-scale practical application.

Key words: solar PV array, monitoring, internal parameters

INTRODUCTION

According to the National Institute of Meteorology and Hydrology, sunshine in Bulgaria reaches 2200-2500 h annually. In the summer months, the sunshine cycle is over 10 hours in over 1/3 of the days, with the average solar radiation intensity higher than 650 [W/m²] for the time from 8 am to 4 pm. It has been reported that a solar system would work efficiently for over 200 days in the southern regions and 170-180 days in the rest of Bulgaria.

The intensity of solar radiation per square meter G[W/m²] is the main characteristic of the solar power P_{PV}. The solar energy produced is given with the power for the sunshine period, and in practice for Bulgaria the average period is greater than 6.5 hours per day with a solar radiation intensity greater than 410[W/m²]. This allows the efficient use of solar power systems in Bulgaria [1-2].

SOLAR PANELS ARRANGED IN A STRING (STRING PV)

Solar panels represent a system of geometrically arranged solar cells connected in a grid and enclosed in a housing to achieve a higher mechanical resistance.

The connection in the form of a string (Fig. 1) is of 18 solar modules 18 times raise UPV1.

The external factors impacting the size and stability of the generated power PPV are defined as follows: geographic location, topography and climate of the environment, total area orientation angle of solar panels, daytime temperature range,

temperature, humidity and dustiness of the environment and cloudy weather.

The power PPV obtained from the solar panels under standard test conditions (STC) is the maximum and is defined as “peak” power Wp.

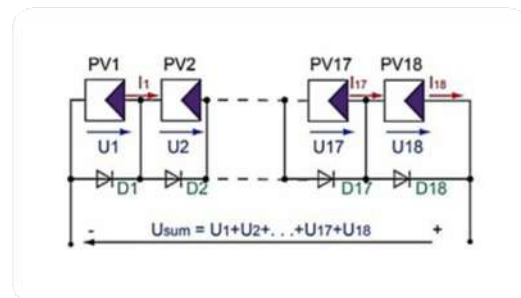


Fig. 1. Solar photovoltaics connected in string (PV string) for higher voltage U_{sum}

The nominal mode of the solar panels is calculated at the maximum power point P_{mpp} of the V-A characteristic. It is fixed by converters (DC/DC) with tracking algorithms at the maximum power point (Maximum Power Point Tracker). The converters connect with their input to the solar panel and the output is towards the energy consumer. In this way, a connection is made towards a solar generator architecture with stabilized electrical parameters.

The active power P_{PV} is calculated from the voltage U_{PV}, [V] and current I_{PV}[A] generated by the solar panels:

$$P_{PV} = U_{PV} \cdot I_{PV}, [W]. \quad (1)$$

The peak power P_{mpp} , [Wp] is calculated from the voltage U_{mpp} , [V] and current I_{mpp} , [A] values in the maximum power point:

$$P_{mpp} = U_{mpp} \cdot I_{mpp}, [Wp]. \quad (2)$$

Standard test conditions define the maximum efficiency factor η_{PV_max} , stated by the solar panel manufacturers. For polycrystalline silicon solar panels, the efficiency ratio η_{PV} reaches a maximum value of up to 20%.

It is calculated by the formula:

$$\eta_{PV} = P_{pvout} / P_{pvin} \cdot 100\%. \quad (3)$$

$$P_{pvin} = G \cdot S_{pv}. \quad (4),$$

where:

P_{pvin} is the input power expressed with solar radiation G falling over the total S_{pv} area of PV.

The application of the beneficial power P_{PV} produced from the solar generator is defined by the type of consumer for constant or variable load. The voltage inverter (DC/AC) as a load converts the constant power to the AC power. For the effective transfer of active power P_{PV} the impedances of the generator and the consumer are harmonized. This improves the efficiency and working period of the devices in the system [3].

ARCHITECTURE OF A SOLAR INSTALLATION

The schematic diagram (Fig. 2) includes the main elements for generating electrical energy.

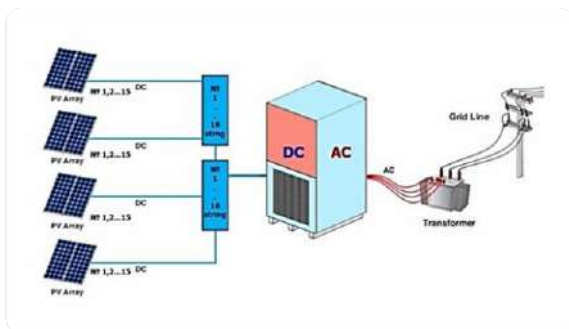


Fig. 2. Structure of a solar system connected to the public electricity network

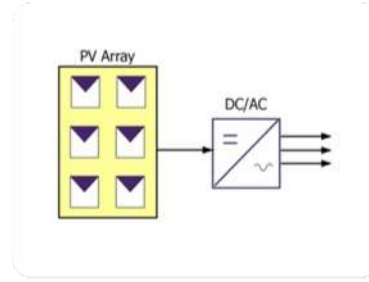


Fig. 3. Solar array (Solar PV array) connected to a DC/AC voltage inverter.

The main units of the solar system in Fig. 2 and Fig. 3 are as follows:

1. Solar PV panels connected in strings of 18 pieces in row and 15 pieces in parallel;
2. Collecting boxes integrating the arrays of solar modules;
3. $S_{pv} = 4062.24m^2$ is the total area of the solar field built with 2232 solar panels;
4. DC/AC - Three phase voltage inverter;
5. Transformer is a networking transformer in a star/triangle shape to increase voltage;
6. Grid line is a three-wire line for connection to a high voltage network.

ARCHITECTURE OF THE MONITORING SYSTEM

The architecture of the monitoring system includes tracking devices connected to sensors for temperature and intensity of solar radiation. Other elements of the system record the input/output parameters U_{PV} and I_{PV} in the collection boxes. They bring together the strings of individual solar panels into a grid (Solar PV array).

CONCLUSIONS AND ANALYSES

1. The measurement results obtained are reported for monthly periods of time plotted for G , P_{pvout} , P_{pvin} , $t[^\circ C]$ and $W [kWh]$, with the tabular data used in the computation part.

2. The calculations are for the mean monthly values for the non-electric values $t[^\circ C]$, $G[W/m^2]$ and the electrical P_{pvout} , P_{pvin} parameters. A comparative analysis of solar panel performance is made during the four seasons of the year.

3. Analysing the results, the months with the highest values of η_{PV} , P_{pvin} , P_{pvout} are determined. They are decisive for the optimal performance of the system required for large-scale practical application.

REFERENCES

1. Yilmaz, S.; Ozcalik, H.; Kesler, S.; Dincer, F.; Yelmen, B. *The analysis of different PV power systems for the determination of optimal PV panels and system installation—A case study in Kahramanmaras, Turkey*. *Renew. Sustain. Energy Rev.* **2015**, *52*, 1015–1024.
2. Bagarella, G.; Lazzarin, R.; Noto, M. *Annual simulation energy and economic analysis of hybrid heat pump systems for residential buildings*. *Appl. Therm. Eng.* **2016**, *99*, 485–494.
3. Stoyanov, Iv., V. Ivanov, T. Iliev, E. Ivanova, G. Mikhailov. “Modeling the Operation of Power Electronic Converters for Electricity Used in Photovoltaic Systems”, *TU-Sofia Yearbook*, Volume 67, Book 1, page 123, 2017, ISSN 1311- 0829.4.

MODERNIZATION OF THE STREET LIGHTING SYSTEM OF A RESIDENTIAL DISTRICT

Mladen Proykov
E-mail: m_proykov@abv.bg

ABSTRACT

As a result of research data, measures are proposed to improve the energy efficiency of street lighting by introducing new LED lighting and a modern lighting management system.

Key words: street lighting, lighting classification, LED luminaires

INTRODUCTION

The improvement of lighting and energy performance of LED lighting creates conditions for achieving high energy efficiency of street lighting systems compared to conventional technologies. The new BS EN13201: 2016 standard [1] has been introduced and is in force in Bulgaria for the classification of streets and normalization of quantitative and qualitative lighting indicators. This paper presents the main results of a 2014 analysis of the state of the street lighting system in Meden Rudnik residential district of Burgas. The impact of its modernization with the introduction of new energy-efficient lighting and a control system to increase the energy performance and characteristics of street lighting has been evaluated. The assessment was made on the basis of an analysis of the existing state of the street lighting system.

ELECTRICAL ENERGY RESEARCH

The electric energy research of the existing street lighting in Meden Rudnik residential district was carried out in 2014 and includes the following steps and activities:

- research of the existing street lighting system;
- preparation of lighting classification of the streets;
- analysis of the energy consumption of the street lighting system;
- digital mapping of the street lighting system.

A study was made of the current state, number and type of street poles and lighting powered by street panel boards (PB). The location of the PB and the type of their control system were examined. All elements of the street lighting

system were mapped and marked on a digital model of the cadastral plan of the residential district made with AutoCAD software.

As a result of an energy audit of street lighting, it was found out that 100% of the existing high-pressure sodium lamps (HDLs) were installed over 20 years ago. The condition of the existing luminaires was relatively good, but they were at the end of their technical and operational lifecycle (Fig. 1). This had led to deterioration of their light and electrical performance and to an increased risk of damage to the luminaires.



Fig. 1. Existing lighting system

The existing light poles were in relatively good condition. They were of three types: trolley, metal and concrete. The research found that there were places where the lighting fixtures were in areas with high vegetation, which impaired the lighting performance on the roadway.

A considerable part of the luminaires had a wide boom angle, from 30° to 60°, which was unsuitable for the width of the roadways, reduced the realized luminance of the roadway and at the same time increased the dazzling effect. These angles were unsuitable for modern LED street lights with optimal boom angles from 0° to 10°.

On the basis of a summary of information on existing street lighting in the residential district,

where a total of 1390 luminaires were installed, Table 2 presents data on the type of lighting, the type of light source, the number and the power of the lighting fixtures. The total installed capacity of the existing street lighting was 94 700W.

Table 1. Type, number and power of existing street luminaires

Luminaires	Power, W	Number
Street luminaire with HDLs	50	854
Street luminaire with HDLs	75	182
Street luminaire with HDLs	100	259
Street luminaire with HDLs	150	83

The power supply came from 66 lighting PB, which are indicated in the cadastral plan.

Most of these PB are in very poor technical condition. There is no control system for the road lighting system. The control of the luminaires is carried out with individual clocks mounted in a PB (Fig. 2).

A relatively large number of PB were established, a total of 66. Practice shows that up to 200 luminaires can be controlled through one PB, but due to the specifics of the layout of the streets in the residential district, this number

could not be achieved [1]. However, given the continued expansion of the district and the construction of new buildings on empty plots, a way to increase the number of illuminators supplied by a PB can be found.

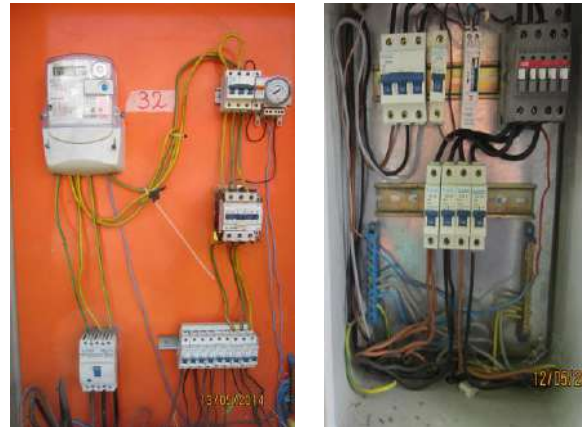


Fig. 2. Street lighting panel board

On the basis of a detailed research of the condition of the lighting fixtures, the type of the lighting poles, the power lines and the power supply PB, a graphical digital model of the existing state of the street lighting in the residential district was developed (Table 2). Appropriate graphic symbols indicate the different types of luminaires, the type of poles and the location of the PB.

Table 2. Condition of street lighting by averages

№	Road Category	Poles arrangement	Roadway width	Sidewalk width	Pole distance	Light Centre high	Boom angle	Power	Luminaire
			m	m					
A	Main	two – sided	16	2,5	35	12	30	150	HDLs
A	Regional	two – sided	14	2,5	30	9	30	150	HDLs
B	Regional	one – sided	17,5	3	30	12	30	100	HDLs
A	Assembly	one – sided	14	3	30	9	30	100	HDLs
B	Assembly	one – sided	7	2,5	25	12	30	75	HDLs
C	Assembly	one – sided	7	2,5	25	9	30	75	HDLs
A	Service	one – sided	10	2,5	35	9	30	75	HDLs
B	Service	one – sided	6	2,5	30	9	30	50	HDLs

Fig. 3 shows part of the digital model with graphical and textual information.

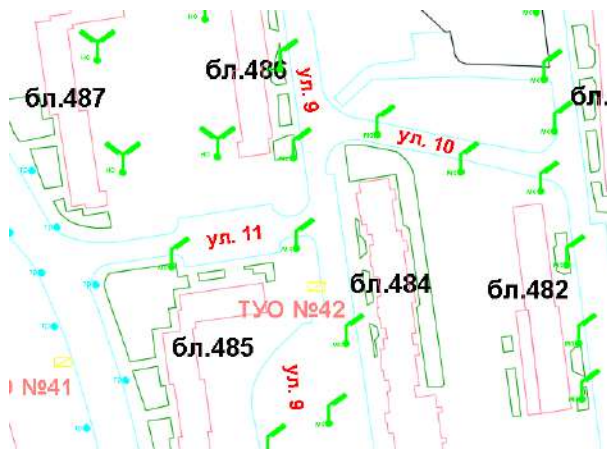


Fig. 3. Part of a digital model with locations of street lights and panel boards

As a result of the analysis of the electric energy research of street lighting, measures are proposed to improve energy efficiency. The first step is to prepare a lighting technical classification of the street network according to the new standard BS EN13201: 2016 [5].

Traffic on the streets is mainly by motor vehicles. Table 3 presents the light-technical categorization of streets. The classification of the streets in the residential district divides them into the following lighting classes: M3 - main streets (1 pc); M4 - regional arteries (9 pcs); M5 - local streets (16 pcs) and M6 - service streets (56 pcs).

Energy efficiency measures include the introduction of LED lights to replace existing street lamps with 150W, 100W, 70W and 50W LVLs, or in places with existing pillars but missing luminaires, new ones to be installed.

Table 3. Normal indicators for different road classes

Road categorization	Illuminance class	Indicators				
		Lcp, cd/m ²	Uo (min)	U1 (min)	TI, %	SR (min)
Main streets	M3	1	0.4	0.6	15	0.3
Regional arteries	M4	0.75	0.4	0.6	15	0.3
Local streets	M5	0.5	0.35	0.4	15	0.3
Service streets	M6	0.3	0.35	0.4	20	0.3

RESULTS AND DISCUSSION

Lighting calculations were performed for the different street categories, further divided by the road width, poles arrangement, and pole distance in view of the existing conditions.

The calculations were performed with street LEDs with an asymmetric light distribution curve (Fig. 4). Table 4 shows the parameters of the LED luminaires.



Fig. 4. LED street luminaire

Table 4. LED luminaires

Power, W	Color temperature, K	Luminous, Lm	Ra (CRI)	Curve, °	Voltage, V	IP
19,6	3000/4000	3038	≥70	67	160÷260	65
26,6	3000/4000	4123	≥70	67	160÷260	65
39,6	3000/4000	6138	≥70	67	160÷260	65
54	3000/4000	8370	≥70	67	160÷260	65
80	3000/4000	12403	≥70	67	160÷260	65

The calculation results are shown in Table 5, in compliance with BS EN13201: 2016.

Table 6 shows the types of LED lights, their parameters and how they are installed for the different street classes.

Table 5. Indicators for different street classes implemented with new street LED luminaires

N	Street category	Illuminance class	Indicators				
			Lcp, cd/m2	Uo, (min)	U1, (min)	TI, %	SR, (min)
A	Main streets	M3	1.26	0.85	0.84	9	0.53
A	Regional arteries	M4	0.76	0.43	0.84	8	0.53
B	Regional arteries	M4	0.91	0.79	0.88	8	0.51
A	Local streets	M5	0.57	0.44	0.90	6	0.53
B	Local streets	M5	0.64	0.74	0.85	5	0.76
C	Local streets	M5	0.54	0.66	0.86	6	0.62
A	Service streets	M6	0.33	0.47	0.76	8	0.44
B	Service streets	M6	0.34	0.67	0.92	7	0.7

Table 6. LED street lighting by averages

№	Road Category	Poles arrangement	Roadway width	Sidewalk width	Pole distance	Light Centre high	Boom angle	Power, W	Luminaire
			m	m					
A	Main	two - sided	16	2,5	35	12	0	80	LED
A	Regional	one – sided	14	2,5	30	9	0	80	LED
B	Regional	two - sided	17,5	3	30	12	0	54	LED
A	Local	one – sided	14	3	30	9	0	54	LED
B	Local	one – sided	7	2,5	25	12	0	39,6	LED
C	Local	one – sided	7	2,5	25	9	0	26,6	LED
A	Service	one – sided	10	2,5	35	9	0	26,6	LED
B	Service	one – sided	6	2,5	30	9	0	19,6	LED

Table 7. Type, number and power of new luminaires

Luminaires	Power, W	Number
LED road luminaire	19,6	530
LED road luminaire	26,6	269
LED road luminaire	39,6	96
LED road luminaire	54	181
LED road luminaire	80	314

The summarized number, type and capacity of the proposal for upgrading street lighting are presented in Table 7.

On the basis of the cadastral plan of the existing lighting system, a new one was developed, detailing the type of the grid, power lines and feeders. Appropriate graphic symbols indicate the different types of LED luminaires, the type of poles and the location of street PB.

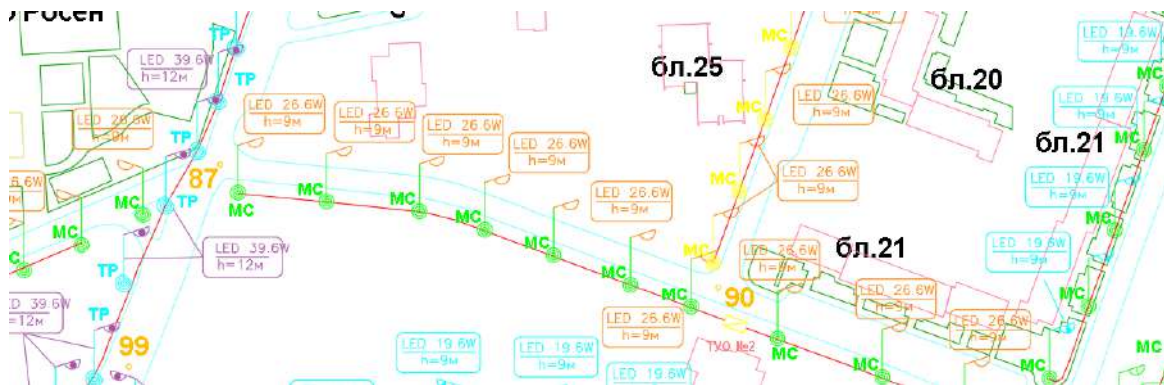


Fig. 4. Part of the new digital model with locations of street LEDs

The second major energy saving measure is the introduction of an intelligent street lighting control and management system. The construction of such a system increases the quality and reliability of street lighting and reduces the ongoing costs of electricity and maintenance. Widely used in the city of Burgas is a system with autonomous programmable controllers type AMC 190 (G) with built-in GSM GPRS modem for communication and a server in a central control room for monitoring and control. One or more “Matrix” meters are connected to each controller to measure the parameters of the electrical network.

The controllers can autonomously control the street lighting according to a predetermined task taking into account environmental factors. They allow the MA to be controlled by: pre-schedule, sunrise and sunset at the current date, by illumination using an analog light sensor or an external clock. They also allow for manual control of the CDD system. The proven system has a relatively low initial capital investment and is easy to maintain.

For the implementation of the system in different variants of management, it is necessary to choose luminaires with the necessary functionality for control (dimming), which also depends on the initial investment for the reconstruction of all MA cassettes in the residential district and connecting them to the already built such system in parts of Burgas.

The presented energy efficiency research of the studied street lighting system is an example of the transition from conventional lighting to LED lighting.

The total installed power of the existing lighting system is 263kW. For an average annual usage of 4000 hours, this equals 1055 417kWh of electricity consumed.

The total power of the LED luminaires is 51kW. For 4000 hours average annual usage this equals 204 000kWh of electricity consumed. This is five times less power with LED lighting and five times less power consumption.

The technical results correspond to the current regulations in Bulgaria and represent an up-to date technical solution for the modernization of street lighting in order to improve the energy its efficiency of street lighting.

ACKNOWLEDGMENTS:

The author is grateful to the Scientific and Research Sector “Scientific and artistic-creative activities” at University “Prof. Assen Zlatarov”-Burgas, for funding the research through contract No NIH - 427/2019.

REFERENCES

1. Tzankov P., M. Jovchev, H. Ibrishimov, Tz. Petkov, E. Stanev and L. Dimitrov, *Electrical energy research of street lighting in Gabrovo*, Proceedings of the National Lighting Conference for Young Scientists, Lighting 2016, 21 – 23 October, Sofia, Bulgaria.
2. Ashryatov A., *Improving the efficiency of existing lighting systems*, Proceedings of the National Lighting Conference for Young Scientists, Lighting 2016, 21 – 23 October, Sofia, Bulgaria.
3. Van Tichelen P., T. Geerken, J. B. Vanden Bosch, M. Laborelec, V. Van Hoof, L. Vanhooydonck, A. Vercalsteren, *City of San Josse Public Strreetlight Design Guide*, USA, 2011, “Final Report Lot 9: Public street lighting”, 2007/ETE/R/021.
4. BS EN 13201:2016. Street lighting. Part 1-5.

LABORATORY MODEL FOR COMPENSATION OF REACTIVE POWER

Mladen Proykov
E-mail: m_proykov@abv.bg

ABSTRACT

A laboratory model for reactive power compensation was made. The benefits of reactive power compensation were examined. The possible occurrence of resonance phenomena was investigated.

Key words: reactive power compensation, resonance.

INTRODUCTION

Reactive power is used to generate electromagnetic fields in electrical machines. Its transmission through the electricity network is associated with a number of negative consequences, such as increased losses via the transmission facilities. Reactive power is a reason for underutilization of synchronous generators as it overloads them. Its circulation through the elements of the electricity system causes losses of active power. The huge amounts of inductive loads on the network have enormous jet power that circulates between generators and consumers without doing any useful work.

Reactive power compensation (RPC) has a direct effect on the quality of electricity and the improvement of the efficiency of the electricity supply systems. This requires technical and organizational measures to be taken.

Transformers, asynchronous motors (AM), induction furnaces and other devices, which may be called "inductive loads", are the main consumers of reactive energy and degrade $\cos\varphi$ [1].

THEORETICAL

The following quantities are used to quantify the relationship between active and reactive power [2, 3]:

Instantaneous value of $\cos\varphi$:

$$\cos\varphi(t) = \frac{P(t)}{S(t)} = \frac{P(t)}{\sqrt{P^2(t) + Q^2(t)}} \quad (1)$$

Average value of $\cos\varphi$ for time interval T:

$$\cos\varphi_{cp.} = \frac{1}{\sqrt{1 + \left(\frac{W_p}{W}\right)^2}}; \quad tg\phi_{cp.} = \frac{W_p}{W} \quad (2)$$

Natural $\cos\varphi$ is the value of $\cos\varphi$ for a group of consumers without considering the performance of the compensation devices:

$$\cos\varphi_e = \cos\left(\arctg\frac{Q}{P}\right) = \frac{P}{\sqrt{P^2 + Q^2}} \quad (3)$$

Actual $\cos\varphi$ is when the reactive power of the consumers and of the compensation systems (CS) are taken into account:

$$\cos\varphi_{\Delta} = \cos\left(\arctg\frac{Q - Q_K}{P}\right) \quad (4)$$

Rate of reactive power compensation [1]:

$$C_K = \frac{Q_K}{Q} \quad (5)$$

Power supply system (PSS) saturation with compensating capacities takes into account the need for compensating power:

$$H = \frac{Q_K}{P_M} \quad (6)$$

Adverse situations of low $\cos\varphi$ are expressed in:

- The useful active power "P" of the generators is reduced;
- The throughput of the transformers is reduced;
- Additional losses of active power and energy occur in the power supply system;
- Reducing $\cos\varphi$ results in an increase in the current in the grids;
- Increased voltage losses at low $\cos\varphi$;

This can be disadvantageous for many consumers, such as asynchronous motors, light sources, induction furnaces, welding units etc.

The aforementioned disadvantages of low $\cos\varphi$ require measures to be taken regarding the

power supply system of the facilities to improve it. These activities are carried out in two directions: improvement of $\cos\varphi$ without compensating devices (natural modes) and use of CS (artificial modes).

The improvement of $\cos\varphi$ without compensating devices is accomplished in the following ways:

- The right choice of electrical equipment during design;
- Arrangement of the technological process in order to improve the energy regime of the facilities;
- Using synchronous motors (SM) instead of asynchronous motors of the same power when the technological process allows and is economically feasible;
- Replacement of low load asynchronous motors with lower power engines;
- Reducing the voltage;
- Limiting the idle time of electric motors;
- Quality repair of electric motors;
- Reduction of reactive power consumption of transformers.

In most cases it is not possible to achieve the desired increase in $\cos\varphi$ by the "natural" methods described above. It may then be technically and economically feasible to use compensation devices to improve $\cos\varphi$, namely:

- Static compensation devices: power capacitors, reactors and thyristor-controlled capacitors and reactors;
- Dynamically compensating devices: synchronous motors, synchronized asynchronous motors, compensating converters, synchronous (AC) and asynchronous (AC) compensators, etc.;
- Modern solutions for reactive power compensation based on flexible DC systems (Fig. 1).

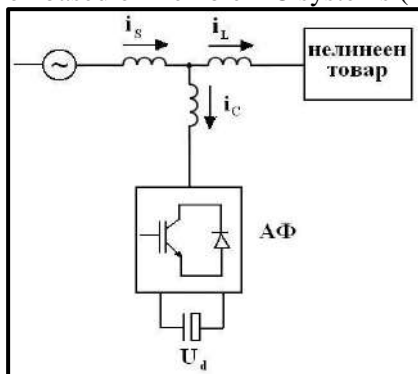


Fig. 1. Active filter for reactive power compensation

The determination of the required compensating power is carried out in accordance with the vector diagram in Fig. 2. and formula (7):

$$Q_K = k \cdot P_{CP} \cdot (\operatorname{tg}\varphi_E - \operatorname{tg}\varphi_{Ж}) \quad (7)$$

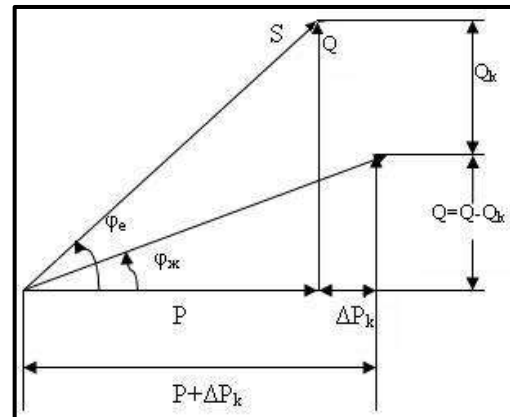


Fig. 2. Vector diagram of active, reactive and total power

Compensating power management is regulated in view of:

- improving the quality of the voltage;
- management of reactive loads in the electricity system and reduction of power and energy losses;
- optimized utilization of installed compensating powers;
- reducing the current load of power system elements of the facilities.

With the continuous increase in the capacity of installed capacitors in industrial plants, it is becoming more and more urgent and necessary to regulate their capacity. Compensation power regulation can be manual, dispatcher or automatic.

- Manual regulation is performed by the duty staff.
- Dispatching regulation is carried out by a dispatching point.
- Automatic regulation.

The reactive power compensation effect can increase the efficiency of the transformer power, reduce the losses in the power lines and improve the quality of the voltage, which leads to increased economic and social benefits. A particularly great effect is achieved through the implementation of an automatic reactive power compensation, which leads to optimization of the compensating power control scheme, reduction of the time for switching the compensating power on and off, precise control of the compensating power and, accordingly, maintaining the desired $\cos\varphi$ more precisely [4].

Controllers used for automatic power compensation make a direct analysis of current and

voltage harmonics up to the 19th harmonic. The maximum value is stored in their memory, the total coefficients of harmonic current and voltage distortions are calculated. If the distortion is greater than the predetermined current, all stages of the capacitor battery are disconnected from the controller and an alarm is activated.

The use of a quality controller with good software that also performs protective functions can significantly extend the life of capacitors. The controller effectively protects them from rising and falling mains voltage, frequent starts and even against resonance [5].

RESEARCH

A laboratory model for automatic reactive power compensation based on transverse compensation has been implemented. It can visually simulate the benefits of implementing transverse compensation in an electrical system and capture

electrical parameters (current, voltage and $\cos\phi$) before and after compensation (Fig. 3).



Fig. 3. Laboratory model

Fig. 4 shows the circuit diagram of the laboratory model.

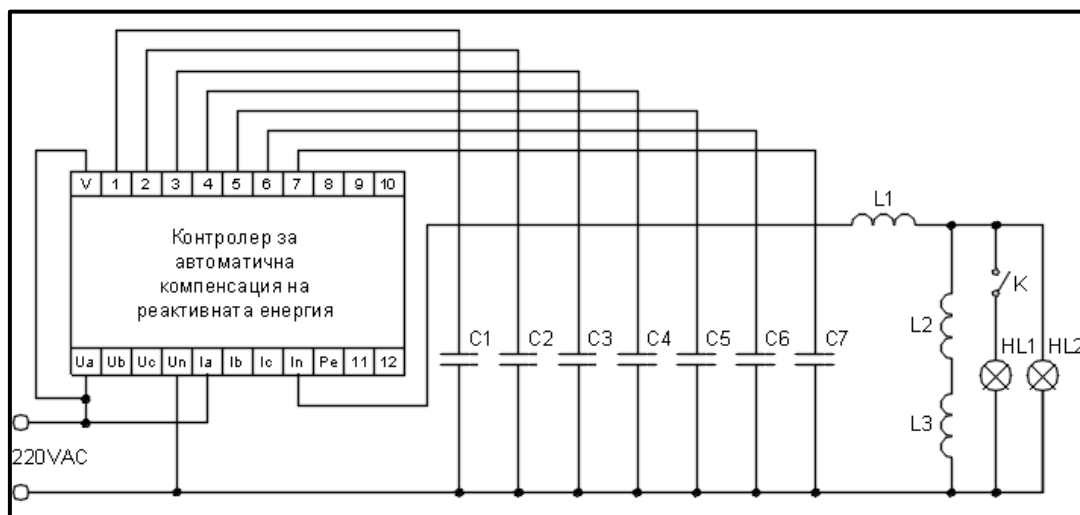


Fig. 4. Circuit diagram of the laboratory model

Description of the laboratory model:

- L_1 ; L_2 and L_3 are throttles for high pressure sodium lamps with nominal data: $U_n = 220\text{VAC}$; $L = 230\text{mH}$; $f = 50\text{Hz}$; $I_n = 1\text{A}$;

- C_1 is a capacitor with nominal data: $C_n = 0,4\mu\text{F}$; $U_n = 220\text{VAC}$;

- C_2 and C_3 are capacitors with nominal data: $C_n = 2,5\mu\text{F}$; $U_n = 220\text{VAC}$;

- C_4 and C_5 are capacitors with nominal data: $C_n = 2\mu\text{F}$; $U_n = 450\text{VAC}$;

- C_6 and C_7 are capacitors with nominal data: $C_n = 0,5\mu\text{F}$; $U_n = 450\text{VAC}$;

- Q is circuit breaker: number of poles = 2; $I_n = 6\text{A}$;

- JKL is a controller for reactive power compensation;

- $HL1$ and $HL2$ are light bulbs: $P_n = 100\text{W}$; $U_n = 220\text{VAC}$;

The Reactive power compensation controller (Fig. 5) is a standalone device for automatic/manual control of capacitor batteries in single-phase and three-phase networks. It has installed filters for harmonic components of voltage and current, which is why it is characterized by high precision and precision of reactive power control.

- $\cos\varphi$ must be equal to $\cos\varphi$ (d);
- Determination of the capacitive power included by the controller (formula 13):

$$Q'_{kb} = \varpi \cdot C'_k \cdot U^2 \quad (13)$$

- Determination of the power supply system saturation with compensating capacities (formula 13):

$$H = \frac{Q'_{kb}}{P} \% \quad (14)$$

Determination of the rate of reactive power compensation:

$$C_K = \frac{Q'_{kb}}{Q} \% \quad (15)$$

Determining the economic impact of reactive power compensation:

- Reported current in the circuit after the reactive power compensation is $I' = 0,39\text{mA}$;
- Reactive power after compensation is defined by formula (16):

$$Q' = U \cdot I' \cdot \sin\varphi \quad (\text{ж}) \quad (16)$$

where $\sin\varphi$ (d) = 0,392 according to $\cos\varphi$ (d) = 0,92.

- The active “P” and full “S” powers in circuit diagram after compensation are defined by formulas 14 and 18:

$$P' = U \cdot I' \cdot \cos\varphi \quad (\text{ж}) \quad (17)$$

$$S' = \sqrt{P'^2 + (Q')^2} \quad (18)$$

- The amount of compensated total power “S” in the electrical circuit after the compensation is:

$$\Delta S = S - S' \quad (19)$$

Table 2 shows the individual steps of the controller work during compensation and Table 3 shows the final results of the study.

Table 2. Circuit parameters during automatic reactive power compensation

I', A	$C'_{kb}, \mu\text{F}$	Step number	$\cos\varphi'$	I', A	$C'_{kb}, \mu\text{F}$	СТЪПКИ N	$\cos\varphi'$
0,66	0	1	0,53	0,37	6,5	8	0,96
0,64	0,4	2	0,55	0,45	4	9	0,78
0,51	2,9	3	0,69	0,43	4,5	10	0,82
0,4	5,4	4	0,88	0,41	5	11	0,86
0,35	7,4	5	0,98	0,4	5,4	12	0,89
0,37	7	6	0,97	0,36	7,9	13	0,99
0,43	4,5	7	0,82	0,39	5,9	14	0,92

Table 3. Circuit parameters after reactive power compensation

I', A	U, V	$C'_{kb}, \mu\text{F}$	P', W	$Q_{к6}, \text{Var}$	Q', Var	S', VA	$\Delta S, \text{VA}$	$\cos\varphi'$	H, %	$C_K, \%$
0,39	235	5,9	82,2	102,3	35,9	89,7	65,4	0,92	124,5	77,8

In electrical circuits containing L and C elements, resonance phenomena can occur when equalizing the inductive X_L and capacitive X_C resistances in the circuit. For the circuit in Fig. 8, there are conditions for a consistent resonance between the equivalent inductance L_{eKB} and equivalent capacity C_{eKB} .

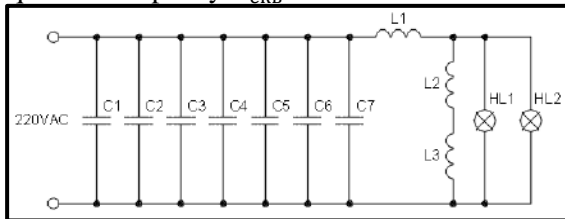


Fig. 8. Resonance $L_{\text{eKB}} - C_{\text{eKB}}$ circuit

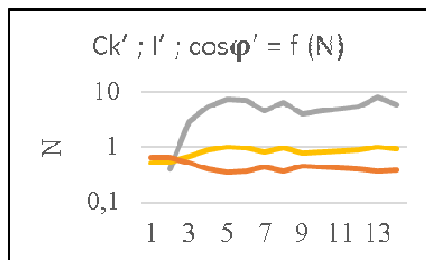
The equivalent inductance measured with the LCR meter is $L_{\text{eq}} = 1,34\text{H}$. The value of the capacitance at which a resonance can occur are determined by formula 20:

$$X_L = X_C; \quad \omega \cdot L = \omega \cdot C; \quad C = \frac{1}{\omega^2 \cdot L_{\text{eq}}} \quad (20)$$

$$C = \frac{1}{314^2 \cdot 1,337} = 7,6 \mu\text{F}$$

The test shows that values of $C_{\text{eq}} = 7,6\mu\text{F}$, should be avoided due to conditions for the occurrence of consistent resonance and a sharp increase of current in the electrical circuit.

The diagram in Fig. 9 shows alteration of: C'_{kb} ; I' ; $\cos\varphi' = f(N)$



RESULTS AND DISCUSSION

The work of an automatic reactive power compensator was investigated.

After applying a transverse reactive power compensation, $\cos\varphi$ increased from 0,53 to 0,92. This measure leads to unloading the electrical circuit from the transfer of reactive power “Q”.

As $\cos\varphi$ increases to the value of 0,92, the total current in the circuit decreases 1,7 times, the total power “S” decreases 2,37 times and the reactive power “Q” decreases 3,66 times.

The reduction of the current in the circuit makes it possible to choose electrical equipment

with fewer parameters, cables/wires with smaller sections, which is cost-effective. It also leads to a decrease of active energy consumption due to a reduction in active losses in wires and equipment.

REFERENCES

1. KarafeizovTz., *Reactive power transmission in power lines*, Energetika 2003;
2. Kirov M., Reactive cargo compensation, an effective way for saving electrical power, *Energy forum*, Proceedings, 2006;
3. Kirov M., *Optimization of reactive power compensation, performance by synchronous motors and capacitors in the power supplying systems of powerful industrial facilities*, ELMA, 2011.
4. Baev D., *A guide to enterprise energy efficiency management*, Sofia, 2015;
5. Gotman I., Criteria for evaluation of reactive power compensation, *Electricity*, 2009;

COMBINED ROAD AND RAILWAY TRANSPORT IN PRESENT-DAY BULGARIA

Vasil Bobev

E-mail: v_bobev@yahoo.com

ABSTRACT

Combined transport is a highly-efficient technology aimed to optimally use different types of transport. The peculiarity of combined transport is the combination of the advantages of the different kinds of transport participating in haulage and their complementarities. The present paper describes the process of Ro-La traffic. A model for the transportation of vehicles with railway transport from Plovdiv intermodal terminal has been developed.

Key words: road transport; rail transport; combined transport.

INTRODUCTION

As is known, combined goods transport is a highly-efficient technology aimed to optimally use different types of transport. The organization of work at the terminals and vehicle-carrying ferries is the major factor influencing the efficiency of the whole transport process [1].

Combined transport allows increasing the efficiency of goods transportation. The peculiarity of combined transport is the combination of the advantages of all kinds of transport participating in haulage and their complementarities. In this way the infrastructure is used optimally and a high quality of offering transport product is achieved [2].

In [1] the process of the ferry traffic is presented. The evaluations corresponding to the ferry traffic make use of the theory of intuitionistic fuzzy sets. Ferry transport is the transport of vehicles, persons and goods across a river, lake or sea. This is a combined technology with horizontal transfer of transport. In this case the standard combined unit is a vehicle.

The characteristics of this combined transport result from the fact that the vehicles move in shorter intervals. This is due to the fact that there are a lot of means of transport.

In [2] the process of Ro-Ro traffic is described. Ro-Ro is a combined technology with a horizontal transfer of transport. In this case the standard combined unit is a vehicle: a lorry with a trailer or only trailers. The ships have two or more decks. Vehicles are driven on and off the ship on their own wheels and cabins are available for the drivers. Ro-Ro combined technology is not being developed in Bulgaria these days.

Combined road and railway transport is the loading and railroading of vehicles (lorries with

trailers or only trailers) by trains. In practice they are called Ro-La trains. In this case the major advantages of railway transport, such as ecology, safety and big haulage capacity, are used.

This kind of combined transport to a great degree combines the efficiency of railway transport in haulage of the mass goods on a long distance with the indisputable priority of road transport on short distances and potentiality for direct delivery of goods to customers. The development of combined transport has and continues looking for new possibilities to solve transport problems, such as traffic congestion, road accidents, pollution, etc.

Regular connections with such trains exist between different countries in Europe. There are such connections between Hungary and Austria, Romania and Austria, Slovenia and Austria, the Czech Republic and Germany, etc.

Nowadays, trains run on fixed schedules, e.g. fixed day of the week and departure time. The requirements for lorries are: to have a reservation in advance, to arrive at the terminal by the specified time before departure and to meet technical standards (weight and overall dimensions) [3].

EXPERIMENTAL

In Bulgaria there are a lot of conditions for the development of combined road and railway transport. These are good transit car traffic and good advanced combined transport. Unfortunately, only this technology is being developed in Bulgaria now, and only as the internal technology transport of a private company.

The Bulgarian government granted a 27-year-long concession to the Terminali Company for the intermodal terminal in Plovdiv in the South

Central Planning Region of Bulgaria. Terminali is solely owned by PIMK, the country's largest carrier company. The company, together with DB Schenker, transports goods from Rousse. Recently, it has invested in its own railway company, PIMK Rail and is licensed as a rail carrier.

Now the company transports trailers by train between Plovdiv (BG) and Cherkezköy (TR). The train has a capacity of 34 carriages. The initial schedule is the following (Fig. 1):

BG (Friday) →→→→→**TR(Saturday)**
TR(Saturday)→→ →→→ **BG(Sunday)**

Fig. 1

The train will start every Friday from the intermodal terminal near Plovdiv. On Saturday, the train will be unloaded in Turkey. On the same day the train will go back to Bulgaria and on Sunday it will be back at the terminal in Plovdiv.

There is a timetable for trains to move between Bulgaria and Turkey twice a week. In this way, they will also carry trailers to other carriers, most often Turkish (Option II).

In [3] the model describing the process of Ro-La floats is presented. The Generalized Net model described in [3] is a possible model for the process of Ro-La traffic. In this case, the actual process is easier to describe.

RESULTS AND DISCUSSION

Based on these, a model about a specific timetable has been designed by the author. This model has a limit based on the number of carriages in every train. The number of carriages is equal to the number of vehicles.

In this case it is possible to optimize the train timetable. The aim is to ensure the transport of more trailers. This improves the ability to transport trailers owned by other carriers (Option III). In this case, the timetable is as shown in Fig. 2.

BG (Friday) →→→→→**TR(Saturday)**
TR(Saturday)→→ →→→ **BG(Sunday)**

BG (Sunday) →→→→→**TR(Monday)**
TR(Monday)→→ →→→ **BG(Thursday)**

BG (Thursday) →→→→→**TR(Wednesday)**
TR(Wednesday)→→ →→→ **BG(Thursday)**

Fig. 2

The number of vehicles in this case is shown in Fig. 3.

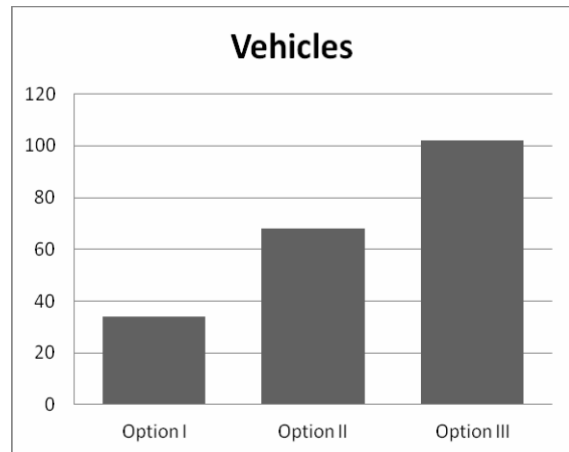


Fig. 3

This allows for up to 68 vehicles/trailers (Option II) or 102 vehicles/trailers (Option III) to be carried between Bulgaria and Turkey in every direction every week.

In general, this means 204 trucks fewer on the roads between Bulgaria and Turkey every week.

The future plans of the company envisage the launch of another train from the intermodal terminal in Plovdiv to Austria. The difference is that it can be up to 30 carriages long, because it will pass through Serbia, where there are limitations on the length of the train. The journey will be about three days for each direction or about a week to complete the entire turnover.

This means 60 trucks fewer on the roads between Bulgaria and Austria and transit countries every week and decreased costs for carriers in the future.

CONCLUSIONS

The presented results can be used to create a methodology for future plans of the company to envisage the launch of another train from Plovdiv to Austria.

Thus, the major advantages of the railway transport, such as ecology, safety and big haulage capacity, appear in practice.

Most of the model parameters can also be regarded as characteristics of tokens from an additional contour, thus achieving optimization with respect to our given aim.

Statistical information needs to be collected in order to monitor the development of the process.

REFERENCES

1. Bobev V., S. Sotirov, Generalized net model of the auto ferry traffic, using intuitionistic fuzzy estimations, *Notes on Intuitionistic Fuzzy Sets*, Sofia, 14-15 May 2008, ISSN 1310-4926, p. 108-112;
2. Sotirov S., Bobev V., Generalized net model of the Ro-Ro traffic, *Issue on Intuitionistic Fuzzy Sets and Generalized nets*, Warszawa, 2008, ISBN 978-83-60434-58-1, p.155-160;
3. Bobev V., S. Sotirov, Generalized net model of combined transport between road and railway transport, *Developments in Fuzzy Sets, Intuitionistic Fuzzy Sets, Generalized Nets and Related Topics*. Volume II: Applications, Polish Academy of Sciences, Warszawa, 2010, ISBN 9788389475305, p. 25-30.

MODELING OF TRANSIENT PROCESSES IN A LINEAR ELECTRIC CIRCUIT OF THE SECOND ORDER WITH A GENERALIZED NET

Yuliy Petrov
E-mail: yulipetrov@mail.bg

ABSTRACT

This article presents a method for modeling of transient processes in linear electrical circuits of the second order with generalized nets. During the analysis we applied not only the Ohm and Kirchoff's laws but also generalized methods. For modeling and describing the apparatus of generalized nets is used, including the whole algorithm of the realization of every single step of the algorithm and there are also foreseen possible exits and rules for making decisions. Generalized nets are one of the best-known techniques for describing processes in a formal and abstract way.

Key words: linear electrical circuits, second order, generalized nets, algorithm, Ohm, Kirchoff

INTRODUCTION

When a circuit containing coils and capacitors passes from one mode to another, transitional processes occur (Fig.1). The event triggering this process is called commutation, and the moment when it happens is assumed to be 0. The transition process does not take place instantly because there is an electromagnetic energy stored in the circuit. Theoretically, this process continues indefinitely, but, practically, it happens very quickly. The analysis of these processes follows a certain algorithm that can be modeled using generalized networks.

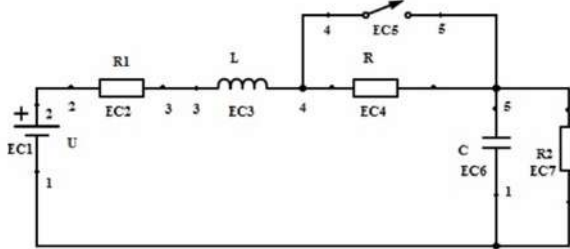


Fig. 1. Electrical circuit

Generalized networks use a formal algorithm description and they are a technique for describing processes using a high degree of abstraction and intuitiveness [3 - 6]. Such an approach allows to exclude the ambiguity in the semantics of the individual instances representing separate semantic units in the presented model. The result of this type of modeling is generating an abstract generalized network, giving the opportunity for unimpeded implementation in program environments.

The article examines the general structure for describing the classical method for the analysis of transitional processes through the generalized network model for the following diagram (Fig. 2). The methodology for building generalized networks involves constructing the static structure of the modeling process, reflecting the dynamics of the model process, describing the functioning of the modeling process over time, identifying the data that are of interest to the modeling process.

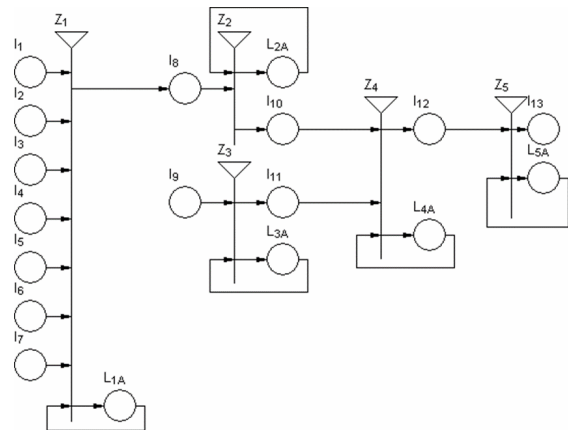


Fig. 2 Generalized network model

GENERALIZED NET MODEL

A generalized network model has been developed with an entered multitude of transitions A which:

$$A = \{Z_1, Z_2, Z_3, Z_4, Z_5\},$$

where the transitions describe the following processes:

Z_1 ="Building a circuit";
 Z_2 ="Independent initial conditions (before commutation)";
 Z_3 ="Linear differential equation system (after commutation)";
 Z_4 ="System of equations with state variables";
 Z_5 ="Determination of transition values".

A) Transition Z_1

Transition Z_1 has the following description:

$$Z_1 = \langle \{l_1, l_2, l_3, l_4, l_5, l_6, l_7, L_{1A}\}, \{l_8, L_{1A}\}, r_1, \vee (l_1, l_2, l_3, l_4, l_5, l_6, l_7, L_{1A}) \rangle$$

where:

	l_8	L_{1A}
$r_1 = l_1$	false	true
l_2	false	true
l_3	false	true
l_4	false	true
l_5	false	true
l_6	false	true
l_7	false	true
L_{1A}	$W_{1A,8}$	true

$W_{1A,8}$ = "all entrance levels are available"

Transition Z_1 consists of seven entrances $l_1, l_2, l_3, l_4, l_5, l_6, l_7$ and one exit l_8 . Entranced kernels from positions $l_1, l_2, l_3, l_4, l_5, l_6, l_7$ come with the following initial features [6]:

$$l_1 = \langle EC1, 1, 2, "DC\ voltage", U \rangle,$$

$$l_2 = \langle EC2, 2, 3, "Resistive", R1 \rangle,$$

$$l_3 = \langle EC3, 3, 4, "Inductive", L \rangle,$$

$$l_4 = \langle EC4, 4, 5, "Resistive", R \rangle,$$

$$l_5 = \langle EC5, 4, 5, "Switch", K \rangle,$$

$$l_6 = \langle EC6, 5, 1, "Capacitive", C \rangle,$$

$$l_7 = \langle EC7, 5, 1, "Resistive", R2 \rangle.$$

After transition Z_1 , the entered kernels from $l_1, l_2, l_3, l_4, l_5, l_6, l_7$ are united into the exit kernel l_8 to subsequently simulate the process. After the

transition, kernel l_8 receives the feature "designed modeling scheme".

B) Transition Z_2

Transition Z_2 has the following description:

$$Z_2 = \langle \{l_8, L_{2A}\}, \{l_{10}, L_{2A}\}, r_2, \vee (l_8, L_{2A}) \rangle$$

where:

	l_{10}	L_{2A}
$r_2 = l_8$	false	true
L_{2A}	$W_{2A,10}$	true

$W_{2A,10}$ = "there are independent initial conditions before commutation"

The entrance kernel of position l_8 receives a characteristic: "modeling pattern" in L_{2A} , after the Z_2 transition, kernel l_{10} receives a new characteristic "independent startup".

C) Transition Z_3

Transition Z_3 has the following description:

$$Z_3 = \langle \{l_9, L_{3A}\}, \{l_{11}, L_{3A}\}, r_3, \vee (l_9, L_{3A}) \rangle$$

where:

	l_{11}	L_{3A}
$r_3 = l_9$	false	true
L_{3A}	$W_{3A,11}$	true

$W_{3A,11}$ = "a system of differential equations is available".

Transition Z_3 consists of one entrance l_9 and one exit l_{11} . The entrance kernel from position l_9 enters with the "initial data" characteristic in L_{3A} ; after the transition Z_3 , kernel l_{11} receives a characteristic "a system of differential equations".

D) Transition Z_4

Transition Z_4 has the following description:

$$Z_4 = \langle \{l_{10}, l_{11}, L_{4A}\}, \{l_{12}, L_{4A}\}, r_4, \vee (l_{10}, l_{11}, L_{2A}) \rangle$$

where:

CONCLUSIONS

The model allows to examine different stages of the process of modeling transition processes, as well as its simulation and behavior. The transition process study program includes monitoring the change of transitional quantity over time, examining the impact of chain parameters on the character and speed of the transitional process, and also the ability to determine some parameters of the chain based on received images.

The created mathematical model aims to show a different approach for laboratory practice. The results obtained from the simulation can be compared with the results obtained in a laboratory environment with actually connected chain. Their implementation supports the development of logical and algorithmic thinking, enables mastery of the basic methods of research and analysis of assigned tasks, and self-improvement of technical knowledge and finding rational solutions.

ACKNOWLEDGMENT

This work was supported by the Bulgarian Ministry of Education and Science under the National Research Programme “Young scientists and postdoctoral students”, approved with DCM #577/17.08.2018.

REFERENCES

1. Mechkova V, L. Staneva, B. Mechkov, Mathematical models for examination of transients processes in electric circuits of second order, *Industrial technologies*, vol.II (1), Burgas, cc 17 – 20, 2015
2. Mechkova V, L. Staneva, B. Mechkov, „Razrabotka cikla laboratornax rabot po kursu “Teoreticheskaya electrotehnika“ v srede MATLAB“, *Sbornik nauchnax trudov XI megdunarodnoy nauchno – tehniceskoy konferencii „Problema i perspektiva razvitiya otechestvenoy svetotekhniki, electrotehniki I energetiki“*, Saransk, 2013, c. 392–396;
3. I. Vardeva, V. Gochev, Calculation of estimations of messages by generalized nets and intuitionistic fuzzy truth values, *IEEE 6th International Conference “Intelligent Systems”*, 2012
4. I. Vardeva Generalized net model for building a virtual private dial-up network, *Issues in IFSS and GN*, Vol.9 (2011), pp.70 - 76
5. Gocheva P., N. Hinov, V. Gochev. Generalized net based estimations on switching topologies in electronic circuits, *AIP Conference Proceedings 2048*, 060025 – pp.1-6 (2018)
6. P.Gocheva, N. Hinov, V. Gochev, Modeling of Electronic Circuits with Generalized Nets, 2018 *IX National Conference with International Participation (ELECTRONICA)*, DOI:10.1109

NOVEL MG-CONTAINING GLASS-CERAMICS IN THE SiO₂-CaO SYSTEM AND THEIR IN VITRO BIOACTIVITY: XRD, FTIR, SEM AND ICP-AES ANALYSIS

Lachezar Radev
E-mail: l_radev@abv.bg

ABSTRACT

Novel Mg-containing glass ceramics in SiO₂-CaO system were prepared via sol-gel method. The obtained dried gels were thermally treated at different temperatures. The structure of the samples obtained were characterized by XRD and FTIR, and the concentrations of Ca²⁺, Mg²⁺, Si⁴⁺ and P⁵⁺ after in vitro test in SBF were studied by ICP-AES technique. XRD of the thermally treated samples proved the presence of the main phase of merwinite accompanied with akermanite or akermanite and bredigite. FTIR of the thermal treated samples confirmed XRD results. FTIR of the samples after in vitro test in SBF solution revealed that CO₃HA was formed on the soaked samples in static conditions. The obtained FTIR results are in a good agreement with XRD. ICP-AES showed that the precipitation was similar for the two prepared glass ceramics. SEM revealed the presence of HA on the soaked surface. Based on these results, it can be concluded that the Mg-containing glass ceramics in the SiO₂-CaO system are in vitro bioactive.

Key words: merwinite, akermanite, bredigite, glass ceramics, in vitro bioactivity

INTRODUCTION

Hydroxyapatite (Ca₁₀(PO₄)₆(OH)₂, HA) and β-tricalciumphosphate (β-Ca₃PO₄, β-TCP) have been considered the most promising materials for both dental and orthopaedic applications because of their chemical similarity to that of human hard tissue [1]. It is known that their applications are limited due to some disadvantages. For example, HA shows a limited ability to stimulate the development of new bone tissue and does not significantly degrade over time [2].

On the other hand, biological HA structures and their properties, such as bioactivity, biocompatibility, solubility, and absorption, can be improved by modifying their composition by ionic substitution processes, as described by W. Suchanek et al. [3]. Small quantities of cations (i.e. K⁺, Mg²⁺, Sr²⁺, Al³⁺) and/or anions (i.e. F⁻, SiO₄⁻ and CO₃²⁻) in the HA- structure can play a pivotal role in their overall biological performance, as can be seen in several studies [1, 2, 4-6].

Magnesium (Mg) is one of the most important mineral elements in the human body. Some studies have indicated that Mg²⁺ has a key role in bone remodelling and skeletal development [7, 8]. A brilliant review on Mg-containing sol-gel glasses and glass-ceramics was published by M. Diba and co-workers [9].

In recent decades, pure and multiphase glass-ceramics in CaO-SiO₂-MgO system have been of particular interest for biomedical applications. Pure crystalline phases, such as akermanite (Ca₂MgSi₂O₇, Ak) [10-14], diopside (CaMgSi₂O₆, Di) [15-19], merwinite (Ca₃MgSi₂O₈, Merw) [20], and bredigite (Ca₇MgSi₄O₁₆, Bred) [15, 21-23] have been thoroughly investigated, respectively, showing that they possess good biological properties. Furthermore, all authors have reported that calcification temperature is an important factor for obtaining glass-ceramics.

A brief summary of previous studies of the polycrystalline Mg-containing glass-ceramics, including the composition of the gels, preparation methods, and crystalline phases observed, are given in Table 1, where W is wollastonite, PsW is pseudowollastonite, Cryst is crystoballite, Lar is larnite (dicalcium silicate), and Per is periclase.

The characteristics of the crystallization process in the CaO-MgO-SiO₂ system provide the synthesis of materials of an identical chemical but of a various phase composition and structure. The chemical composition corresponding to the stoichiometry of merwinite 3CaO.MgO.2SiO₂ is chosen. Merwinite ceramics have recently drawn attention, since they show not only mechanical

properties comparable to those of cortical bone, but also apatite forming ability in vitro and good in vivo biological properties [9].

This study is a continuation of our studies [34, 35], which described bioactive ceramics containing merwinite in the amount of 29% and 85%, respectively. It would be interesting to determine the effect of the phase composition on the in vitro bioactivity of the glass-ceramics. The

glass-ceramics studied have the same chemical composition but different phase composition due to different synthetic conditions. The objective of the present study is to determine the in vitro bioactivity of two glass ceramics of the CaO - MgO - SiO₂ system containing merwinite as the main crystal phase in the amount of 92% and 63%, respectively, and different additional phases.

Table 1. Summary of previous studies on the synthesis of Mg-containing glass-ceramics in CaO-SiO₂-MgO system with (or without) other components

Authors	Composition of the gel	Method	Temperature, °C	Phases	Ref.
D-M.Liu	54.5CaO-32.8SiO ₂ -6.1P ₂ O ₅ -6.0MgO-0.6CaF ₂ (mol.%)	Melting	930-1150	Ak, W, HA	[24]
R. Choudhary	akermanite	Sol-gel	900 1000 1200	Ak, Mer, Di Ak, Di Ak, Mer	[25]
J. Ma	28CaO-58SiO ₂ -10MgO-4P ₂ O ₅ (mol.%)	Sol-gel	900 1200	PsW, W, Ak Ak, Cryst	[26]
J. Ma	(38-x)CaO-xMgO-4P ₂ O ₅ -58SiO ₂ , where x=5,10,20 mol.% MgO	Sol-gel	1200	Ak, Cryst	[27]
J. Ma	(38-x)CaO-xMgO-4P ₂ O ₅ -58SiO ₂ , where x=5,10,20 mol.% MgO	Sol-gel	1200	Ak, Cryst	[28]
E. Bernardo	Akermanite with micro- and nanofillers of CaCO ₃ , MgO and Mg(OH) ₂	Oxidation decomposition of resins	900 1000	Ak Ak, Mer, W	[29]
X. Chen	Ak on Ti-6Al-4V alloy	Sol-gel, plasma spraying	650-800	W, Lar, Ak	[30]
X. Chen	40.18CaO-46.43SiO ₂ -13.39MgO (mol.%) 43.30CaO-45.98SiO ₂ -10.72MgO (mol.%) 45.98CaO-45.54SiO ₂ -8.48MgO (mol.%)	Sol-gel Sol-gel Sol-gel	1350 1320 1300	W, Ak, Lar	[31]
M. Zhang	49.13CaO-49.13 SiO ₂ -7.68MgO (wt.%)	Sol-gel	1300	Ak, W, Lar	[32]
O.-M. Goudouri	70SiO ₂ -20CaO-10MgO 70SiO ₂ -10CaO-20MgO 60SiO ₂ -30CaO-10MgO 50SiO ₂ -30CaO-20MgO	Sol-gel Sol-gel Sol-gel Sol-gel	810 850 1050 800 840 1050 810 850 1050 780 820 1050	amorphous Di Di amorphous Di Di amorphous Di, W, PsW Lar Lar, Di Di, Ak, Mer	[33]
I.Michailova	51.2 CaO-12.3MgO-35.5SiO ₂ (wt.%) 50.0 CaO-16.7MgO-33.3SiO ₂ (mol.%)	Sol-gel	1100	Lar, Mer, Ak, Per.	[34]
I.Michailova	51.2 CaO-12.3MgO-35.5SiO ₂ (wt.%) 50.0 CaO-16.7MgO-33.3SiO ₂ (mol.%)	Sol-gel	1300	Mer, Ak	[35]
L. Radev	46.7CaO-34.2SiO ₂ -15.9P ₂ O ₅ -2.9MgO (wt.%)	Sol-gel	1200	Ak, HA	[36]

EXPERIMENTAL PART

1. Synthesis of the glass-ceramics

The two investigated sol-gel glass-ceramics were synthesized by the sol-gel technique as reported in [35].

Glass ceramics were prepared by the sol-gel method using tetraethyl orthosilicate ((C₂H₅O)₄Si, TEOS), magnesium nitrate hexahydrate (Mg(NO₃)₂·6H₂O) and calcium nitrate tetrahydrate (Ca(NO₃)₂·4H₂O) as raw materials. Nitric acid (HNO₃, 2N) was used to catalyze the hydrolysis of TEOS. The TEOS was mixed with absolute ethanol, water and 2N HNO₃ (molar ratio: TEOS/H₂O/HNO₃=1:8:0.16) and hydrolyzed for one hour under stirring. Then, the solutions of Ca(NO₃)₂·4H₂O and Mg(NO₃)₂·6H₂O were added into the mixture (molar ratio: TEOS/Mg(NO₃)₂·6H₂O/Ca(NO₃)₂·4H₂O = 2:1:3), and the reactants were stirred for 6 hours at room temperature. After mixing, the solution was dried at 100°C for 2 days to obtain the dry gel. The dried gel was calcined at 600°C for 2 hours. Finally, the powders were thermally treated. The sample obtained after thermal treatment at 1250°C for 2 hours was denoted as 738. The other sample, obtained after thermal treatment at 1350°C for 2 hours, was denoted as 709.

2. Structural characterization

The crystal structure of the synthesized glass-ceramic materials after heat treatment was evaluated by Fourier Transform Infrared Spectroscopy (FTIR) and X-Ray Diffraction (XRD). FTIR transmittance spectra were obtained using an FTIR spectrometer (Nicolet, USA) in the region 4000-400 cm⁻¹ with a resolution of 4 cm⁻¹ by the KBr pellet technique. The XRD measurements were carried out using a D8 Brucker ADVANCE X-Ray diffractometer, equipped with a VANTEC-1 detector. The XRD spectra were recorded in the 2 Theta (2 θ) range using CuKα radiation in the range 0-100°.

3. In vitro apatite forming ability

The apatite forming ability of the synthesized glass-ceramics was assessed by immersion of the pellets for 3, 9 and 15 days in Simulated Body Fluid (SBF), prepared as described by Kokubo et al. [37]. When the samples were removed from the SBF solution they were rinsed with ethanol and distilled water, dried and stored in containers. After immersion in SBF, all specimens were characterized by FTIR and XRD. The ionic concentrations of Ca, P, Si, and Mg of

these solutions were determined by Inductively Coupled Plasma Atomic Emission Spectroscopy (ICP-AES), Iris 1000, Thermo Elemental, USA.

RESULTS AND DISCUSSION

X-ray diffraction analysis of the synthesized samples is given in Fig. 1

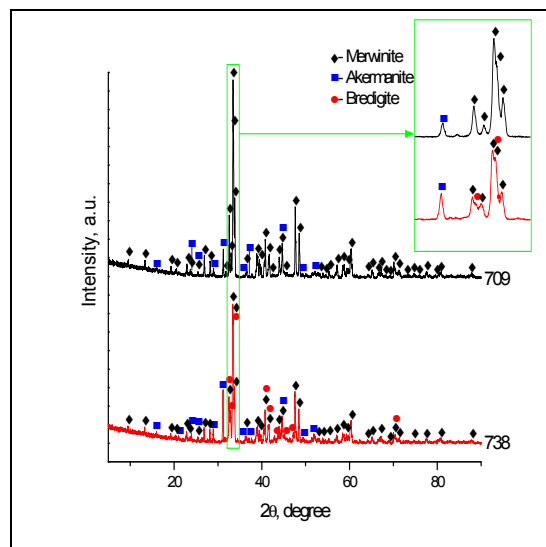


Figure 1. XRD patterns of the 709 and 738 samples, after thermal treatment at 1350°C and 1250°C for 2 hours

The XRD diffractograms of prepared and thermally treated samples are different. In sample 709, XRD detects the presence of merwinite (PDF card 35-0591) as the main crystalline phase and akermanite (PDF card 35-0592). In the case of sample 738, XRD proved the presence of merwinite (PDF card 35-0591), akermanite (PDF card 35-0592) and bredigite (PDF card 36-0399). Similar results were published by R. Choudhary et al. [25], who prepared akermanite by the sol-gel combustion method using eggshell waste as a calcium source.

The FTIR spectra of the prepared glass-ceramics after annealing at 1350°C and 1250°C for 2 hours are shown in Fig. 2.

The peaks posited at 1023, 997, 970, 940, 903, 884, 863 (867), 587 (589), 535, 515 (513), 435 (437) and 407 (408) cm⁻¹ confirmed the presence of merwinite [35, 38, 39].

The absorption bands centered at 970, 903, 847, 701, 684 (682), 638, 631, 587 (589), and 407 (408) cm⁻¹ could be related to akermanite [25, 38, 40, 41]. The bands at 610, 470, 460, 428, and 417 cm⁻¹ could be related to bredigite [23, 25, 40, 42]. The presented FTIR results are in good agreement with the XRD results.

Fig. 3 shows the XRD patterns of the two glass-ceramics after soaking in SBF solution for 15 days in static conditions.

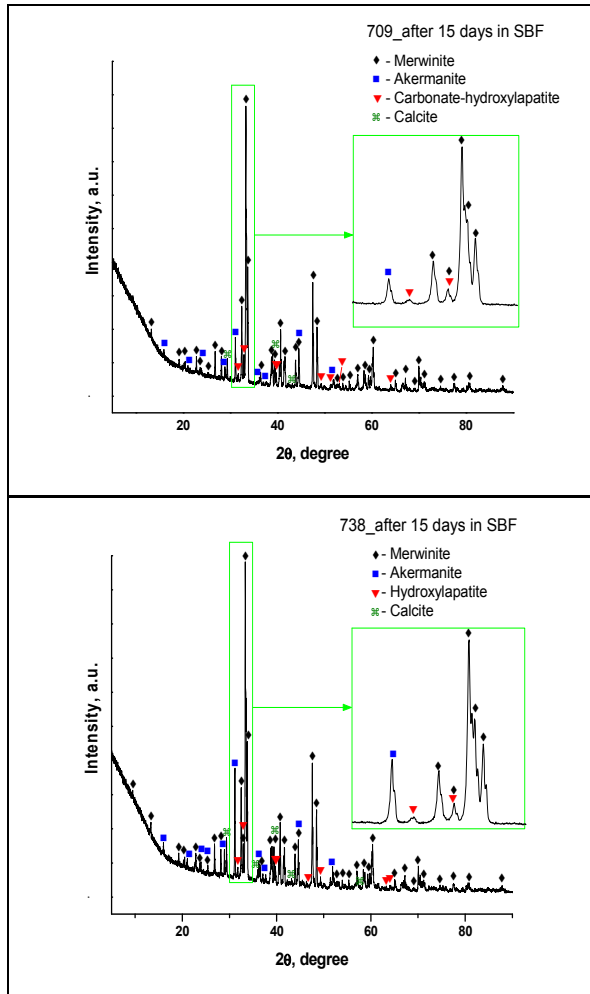


Figure 3. XRD patterns of the prepared and thermally treated at different temperatures 709 and 738 glass-ceramics, after soaking in SBF solution for 15 days in static conditions

From the data in Fig. 3 it is obvious that the peaks of bredigite completely disappeared [15, 21, 22] and the characteristic peaks of CO_3HA (PDF card 96-900-3553) appeared after soaking for 15 days. On the other hand, the peak of calcite (PDF card 5-0586) was also detected.

FTIR spectra of the synthesized Mg-containing glass-ceramics after soaking in SBF solution for 3, 9, and 15 days are presented in Fig. 4.

Theoretically, four vibrational modes are visible for the PO_4^{3-} ions in HA structure: $\nu_3 \text{PO}_4^3$ at $1190\text{-}980 \text{ cm}^{-1}$, $\nu_1 \text{PO}_4^3$ at $960\text{-}965 \text{ cm}^{-1}$, $\nu_4 \text{PO}_4^3$ at $660\text{-}520 \text{ cm}^{-1}$, and $\nu_2 \text{PO}_4^3$ at 460 cm^{-1} [43]. Furthermore, from the presented in Fig. 6 it is visible that in the FTIR spectra $\nu_3 \text{CO}_3^{2-}$ and ν_2

CO_3^{2-} are also detectable [44, 45]. It is well known that carbonate containing HA structure (CO_3HA) depends on its chemical composition. There are two types of substitution in HA lattice: CO_3^{2-} can replace PO_4^{3-} ions (B-type) and CO_3^{2-} can replace OH^- ions (A-type) [46-48].

IR frequencies for the synthesized glass-ceramics, after soaking in SBF solution for 3, 9 and 15 days are given in Table 2.

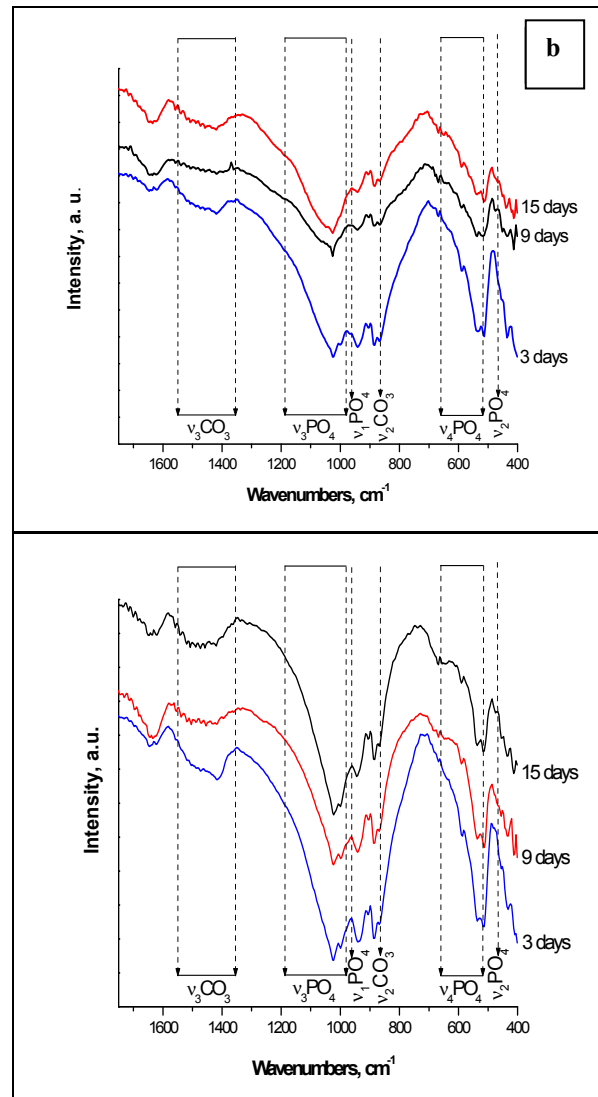


Figure 4. FTIR of the prepared glass-ceramics (sample 709, a, and sample 738, b), after immersion in SBF solution in static conditions

On the basis of the results obtained, we can conclude that:

- $\nu_1 \text{PO}_4^3$ at 960 cm^{-1} shifts to lower wave numbers ($963\text{-}967 \text{ cm}^{-1}$) due to the CO_3^{2-} substitution [49];
- B-type CO_3HA is preferentially observed on the surface of the soaking glass-ceramics [4, 45, 51, 55-61];

- A-type CO₃HA was also detected [46, 51, 55].

Table 2. Vibration modes for the samples after soaking in SBF solution for 3, 9 and 15 days and corresponding frequencies (cm⁻¹), where A and B are A-type CO₃HA or B-type CO₃HA, respectively

Vibrational mode	Sample 709			Sample 738			Assigned according to
	3 days	9 days	15 days	3 days	9 days	15 days	
v ₃ PO ₄ stretching	1022 1044	1024 1045	1026 1040	1023 1052	1024 1044	1022 1050	[44] [44]
v ₁ PO ₄ stretching	963, B	965, B	967, B	960, B	964, B	963, B	[49]
v ₄ PO ₄ stretching	538 567 575 609 638 722	540 567 570 618 640 720 765	538 565 575 611 635 720 765	540 565 574 610 641 719	530 563 575 614 649 720 763	525 565 581 613 642 720 763	[20, 50] [31, 38, 43] [25] [34] [51] [51] [52]
v ₂ PO ₄ stretching	456	451	441 454	456	448 458	458	[20, 49] [53, 54]
v ₃ CO ₃ stretching	1543, A 1521, A 1508 1489, A 1489, B 1473, B 1458, B 1434, B 1416, B 1396, B	1540, A 1521, A 1504, A 1489, B 1473, B 1457, B 1436, B 1418, B 1397, B	1540, A 1521, A 1509, A 1489, B 1473, B 1457, B 1440, B 1418, B 1397, B	1538, A 1517, A 1503, A 1487, B 1473, B 1457, B 1440, B 1415, B 1400, B	1539, A 1518, A 1504, A 1488, B 1470, B 1453, B 1433, B 1415, B 1394, B	1542, A 1522, A 1505, A 1490, B 1474, B 1458, B 1436, B 1419, B 1397, B	[55] [46] [51] [51, 56] [55, 57] [45, 58, 59] [59, 60] [61] [5]
v ₂ CO ₃ bending	867	866	864	865	867	867	[44]
Ca-CO ₃ calcite	710	710	712	710	712	714	[62]

Briefly, we can summarize that the prepared glass-ceramics are *in vitro* bioactive.

From the data presented in Fig. 5, it can be seen that the Ca²⁺ concentration slightly increased for all soaked samples, compared with the Ca²⁺ concentration (64 mg/l) in the initial SBF solution. On the other hand, the concentration of Si⁴⁺ slightly decreased with increasing the soaking times from 80 mg/l (for 709-3) to 26 mg/l (for 709-15), and for 63 mg/l (for 738-3) to

20 mg/l (for 738-15). From the data obtained, it can be concluded that the silicon containing CO₃HA may be formed on the soaked surface of the thermally treated samples. The concentration of Mg²⁺ in SBF solutions shows the same trends. For all studied samples, the concentration of Mg²⁺ in SBF solution (31 mg/l) increased to 99 mg/l (for 703-9) and to 83 mg/l (for 738-3 and then slightly decreased to 26 mg/l (for 709-15) and to 20 mg/l (for 738-15). It is very likely that Mg²⁺ is also included in CO₃HA, which is formed on the soaked surface. Finally, the P⁵⁺ concentration slightly decreased from 29 mg/l (for the initial SBF solution) to 0 mg/l (for all samples) regardless of the soaking time

Si⁴⁺ slightly decreased with increasing the soaking times from 80 mg/l (for 709-3) to 26 mg/l (for 709-15), and for 63 mg/l (for 738-3) to 20 mg/l (for 738-15). From the data obtained, it can be concluded that the silicon containing CO₃HA may be formed on the soaked surface of the thermally treated samples. The concentration of Mg²⁺ in SBF solutions shows the same trends. For all studied samples, the concentration of Mg²⁺ in SBF solution (31 mg/l) increased to 99 mg/l (for 703-9) and to 83 mg/l (for 738-3 and then slightly decreased to 26 mg/l (for 709-15) and to 20 mg/l (for 738-15). It is very likely that Mg²⁺ is also included in CO₃HA, which is formed on the soaked surface. Finally, the P⁵⁺ concentration slightly decreased from 29 mg/l (for the initial SBF solution) to 0 mg/l (for all samples) regardless of the soaking time.

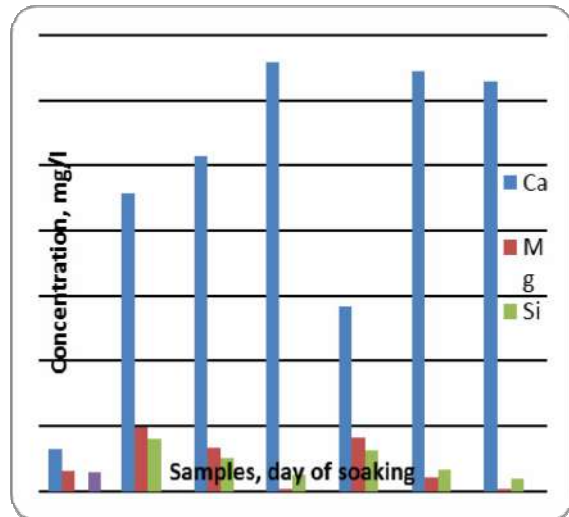


Fig. 5. Changes in Ca, Si, Mg and P concentrations for the SBF solutions (sample SBF) and for samples 709 and 738, after *in vitro* test in SBF solutions for 3, 9 and 15 days in static conditions

The obtained ICP-AES data indicate that the Si^{4+} and Mg^{2+} containing CO_3HA may be formed on the soaked surface. Furthermore, the presences of the bands of PO_4^{3-} in FTIR spectra in the *in vitro* test suggest that the prepared samples are *in vitro* bioactive. The presented ICP-AES data are in agreement with XRD and FTIR data analysis for the soaked samples.

SEM of the samples after soaking in SBF solution for 15 days in static conditions are presented in Fig. 6.

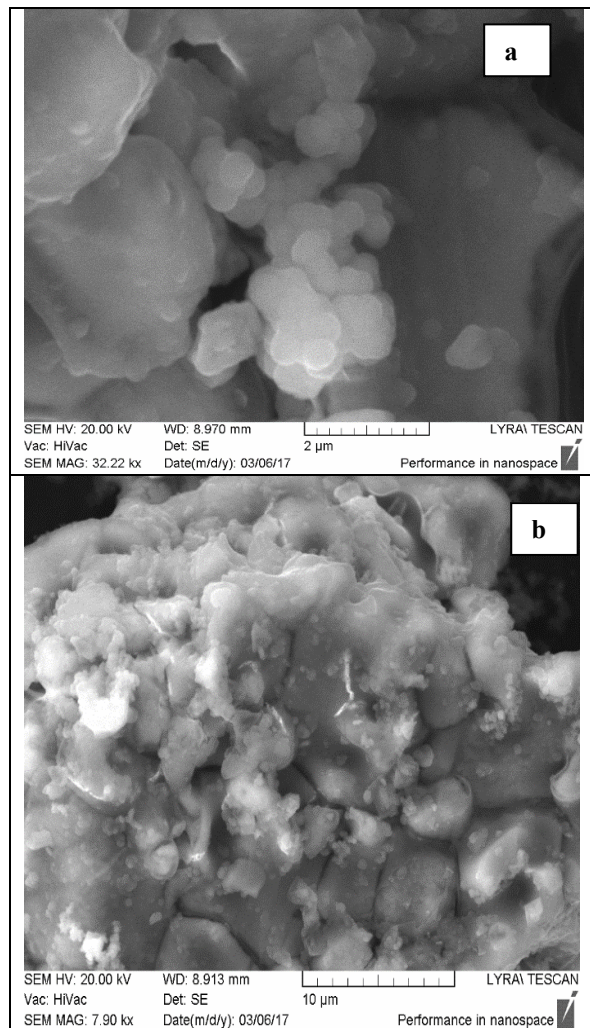


Figure 6. SEM for the soaking in SBF solution 709 (a) and 738 (b) samples for 15 days in static conditions.

The presented SEM results show that on the surface of the soaked samples HA were formed, i. e. the obtained glass-ceramics are *in vitro* bioactive. Spherical aggregates of a diameter of 1.5 μm - 2 μm, consisting of smaller particles (of a typical size of 0.2 μm), are observed (Fig. 6 a, b). This microstructure is typical of apatite. The

obtained results are in full agreement with XRD, FTIR and ICP-AES results.

CONCLUSIONS

Novel Mg-containing glass ceramics were synthesized via sol-gel method. The obtained dried gels were thermally treated at 1350°C and 1250°C. XRD of these samples proved that in the sample annealed at 1350°C merwinite crystallized as a main phase accompanied with akermanite. When the sample was treated at 1250°C merwinite was also present in the main phase, accompanied by the two additional crystalline phases: akermanite and bredigite. FTIR of the samples after *in vitro* tests in SBF solution for different times in static conditions revealed that B-type carbonate apatite (B- CO_3HA) is preferentially observed on the surface of the soaked samples. ICP-AES results showed that Mg^{2+} and Si^{4+} containing CO_3HA may be formed on the surface after immersion in SBF solutions for 3, 9 and 15 days of soaking.

ACKNOWLEDGEMENTS

I would like to thank **Prof. Irena Michailova** from the Department of Silicate Technology in UCTM Sofia for her assistance with XRD data and for comments that greatly improved the manuscript

REFERENCES

- [1] Kannan S., F. Goetz-Neunhoeffler, J. Neubauer, J. M. F. Ferreira, *J Am Ceram Soc.*, **91** [1], (2008), p. 1-12.
- [2] Bianco A., I. Cacciotti, M. Lombardi, L. Montanaro. *Mater Res Bull.*, **44** [2], (2009), p. 345-54.
- [3] Suchanek W. L., K. Byrappa, P. Shuk, R. E. Riman, V. F. Janas, K. S. TenHuisen, *Biomaterials*, **25** [19], (2004) p. 4647-57.
- [4] Cacciotti I., A. Bianco, M. Lombardi, L. Montanaro, *J Eur Ceram Soc.*, **29** [14] (2009), p. 2969-78.
- [5] Dorozhkin S. V., *J Am Ceram Soc.*, **90** [1], (2007), p. 244-9.
- [6] Dorozhkin S. V., *Acta Biomaterialia*, **6** [3] (2010), p. 715-34.
- [7] Anast C. S., T. V. Burns, J. M. Mohs, S. S. Kaplan, *Science*, **177** (1972), p. 606-8.
- [8] Lansdown A. B. G., *Lancet*, **347** (1996), p. 706-7.

- [9] Diba M., O.-M. Goudouri, F. Tapia, A. R. Boccaccini. *Curr Opin Solid State Mater.*, **18** [3] (2014), p. 147-67.
- [10] Hou X., G. Yin, X. Chen, X. Liao, Y. Yao, Zh. Huang, *Appl Surf Sci*, **257** [8], (2011), p. 3417–22.
- [11] Wu Ch., J. Chang., *J Biomater Appl*, **21**, (2006), p. 119-29.
- [12] Huang Y., X. Jin, X. Zhang, H. Sun, J. Tu, T. Tang, et al., *Biomaterials*, **30** [28], (2009), p. 5041–8.
- [13] Chen L., D. Zhai, Ch. Wu, J. Chang. *Ceram Int. part B*, **40** [8], (2014), p. 12765–75.
- [14] Wu Ch., J. Chang, S. Ni, J. Wang, *J Biomed Mater Res*, **78A** [1], (2006), p. 73–80.
- [15] Wu Ch., J. Chang. *J Biomed Mater Res*, **83B** [1], (2007), p. 153–60.
- [16] Wu Ch., Y. Ramaswamy, H. Zreiqat, *Acta Biomaterialia* **6** [6] (2010), p. 2237–45.
- [17] Luo T., Ch. Wu, Y. Zhang, *J Biomed Mater Res*. **100A** [9], (2012), p. 2269–77.
- [18] Lu J., J. Wei, Q. Gan, X. Lu, J. Hou, W. Song, et al., *Microporous and Mesoporous Mater.*, **163**, (2012), p. 221–8.
- [19] Zhang Y., Sh. Li, Ch. Wu, *J Biomed Mater Res.*, **102A**, (2014), p. 105-16.
- [20] Hafezi-Ardakani M., F. Moztafzadeh, M. Rabiee, *Ceram Int.*, **37** [1], (2011), p. 175-80.
- [21] Wu Ch., J. Chang, J. Wang, S. Ni, W. Zhai, *Biomaterials*, **26** [16], (2005), p. 2925–31.
- [22] Huang X.-H., J. Chang, *Mater Res Bull.*, **43** [6], (2008), p. 1615–20.
- [23] Mirhadi S. M., F. Tavangarian, R. Emadi. *Mater Sci Eng*, **32C** [2], (2012), p. 133–9.
- [24] Liu D.-M., *Mater Chem Phys.*, **36**, (1994), p. 294-303.
- [25] Choudhary R., S. Koppala, S. Swamiappan. *J Asian Ceram Soc.*, **3** [2], (2015), p. 173-7.
- [26] Ma J., C.Z. Chen, D.G. Wang, J.H. Hu, *Mater Lett*. **65**, (2011), p. 130-3.
- [27] Ma J., C. Z. Chen, D. G. Wang, X. Shao, C.Z. Wang, H. M. Zhang, *Ceram Int.*, **38** [8], (2012), p. 6677–84.
- [28] Ma J., C. Z. Chen, D. G. Wang, J. H. Hu. , *Ceram Int.*, **37**, (2011), p. 1637–44.
- [29] Bernardo E., J.-F. Carlotti, P. M Dias, L. Fiocco, P. Colombo, L. Treccani, et al. *Ceram Int.*, **40**, (2014), p. 1029–35.
- [30] Chen X., M. Zgang, X. Pu, G. Yin, X. Liao, Zh. Huang, et al., *Surf Coat Technol.*, **249**, (2014), p. 97-203.
- [31]. Chen X, X. Liao, Zh. Huang, P. You, Ch. Chen, Y. Kang, et al., *J Biomater Res Part B: Appl Biomater*, **93B**, (2010), p. 194–202.
- [32] Zhang M., X. Chen, X. Pu, X. Liao, Zh. Huang, G. Yin, *Colloids and Surfaces B: Bio-interfaces*, **116**, (2014), p. 1–8.
- [33] Goudouri O.-M., E. Kontonasaki, K. Chrissafis, K. Zinn, A. Hoppe, R. Detsch, et al., *Ceram Int.*, **40**, (2014), p. 16287–98.
- [34] Mihailova I., L. Radev, V. Aleksandrova, I. Colova, I. M. M. Salvado, Fernandes MHV., *J Chem Techn Metall.*, **50** [4], (2015), p. 502-11.
- [35] Michailova I., L. Radev, V. Aleksandrova, I. Colova, I. M. M. Salvado, M. H. V. Fernandes. *Bull Chem Soc Commun*, **47** [1], (2015), p. 253-60.
- [36] Radev L., V. Hristov, I. Michailova, B. Samuneva, *Cent Eur J Chem*, **7** [3], (2009), p. 322-7.
- [37] Kokubo T., H. Kushitani, S. Sakka, T. Kitsugi, T. Yamamuro, *J Biomed Mater Res.*, **24** [8], (1990), p. 721-34.
- [38] Goudouri O. M., E. Theodosoglou, E. Kontonasaki, J. Will, K. Chrissafis, P. Koidis, et al. *Mater Res Bull.*, **49**, (2014), p. 399–404.
- [39] Piriou B., P. McMillan, *Amer Mineral*, **68**, (1983), p. 426-43
- [40] Chukanov N. V.. *Enstended library*. **1**, (2014), p. 751.
- [41] Li H. C., D. G. Wang, C. Z. Chen, H. Shi. *Mater Lett*, **159**, (2015), p. 459-62.
- [42] Kouhi M., M. P. Prabhakaran, M. Shamanian, M. Fathi, M. Morshed, S. Ramakrishna. *Composite Sci Technol*, **121**, (2015), p. 115-22.
- [43] Rehman I., W. Bonfield, *J Mater Sci: Mater Med.*, **8** [1], (1997), p. 1-4.
- [44] Rey C., V. Renugopalakrishnan, B. Collins, M. J. Glimcher, *Calcif Tissue Int.*, **49** [4], (1991), p. 251-8.
- [45] Vignoles M., G. Bonel, D. W. Holcomb, R. A. Young, *Calcif Tissue Int*, **43** [1], (1988),
- [46] Fleet M., X. Liu, King P., *Am Mineral*, **89**, (2004), p. 1422-32.
- [47] Fleet M., X. Liu, *J Solid State Chem.*, **177**, (2004), p. 3174-82.
- [48] Fleet M., X. Liu, *Biomaterials*, **28**, (2007), p. 916-26.
- [49] Penel G., Leroy G, I. Rey, E. Bres, *Calcif Tissue Int.*, **63** [6], (1998), p. 475-81.
- [50] Agathopoulos S., D. U. Tulyaganov, J. M. G. Ventura, S. Kannan, M. A. Karakassides, J. M. F. Ferreira, *Biomaterials*, **27** [9], (2006), p. 1832-40.
- [51] el Feki H., I. Rey, M. Vignoles, *Calcif Tissue Int.*, **49** [4], (1991), p. 269-74.
- [52] Awonusi A., M. D. Morris, M. M. Tecklenburg, *Calcif Tissue Int.*, **81** [1], (2007), p. 46-52.

- [53] Lafon J. P., E. Champion, D. Bernache-Assollant, R. Gibert, A. M. Danna. *J Thermal Anal Calorimetry*, **72** [3], (2003), p. 1127-34.
- [54] Singh R. K., A. Srinivasan, *Ceram Int.*, **36** [1], (2010), p. 283-90.
- [55] Barralet J. E., G. J. P. Fleming, C. Campion, J. J. Harris, Wright A. J., *J Mater Sci.*, **38** [19], (2003), p. 3979-93.
- [56] Radev L., T. Gerganov, H. Georgiev, A. Kolev, V. Vassileva, R. Iankova, et al. *Int J Mater Chem.*, **3A**, (2013), p. 8-15.
- [57] Pappas G. S., P. Liatsi, I. A. Kartsonakis, I. Danilidis, G. Kordas. *J Non-Cryst Solids*, **354** [2-9], (2008), p. 755-60
- [58] Yusufoglu Y., M. Akinc. *J Am Ceram Soc.*, **91** [1], (2008), p. 77-82.
- [59] Cerruti M., C. Morterra, *Langmuir*, **20** [15], (2004), p. 6382-8.
- [60] Hong Zh., A. Liu, L. Chen, X. Chen, X. Jing, *J Non-Cryst Solids*, **355** [6], (2009), p. 368-72.
- [61] He Q., Zh. Huang, Y. Liu, W. Chen, T. Xu. *Mater Lett*, **61** [1], (2007), p. 141-3.
- [62] Liu J., Y. Kong, J. Yao, Y. Cai, *Mater Lett*, **110**, (2013), p. 221-4.

Assen Zlatarov University
ANNUAL, VOL. XLVIII, BOOK 1, 2019
TECHNICAL AND NATURAL SCIENCES

Editor-in-Chief
Prof. Margarita Terzieva, DSc

Co-editors
Assoc. Prof. Penka Peeva, PhD
Assoc. Prof. Liliya Staneva, PhD
Asst. Prof. Ivan Sokolov

Technical Assistant
Iliana Ishmerieva

Design and layout
Libra Scorp Publisher
www.meridian27.com

Edition of
Assen Zlatarov University
www.btu.bg

ISSN 2603-3968

BURGAS, 2019

ISSN 2603-3968



9 772603 396002